

# UC San Diego

## UC San Diego Electronic Theses and Dissertations

### Title

Short-Range Wireless Communication: from Bio-Implants to Body-Area Networks

### Permalink

<https://escholarship.org/uc/item/0gs6w9sn>

### Author

Park, Jiwoong

### Publication Date

2019

Peer reviewed|Thesis/dissertation

UNIVERSITY OF CALIFORNIA SAN DIEGO

**Short-Range Wireless Communication:  
from Bio-Implants to Body-Area Networks**

A dissertation submitted in partial satisfaction of the requirements for the degree  
Doctor of Philosophy

in

Electrical Engineering (Electronic Circuits and Systems)

by

Jiwoong Park

Committee in charge:

Professor Patrick Mercier, Chair  
Professor Peter Asbeck  
Professor Gert Cauwenberghs  
Professor Todd Coleman  
Professor Daniel Sievenpiper

2019

Copyright  
Jiwoong Park, 2019  
All rights reserved.

The dissertation of Jiwoong Park is approved, and it is acceptable in quality and form for publication on microfilm and electronically:

---

---

---

---

---

---

Chair

University of California San Diego

2019

## DEDICATION

*To the wisdom of my parents  
who raise me up to more than I can be.*

## EPIGRAPH

*Learn from yesterday, live for today, hope for tomorrow.*

*The important thing is not to stop questioning.*

- Albert Einstein

## TABLE OF CONTENTS

Signature Page . . . . .	iii
Dedication . . . . .	iv
Epigraph . . . . .	v
Table of Contents . . . . .	vi
List of Figures . . . . .	viii
List of Tables . . . . .	xiv
Acknowledgements . . . . .	xv
Vita . . . . .	xviii
Abstract of the Dissertation . . . . .	xx
Chapter 1. Introduction . . . . .	1
Chapter 2. Channel Modeling of Capacitive-Coupled Electric Human Body Communication Link for Wearable Applications . . . . .	5
2.1. Previous Measurement Configurations . . . . .	8
2.1.1. Measurements with a Vector Network Analyzer . . . . .	9
2.1.2. Measurements with Signal Generators and Spectrum Analyzers . . . . .	11
2.2. Proposed Measurement Configuration . . . . .	12
2.2.1. Gain Definition: Power Gain vs. Voltage Gain . . . . .	14
2.2.2. Electrode Impedance Measurements . . . . .	16
2.2.3. Transmitter Circuitry Configuration . . . . .	17
2.2.4. Receiver Circuitry Configuration . . . . .	18
2.3. Proposed Simulation Model using Circuit & FEM Analysis . . . . .	20
2.3.1. Hybrid Approach . . . . .	20
2.3.2. Electromagnetic Simulation Model . . . . .	23
2.3.3. Electrostatic Circuit Simulation Model . . . . .	25
2.4. Results . . . . .	26
2.5. Conclusion . . . . .	29
Chapter 3. Energy-Efficient Intra-Body Wireless Data Transfer via Magnetic Human Body Communication . . . . .	31
3.1. Theoretical Background . . . . .	34
3.1.1. Characterization of Magnetic Fields in the Human Body . . . . .	34
3.1.2. Human Body as a Leaky Dielectric Waveguide . . . . .	37

3.1.3. mHBC Wireless Channel Link . . . . .	43
3.1.4. Health Safety of mHBC . . . . .	44
3.2. Results . . . . .	45
3.2.1. Validation of Analysis with FEM simulations . . . . .	45
3.2.2. Measurement Results . . . . .	46
3.2.3. System Demonstration . . . . .	49
3.3. Methods and Material . . . . .	50
3.3.1. Simulation Methods . . . . .	50
3.3.2. Measurement Materials and Methods . . . . .	52
3.4. Conclusion . . . . .	54
Chapter 4. A Sub-10 pJ/bit 5 Mbps Magnetic Human Body Communication Transceiver Demonstrating High-Fidelity Audio Trans-Body Delivery . . . . .	56
4.1. Wireless Body Area Network Approaches . . . . .	58
4.1.1. Sub-6 GHz Radio Frequency . . . . .	58
4.1.2. Electric Human Body Communication . . . . .	60
4.1.3. Magnetic Human Body Communication . . . . .	61
4.2. mHBC Transmitter Implementation . . . . .	65
4.2.1. Challenges of PO-based Direct-Modulation Transmitters . . . . .	66
4.2.2. TX Circuit Design . . . . .	68
4.3. mHBC Receiver Implementation . . . . .	70
4.3.1. Design Challenges of Direct-ED Receivers . . . . .	71
4.3.2. RX Circuit Design . . . . .	73
4.4. Measurement Results . . . . .	75
4.5. Demonstration . . . . .	82
4.6. Conclusion . . . . .	85
Chapter 5. Wireless Powering of Millimeter-Scale Fully-on-Chip Neural Interfaces	87
5.1. On-chip Coil Optimization . . . . .	89
5.1.1. Model parameters . . . . .	89
5.1.2. Optimizing the number of turns . . . . .	91
5.1.3. Optimizing trace width/spacing . . . . .	93
5.1.4. Internal Circuit Routing Considerations . . . . .	94
5.2. Transmit Coil Optimization . . . . .	96
5.3. Measurement Results . . . . .	99
5.4. Conclusion . . . . .	102
Appendix A. Derivation of Field Pattern and Complex Power Density . . . . .	103
Appendix B. Derivation of the Magnetic Flux Density inside the Human Body . . . . .	106
References . . . . .	110

## LIST OF FIGURES

Figure 1.1. An example of short-range wireless communication for wearable devices: wireless body area network for a personal tele-healthcare system . . . . .	1
Figure 1.2. Path gain degradation of 1.5-m 2.4-GHz BLE channel by body shadow effect [1] . . . . .	2
Figure 1.3. Another example of short-range wireless communication: mm-scale fully-integrated implantable neural interface . . . . .	3
Figure 2.1. Conventional HBC path loss measurement configuration using the battery-operated instruments . . . . .	6
Figure 2.2. Proposed measurement setup using the battery-operated wearable prototypes for the accurate HBC path loss estimation. . . . .	7
Figure 2.3. Conventional setups used to measure capacitive HBC links with a vector network analyzer, and their equivalent circuit models . . . . .	10
Figure 2.4. Conventional setups used to measure capacitive HBC links with a signal generator and a spectrum analyzer, and their equivalent circuit models . . .	11
Figure 2.5. Proposed measurement setup and its equivalent circuit model . . . . .	13
Figure 2.6. Photographs of the developed battery-operated HBC wearable prototype of (a) the transmitter unit and (b) the receiver unit . . . . .	14
Figure 2.7. Simplified RX front-end model and its noise figure analysis result of output signal to noise ratio. . . . .	15
Figure 2.8. Multiple measurements of the impedance of HBC electrode pairs. . .	16
Figure 2.9. Vector fitting the averaged measured impedance . . . . .	17
Figure 2.10. Prototype TX circuit configuration for operation at multiple frequencies and its transmitting power definition. . . . .	18
Figure 2.11. Prototype RX circuitry configuration with the replaceable matching network for supporting multi-frequency measurements. . . . .	19
Figure 2.12. An example of power measurements using data received from the RX prototype operating at different frequencies. . . . .	20

Figure 2.13. A hybrid simulation model incorporating electrostatic circuit analysis with FEM EM analysis . . . . .	22
Figure 2.14. HFSS simulation model: (a) the realistic human body surface mesh and (b) the external ground model. . . . .	23
Figure 2.15. HFSS simulation electrode model: (a) the HBC electrode pair and (b) the internal ground plate of a spectrum analyzer . . . . .	24
Figure 2.16. Measured input impedance of electrode pairs placed on the skin, and the corresponding $S$ -parameter simulation models. . . . .	25
Figure 2.17. Measured (solid) and simulated (dashed) path loss results of miniaturized wearable capacitive HBC devices compared to conventional measurement setups using a VNA or a SA. . . . .	26
Figure 2.18. Measurement configurations for the validation of the effect caused by the internal ground plates of large battery-powered spectrum analyzers. . . . .	27
Figure 3.1. (a) RF broadcasting communication techniques (e.g. Bluetooth and UWB) and (b) the power consumption breakdown of a wireless EEG monitor system employing a conventional RF (Bluetooth LE v5.0) technique. . . . .	32
Figure 3.2. Human Body Communication: (a) Capacitive-coupled electric HBC (eHBC) and (b) the proposed magnetic HBC (mHBC). . . . .	33
Figure 3.3. Classified power density generated by: (a) a magnetic dipole antenna, and (b) a electric dipole antenna placed in biological tissue or in air. (c) 3D FEM simulation results of a magnetic dipole antenna in biological tissue or in air. . . . .	36
Figure 3.4. (a) Analytical model for cylindrical dielectric waveguide of a human limb, (b) incidence, reflection, and transmission of perpendicularly polarized EM wave at the tissue-air boundary, and (c) total reflection condition. . . . .	38
Figure 3.5. Analysis of leaky dielectric waveguide excited by an ideal magnetic dipole. . . . .	40
Figure 3.6. The simplified circuit model of magnetic resonance coupling for maximum power gain estimation . . . . .	43
Figure 3.7. (a) the power absorption estimating model by a coil of the conductive tissue and (b) its result. . . . .	44

Figure 3.8. The 3D FEM simulated B-field pattern of far-field, near-field, and total field with the cylindrical human limb model and in air . . . . .	46
Figure 3.9. (a) the analysis and simulation results of B-field magnitude averaged within the cross section of the limb model and (b) within the same dimension in air, . . . . .	47
Figure 3.10. (a) the total averaged B-field magnitude comparison between with body and in air and (b) the estimated path gain from analysis and simulation and its comparison to the measured path gain. . . . .	47
Figure 3.11. Experiment results: (a) path loss vs. distance (wrist to wrist) compared to conventional techniques and (b) Path loss of three coherent coils in a single mHBC system compared to a two-coil system . . . . .	48
Figure 3.12. Additional results: (a) path loss across 40 cm between two wrap-around coils (wrist-to-arm) or between a planar chest-worn patch and a wrap-around coil on an arm and (b) Path loss fluctuation during motion (wrist-to-head) . . . . .	48
Figure 3.13. Demonstration results: (a) symbol-error rate curves at various data rates and (b) Comparison between the acquired EEG data in the TX unit and the demodulation result of received data on the RX side with -35 dBm transmit power. . . . .	49
Figure 3.14. Practical human body model and its simulation results: (a) body surface meshes for HFSS, dielectric properties of human tissues: (b) relative permittivity and (c) conductivity, and (d) path loss simulation results. . . . .	51
Figure 3.15. EEG demonstration: (a) the EEG data transfer prototype, (b) the block diagram of frequency selective digital transmission (FSDT) modulation, and (c) a hardware configuration for the EEG data transfer system. . . . .	53
Figure 4.1. (a) Conventional RF broadcasting (e.g. Bluetooth). (b) Capacitively-coupled eHBC. (c) mHBC. . . . .	57
Figure 4.2. System block diagram of the proposed mHBC transceiver. . . . .	58
Figure 4.3. Channel gain comparison of mHBC to previous wireless BAN approaches. . . . .	59
Figure 4.4. Measured results of maximum available gain and phase shift of the mHBC channel with various body postures. . . . .	63
Figure 4.5. Comparison of required receiver sensitivity between 2.4 GHz RF Bluetooth Low Energy and mHBC. . . . .	64

Figure 4.6. (a) A generic low-complexity TX architecture used in low-power wireless BANs. (b) An energy-efficient TX architecture for relatively-low TX output power. (c) A cross-coupled LC oscillator employed for the mHBC TX PO. . . . .	65
Figure 4.7. Bandwidth limitation caused by high $Q$ coils: (a) Shut-down and start-up time of the PO that needs for $Q$ cycles; (b) too fast data rate results in a poor modulation index; and (c) the trade-off between bandwidth and the channel gain. . . . .	67
Figure 4.8. The inductance fluctuation of wearable mHBC coils: (a) path gain degradation by resonant frequency mismatch between TX and RX; and (b) an example of circuit malfunction: injection pulling. . . . .	68
Figure 4.9. Proposed TX implementation for fast-data-rate communication and with dynamic resonant frequency calibration. . . . .	69
Figure 4.10. Detailed block diagram of the all-digital-frequency-locked-loop. . . . .	70
Figure 4.11. (a) A CS-amp-based ED with a RC filter and its down-conversion gain by 2nd-order inter-modulation. (b) The interference issue plaguing non-coherent down-conversion receivers without channel selection filters. . . . .	71
Figure 4.12. An additional benefit of mHBC: interference rejection by the RX coil and the human body channel itself. . . . .	72
Figure 4.13. Proposed ultra-lower power and energy-efficient mHBC RX architecture and its circuit-level design. . . . .	73
Figure 4.14. Improvement of (a) first-order transconductance efficiency and (b) second-order transconductance efficiency of an n-type dynamic-threshold MOS-FET in deep sub-threshold operation. . . . .	74
Figure 4.15. A implementation summary table, the die photograph, and the layouts of the proposed mHBC transceiver . . . . .	76
Figure 4.16. Measurement results of the high data rate capability of the proposed mHBC TX: $5.5\times$ improved modulation index by rapid-quenching and kick-start circuits. . . . .	77
Figure 4.17. Measurement results of the high data rate capability of the proposed mHBC TX: measured OOK modulated spectra with various data rates, received by a wire-wound RX coil ( $Q_{RX}=8$ ) with 10-cm distance air (12-dB loss). . . . .	77
Figure 4.18. Measurement results of dynamic resonant frequency calibration for the proposed mHBC TX: measured spectrum and frequency tracking waveform (inset) of ADPLL operation. . . . .	78

Figure 4.19. Measurement results of dynamic resonant frequency calibration for the proposed mHBC TX: measured inductance variation coverage by capacitor-array DAC in ADFLL. . . . .	79
Figure 4.20. RX measurement results: (a) received signal strength variation under inductance fluctuation by user’s moving when the TX output power is -24.8dBm at 40 MHz and (b) RX bit-error-rate results with various data rates. . . . .	80
Figure 4.21. Measured waveform results of 1-m trans-body TX-to-RX data transfer. . . . .	81
Figure 4.22. (a) A summary of the proposed mHBC TRX specification. (b) E/bit comparison to the prior eHBC TRXs. . . . .	83
Figure 4.23. A Hi-Fi audio streaming demonstration: (a) demonstration block diagram; (b) mHBC TX unit prototype fitted in a compact-sized smartphone; (c) mHBC RX headphone unit prototypes. . . . .	84
Figure 4.24. Waveform results of the proposed mHBC Hi-Fi audio streaming system. . . . .	85
Figure 5.1. Overview of fully-on-chip modular neural implants. The inset die photo illustrates the on-chip coil and interior active circuitry. . . . .	87
Figure 5.2. Loss mechanisms in an on-chip coil and its typical quality factor as a function of frequency. . . . .	88
Figure 5.3. Equivalent circuit model of inductive power transfer systems. . . . .	89
Figure 5.4. Cross section of the employed FEM simulation model. . . . .	90
Figure 5.5. Frequency-dependent dielectric properties of tissues for the proposed FEM model. . . . .	90
Figure 5.6. (a) Quality factor ( $Q_{RX}$ ), and (b) effective resistance ( $R_{P,RX}$ ) at resonance for various turn-number configurations. . . . .	91
Figure 5.7. Power transfer efficiency for $k=0.005$ , and $Q_{TX}=250$ for AC loads of (a) 0.16 k $\Omega$ , (b) 1.6 k $\Omega$ , and (c) 16 k $\Omega$ . . . . .	92
Figure 5.8. Optimizing $Q_{RX}$ through trace width/spacing engineering. . . . .	94
Figure 5.9. The loss density on metal surfaces indicating the amount of receiving power from a 1 W transmitting coil and neighboring traces . . . . .	95

Figure 5.10. The $Q$ degradation by inner routing and its measured value of the fabricated IC implementing the H-tree routing scheme . . . . .	95
Figure 5.11. Single-turn TX coil optimization for coupling coefficient ( $k$ ). . . . .	96
Figure 5.12. Single-turn TX coil optimization for quality factor ( $Q_{TX}$ ) at the RX optimal frequency. . . . .	97
Figure 5.13. Transmit coil optimization for 1 oz copper ( $35 \mu\text{m}$ thickness) on a PCB, for 15 mm coupling distance (5 mm of air and 10 mm of tissue). . . . .	97
Figure 5.14. TX shape optimization. . . . .	98
Figure 5.15. (a) Operating frequency selection with 5 mm air gap and (b) optimal air separation from tissue when considering SAR at 144 MHz. . . . .	99
Figure 5.16. (a) Maximum PTE under optimal load conditions, along with estimated $k$ . (b) Measured and simulated PTE with a $1.6 \text{ k}\Omega$ AC load in air and galline tissue. . . . .	100
Figure A.1. (a) An ideal magnetic dipole and its near-field pattern and (b) a Hertzian electric dipole and its near-field pattern . . . . .	104

## LIST OF TABLES

Table 2.1. Impedance Matching Network Configuration . . . . .	19
Table 2.2. Electrostatic Circuit Modeling Component Values . . . . .	25
Table 2.3. Measured and Simulated Path Loss of Capacitive HBC Channel . . . . .	29
Table 4.1. Performance Comparison Table . . . . .	82
Table 5.1. Table of Comparisons to Recent mm-Scale WPT Links for Implants under In-vitro Conditions . . . . .	102

## ACKNOWLEDGEMENTS

I lived my childhood filled with joy and fun, drawing lines in the night sky with my small index finger to find constellations that ignited my imagination with their myths and stories. My journey to pursue the pinnacle of academic achievement (a.k.a Ph.D. degree) began with flying for over 13 hours through the gorgeous night sky over the Pacific Ocean, where the stars were twinkling as I had seen since my childhood. Eventually, this academic adventure culminates in the submission of a doctoral dissertation, providing unforgettable memories, as beautiful as twinkling stars in tonight's sky, with all of those who have shared their lives with me in joy and sorrow.

First of all, I would like to thank my advisor, Professor Patrick Mercier, for providing me with the opportunity to conduct research that pushes the boundaries of the state-of-the-art. I am deeply indebted to you for your advice, not merely related to the technical aspects, but also on how to deliver better presentations, how to elaborate a key idea in research papers, and even how to manage cooperative work with others. I also would like to extend my sincerest gratitude to my dissertation committee members, Professor Peter Asbeck, Professor Gert Cauwenberghs, Professor Todd Coleman, and Professor Daniel Sievenpiper. A special thanks must go to Professor Gert Cauwenberghs, who provided invaluable advice and brilliant insight while working with his group. As well, I also would like to thank Professor Boubacar Kante for his priceless instructions regarding electromagnetic simulation skills.

My research would not have been possible without the timely help and invaluable discussions from my lab colleagues: Dr. Dhongue Lee, Dr. Hui Wang, Dr. Po-han Wang, Dr. Julian Warchall, and Somayeh Imani. Also, I would like to thank all of the other members of Energy-Efficient Microsystems Lab for all the moments we have shared in the joyful and sometimes stressful life of graduate students. I deeply appreciate my collaborators: Dr. Sohmyung Ha, Dr. Chul Kim, and Abraham Akinin, from Integrated Systems Neuroengineering Lab, who all provided insightful advice not only related to integrated circuit design and measuring techniques but also for the work-life

balance. I thank all of my friends, especially those I met at UCSD: Dr. Inho Jeon, Dr. Seunghyun Lee, Dr. Chihyung Ahn, Dr. Kangmoo Lee, Dr. Kimoon Um, Dr. Jayoung Kim, Dr. Dajung Lee, and Dr. Jiyeon Lee, for being wonderful friends who I could share my thoughts and concerns with during this long journey.

Finally, I would like to thank my family. Their love, encouragement, and support have enabled me to turn a frustrating day into a successful one throughout my doctoral study. I sincerely appreciate my parents, Jungshin Baek and Seongho Park, who raised me to believe in myself and reach for the stars. Also, I want to thank my sister, Jiyeon Park, for encouraging me to achieve my best, and my brother, Jihyo Park, for giving me the motivation to choose my career as an electrical engineer and to open my eyes to see beyond the Korean Peninsula. Lastly, to my beautiful better half, Sojeong Noh: Thank you for your unconditional support and unending patience over my academic journey. You are and always will be my first reason for breathing until the end of my life.

Chapter Two is largely a reprint of material as it appears in "Channel Modeling of Miniaturized Battery-Powered Capacitive Human Body Communication Systems" by Jiwoong Park, Harinath Garudadri, and Patrick P. Mercier in *IEEE Transactions on Biomedical Engineering (TBME)*, February, 2017. The dissertation author was the primary investigator and author of this work.

Chapter Three is largely a combination of material as it is submitted to *Proceedings of the National Academy of Sciences of the United States of America (PNAS)*: "Energy-Efficient Intra-Body Wireless Communication via a Human Body Dielectric Waveguide" and as it appears in "Magnetic Human Body Communication," in *Annual International Conference of the IEEE Engineering in Medicine and Biology Society (EMBC)*, August 2015, which both are written by Jiwoong Park and Patrick P. Mercier. The dissertation author is the primary investigator and author of this work.

Chapter Four is largely a combination of material in the following two papers: "A Sub-40 $\mu$ W 5Mb/s Magnetic Human Body Communication Transceiver Demonstrating Trans-Body Delivery of High-Fidelity Audio to a Wearable In-Ear Headphone," in *IEEE International Solid-State Circuits Conference (ISSCC)*, February 2019, and "A

Sub-10-pJ/bit 5-Mb/s Magnetic Human Body Communication Transceiver,” in IEEE Journal of Solid-State Circuits (JSSC), November 2019, which both are written by Jiwoong Park and Patrick P. Mercier. The author is the primary author and investigator of this work.

Chapter Five is largely a reprint of material as it appears to ”Wireless Powering of mm-Scale Fully-on-Chip Neural Interfaces,” by Jiwoong Park, Chul Kim, Abraham Akinin, Sohmyung Ha, Gert Cauwenberghs, and Patrick P. Mercier in IEEE Biomedical Circuits and Systems Conference (BioCAS), October 2017. The dissertation author is the primary investigator and author of this work.

Jiwoong Park  
La Jolla, California, USA  
October, 2019

## VITA

- 2012 Bachelor of Science (*summa cum laude*) in Electronic, Communication, and Computer Engineering, Hanyang University, Seoul, South Korea.
- 2014 Master of Science in Electrical Engineering (Electronic Circuits and Systems), University of California San Diego, La Jolla, California, USA.
- 2019 Doctor of Philosophy in Electrical Engineering (Electronic Circuits and Systems), University of California San Diego, La Jolla, California, USA.

## PUBLICATIONS

- J. Park and P. P. Mercier, "Energy-Efficient Intra-Body Wireless Communication via a Human Body Dielectric Waveguide," in *Proceedings of the National Academy of Sciences of the United States of America (PNAS)*, under review.
- J. Park and P. P. Mercier, "A Sub-10-pJ/bit 5-Mb/s Magnetic Human Body Communication Transceiver," in *IEEE Journal of Solid-State Circuits (JSSC)*, Nov. 2019.
- C. Kim, J. Park, S. Ha, A. Akinin, R. Kubendran, P.P. Mercier, and G. Cauwenberghs, "A 3 mm  $\times$  3 mm Fully Integrated Wireless Power Receiver and Neural Interface System-on-Chip," in *IEEE Transaction on Biomedical Circuits and Systems (TBioCAS)*, Nov. 2019.
- J. Park and P. P. Mercier, "A Sub-40 $\mu$ W 5Mb/s Magnetic Human Body Communication Transceiver Demonstrating Trans-Body Delivery of High-Fidelity Audio to a Wearable In-Ear Headphone," in *2019 IEEE International Solid-State Circuits Conference (ISSCC)*, Feb. 2019.
- S. Ha, C. Kim, J. Park, G. Cauwenberghs, P.P. Mercier, "A Fully Integrated RF-Powered Energy-Replenishing Current-Controlled Stimulator," in *IEEE Transaction on Biomedical Circuits and Systems (TBioCAS)*, Nov. 2018.
- H. Wang, X. Wang, A. Barfidokht, J. Park, J. Wang, and, P.P. Mercier, "A battery-powered wireless ion sensing system consuming 5.5 nW of average power," in *IEEE Journal of Solid-State Circuits (JSSC)*, Apr. 2018.
- J. Park, C. Kim, A. Akinin, S. Ha, G. Cauwenberghs, and, P.P. Mercier, "Wireless Powering of mm-Scale Fully-on-Chip Neural Interfaces," in *2017 IEEE Biomedical Circuits and Systems Conference (BioCAS)*, Oct. 2017.

- H. Wang, X. Wang, J. Park, A. Barfidokht, J. Wang, and, P.P. Mercier, "A 5.5 nW Battery-Powered Wireless Ion Sensing System," in *2017 IEEE European Solid-State Circuits Conference (ESSCIRC)*, Sep. 2017.
- C. Kim, S. Ha, J. Park, A. Akinin, P.P. Mercier, and G. Cauwenberghs, "A 144-MHz Fully Integrated Resonant Regulating Rectifier with Hybrid Pulse Modulation for mm-Sized Implants," in *IEEE Journal of Solid-State Circuits (JSSC)*, Aug. 2017.
- C. Kim, S. Ha, A. Akinin, J. Park, R. Kubendran, H. Wang, P.P. Mercier, and G. Cauwenberghs, "Design of Miniaturized Wireless Power Receivers for mm-Sized Implants," in *2017 IEEE Custom Integrated Circuits Conference (CICC)*, Apr. 2017.
- D. Ahn, J. Park and P. P. Mercier, "A 200-kHz/6.78-MHz Wireless Power Transmitter Featuring Concurrent Dual-Band Operation," in *2016 IEEE International SoC Design Conference (ISOCC)*, Oct. 2016.
- S. Ha, A. Akinin, J. Park, C. Kim, H. Wang, C. Maier, P.P. Mercier, and G. Cauwenberghs, "Silicon-Integrated High-Density Electro cortical Interfaces," in *Proceedings of the IEEE*, Aug. 2016.
- C. Kim, J. Park, S. Ha, A. Akinin, R. Kubendran, P.P. Mercier, and G. Cauwenberghs, "A Fully Integrated 144 MHz Wireless-Power-Receiver-on-Chip with an Adaptive Buck-Boost Regulating Rectifier and Low-Loss H-Tree Signal Distribution," in *2016 IEEE Symposium on VLSI Circuits (VLSI-Circuit)*, Jun. 2016.
- J. Park, H. Garudadri, and P. P. Mercier, "Channel Modeling of Miniaturized Battery-Powered Capacitive Human Body Communication Systems," in *IEEE Transaction on Bio-medical Engineering (TBME)*, Feb. 2016
- J. Park and P. P. Mercier, "Magnetic Human Body Communication," in *2015 Annual International Conference of the IEEE Engineering in Medicine and Biology Society (EMBC)*, Aug. 2015.
- S. Ha, A. Akinin, J. Park, C. Kim, H. Wang, C. Maier, G. Cauwenberghs, and P.P. Mercier, "A 16-Channel Wireless Neural Interfacing SoC with RF-Powered Energy-Replenishing Adiabatic Stimulation," in *2015 IEEE Symposium on VLSI Circuits (VLSI-Circuit)*, Jun. 2015.
- C. Kim, S. Ha, J. Park, A. Akinin, P.P. Mercier, and G. Cauwenberghs, "A 144MHz Integrated Resonant Regulating Rectifier with Hybrid Pulse modulation," in *2015 IEEE Symposium on VLSI Circuits (VLSI-Circuit)*, Jun. 2015.
- T-C. Chou, R. Subramanian, J. Park, and P.P. Mercier, "A Miniaturized Ultrasonic Power Delivery System," in *2014 IEEE Biomedical Circuits and Systems Conference (Bio-CAS)*, Oct. 2014.

ABSTRACT OF THE DISSERTATION

**Short-Range Wireless Communication:  
from Bio-Implants to Body-Area Networks**

by

Jiwoong Park

Doctor of Philosophy in Electrical Engineering (Electronic Circuits and Systems)

University of California San Diego, 2019

Professor Patrick Mercier, Chair

This dissertation presents energy-efficient schemes for short-range wireless communication for wearable devices. Generally, there are two types of wireless scenarios that happen around the human body. The first case is the data transfer between the wearable devices and the local hub devices, e.g., smartphones and smartwatches, allowing to connect to the external network and centrally control multiple wearable devices. Many researchers had proposed various wireless approaches for this scenario; however, there are still limitations in realistic implementations such as restricted form factors and limited energy sources of wearable devices. To address the barriers and challenges of the previously proposed schemes, my doctoral research introduced a new data transmission concept around the human body using magnetic fields, showing the theoretical background and experimental results that validate that the human body acts as a leaky dielectric waveguide. To demonstrate that the proposed concept can be implemented in the practical application, e.g., Hi-Fi audio streaming for portable headphones, this

dissertation describes the design procedure and its measurement results of an energy-efficient ultra-low-power transceiver fabricated with CMOS technology.

The other wireless scenario occurs in a single wearable device, especially a body sensor device. For the practical reasons of accurate health monitoring, the body sensor device needs to be implanted or injected inside the human body, and it should operate in a fully-wireless environment for the portability of the wearable devices. This work presents guidelines for the design and optimization of on-chip coils used for wireless millimeter-scale integrated neural implants as an example of this wireless scenario. Since available real estate of a silicon chip is limited, on-chip coil design involves difficult managing multi-dimension trade-offs amongst the number of turns, trace width and spacing, proximity to other active circuits and metalization, quality factor, matching network performance/size, and load impedance conditions, all towards achieving high data/power transfer efficiency.

# Chapter 1

## Introduction

Wireless communication functionality is one of the necessary features for almost all wearable devices that need to connect continuously to the external networks via a local hub device such as a smartphone and a smartwatch. Figure 1.1 illustrates an example of wireless body area network systems consisting of wearable devices: a personal tele-healthcare system. In this system, wearable medical sensing devices measure a wide variety of health conditions, and a local hub device collects this physiological information via a body area network for the real-time monitoring of the health state of a subject. Here, the short-range wireless communication for this application requires a high-reliable and energy-efficient communication link for long term real-time monitoring.

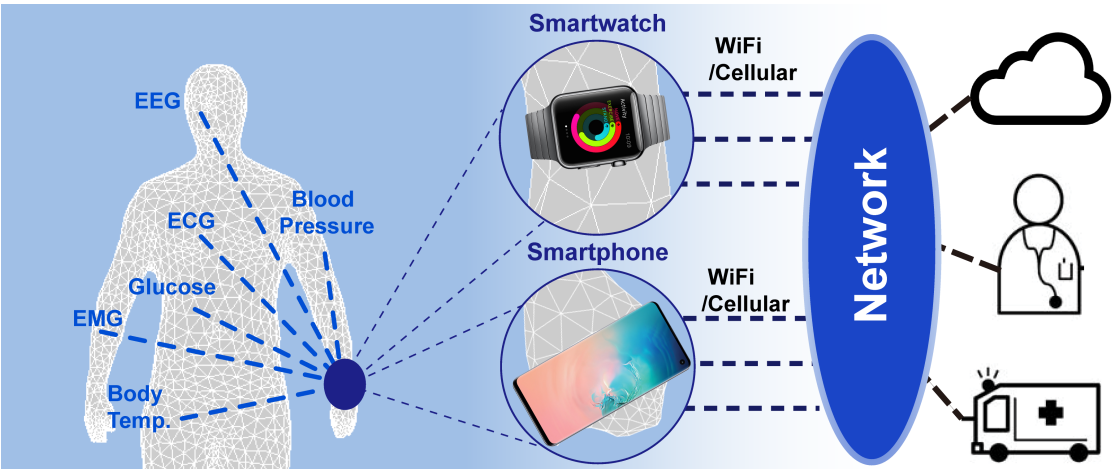


**Figure 1.1:** An example of short-range wireless communication for wearable devices: wireless body area network for a personal tele-healthcare system

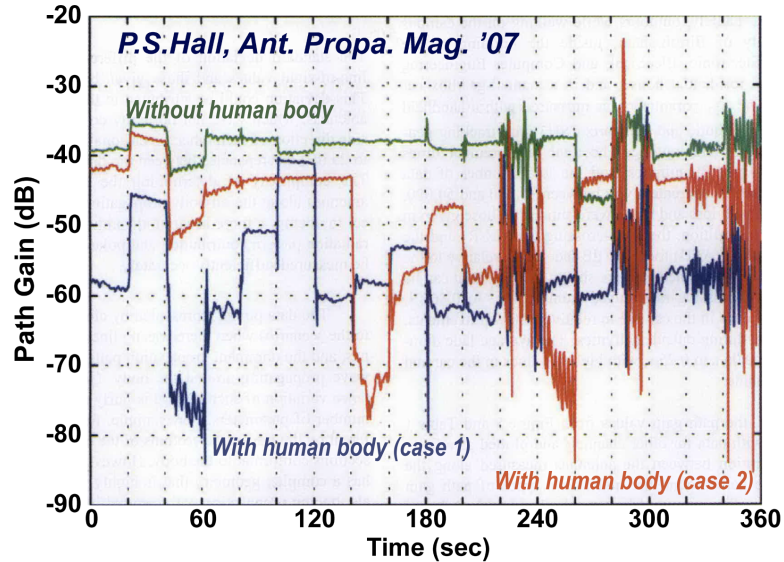


**Figure 1.2:** Path gain degradation of 1.5-m 2.4-GHz BLE channel by body shadow effect [1]

Nowadays, Bluetooth Low Energy (BLE) technology is the standard wireless technique for short-range wireless communication. However, this 2.4 GHz Radio Frequency (RF) wireless is designed originally for over-the-air wireless to cover a 10-m communication range; therefore, it might look sufficient to achieve a reliable and robust wireless connection for 2-m short-range body area network. However, such a wide-range coverage comes with a risk of eavesdropping and wasted power to cover beyond the 2-m body-area range. Furthermore, BLE radio shows a critical disadvantage with the human body presence. Figure 1.2 shows that the path gain decreases up to 50dB due to the body shadow effect caused by the high conductivity of biological tissues at the GHz frequency range [1]. As a result, 2.4 GHz RF BLE requires more transceiver power for higher transmitted power and better receiver sensitivity to compensate for this additional path loss by the human body, which increases the eavesdropping risk too. Since most wearable devices need to be sufficiently small to fit within the human anatomy and their small form factor restricts the capacity of the energy source, an inefficient wireless communication approach involving RF transmission barely allows long-term operating time on a single charge of wearable devices. For this reason, the wearables market is starved for innovations in wireless communication technologies.

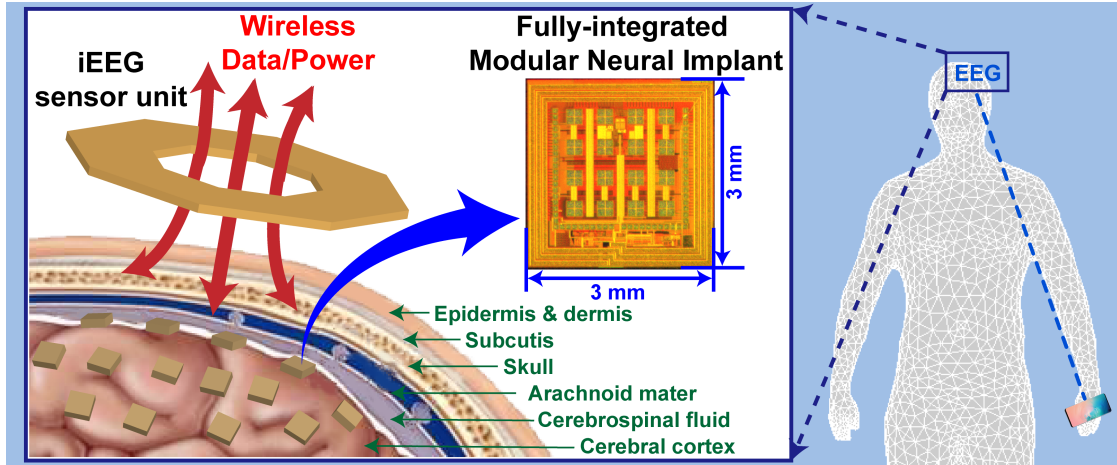


**Figure 1.3:** Another example of short-range wireless communication: mm-scale fully-integrated implantable neural interface

Another example of short-range wireless communication for wearable devices is data transmission for implantable devices. For higher spatial resolution and lower power operation of the wearable medical devices, the bio-interfacing units that provide the stimulation or the data acquisition need to be injected or implanted inside the human body. Here, unlike wired implanted interfaces, the wireless implantable interface significantly reduces infection risk as well as enables freely behaving motion, which finally achieves the portability for wearable medical devices. Figure 1.3 shows an example of wireless implantable bio-sensing applications: implantable neural interface. By implementing the neural implant in a millimeter-scale silicon chip, the interfacing device can be modular, rigid, and small enough to fit in folds and curves of the cerebral cortex, i.e., sulcus. However, since this fully-integrated wireless chip is impossible to employ bulky energy storage such as a battery, wireless data communication must coincide with wireless power transfer via an energy-efficient manner under the regulation for health safety.

This doctoral dissertation presents the energy-efficient schemes for both cases of wireless scenarios for wearable devices. With discussing the challenges of previous human body communication (HBC) approaches for wireless body area networks in Chapter 2, this work describes the theoretical background and its supporting simu-

lation and experiment results of newly proposed wireless technique, magnetic human body communication (mHBC), in Chapter 3. Based on the analysis of mHBC, Chapter 4 shows the design procedure and the measurement results of the ultra-low-power transceiver exploiting the energy-efficient mHBC channel link, while successfully validating that mHBC can be implemented in the practical application with audio streaming demonstration. Finally, Chapter 5 provides the antenna design guideline to maximize the power transfer efficiency of wireless data/power delivery to the on-chip coil employed in mm-scale implantable neural interfaces.

# **Chapter 2**

## **Channel Modeling of Capacitive-Coupled Electric Human Body Communication Link for Wearable Applications**

Wearable devices used in applications ranging from wellness/fitness, augmented reality, healthcare diagnostics, prosthetics and beyond typically require communication of sensed information around a local Body Area Network (BAN). Since such devices are designed to be small to fit anatomical constraints, battery capacity is generally limited, thereby necessitating low-power load circuits. Incumbent communication circuits, typically operating via propagation of radio frequency (RF) electromagnetic energy, have significant losses when operating around the human body. For example, a 2.4 GHz radio communicating over 1 m nominally has a path loss of 40 dB in free space; however, this can increase to upwards of 85 dB due to the body shadowing effect [1, 2]. Such large path loss variation demands either a high transmitted output power and/or a very sensitive receiver operating over a large dynamic range, both of which require substantial circuit power consumption. In addition, the inherent broadcast nature of RF necessitates mechanisms to secure data transmissions and cooperate with nearby users, requiring further power from small wearable batteries.

To reduce the power required to communicate in a BAN, it has been shown that the human body itself can be employed as the communication medium [3]. Since most biological tissues are conductive, such human body communication (HBC) schemes can,

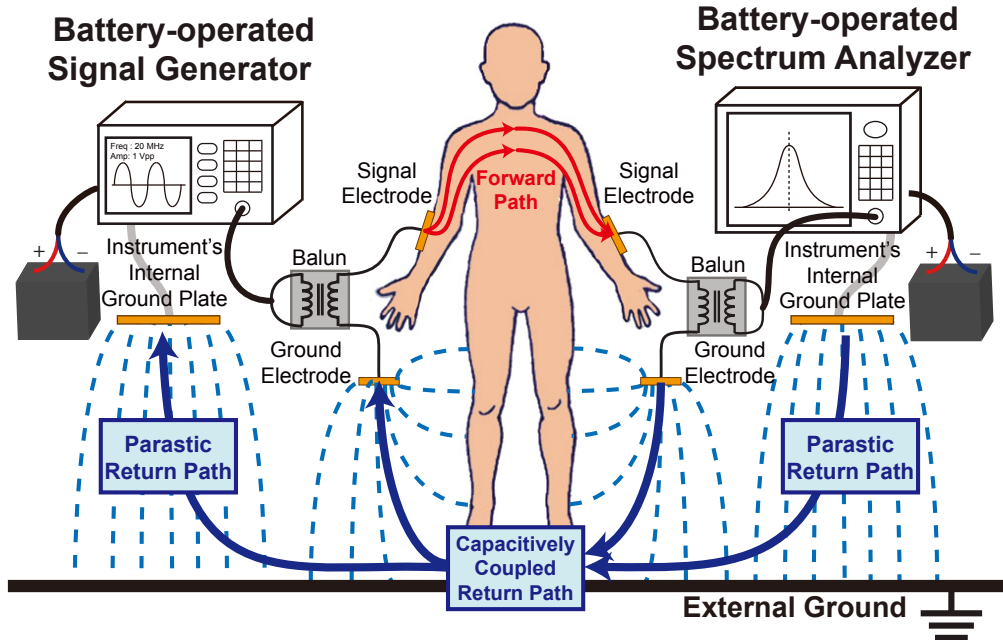


**Figure 2.1:** Conventional HBC path loss measurement configuration using the battery-operated instruments

in principal, offer a more direct route for signal energy to transfer between a transmitter (TX) and a receiver (RX), thereby potentially decreasing path loss and reducing the required power consumption of communication circuits. In addition, energy is more localized to the individual, potentially easing multi-access and security concerns that otherwise plague over the air (OTA) solutions.

There are two primary forms of HBC: galvanic and capacitive coupling. Galvanic HBC systems directly pass small currents through tissue, and are thus suitable for both wearable and implantable devices. However, galvanic HBC has been shown to be optimal at relatively low frequencies (hundreds of kHz), thus limiting bandwidth to support higher data throughputs [4]. Further, galvanic coupling has greater path loss compared with capacitive HBC for long distances [4–6]., Capacitive HBC systems operate by coupling energy between the body and the environment, and can have potentially smaller path loss compared with galvanic coupling for communication between distal areas across the body [5]. In addition, it has been shown that capacitively coupled systems can operate optimally at higher frequencies (tens of MHz), enabling higher-bandwidth

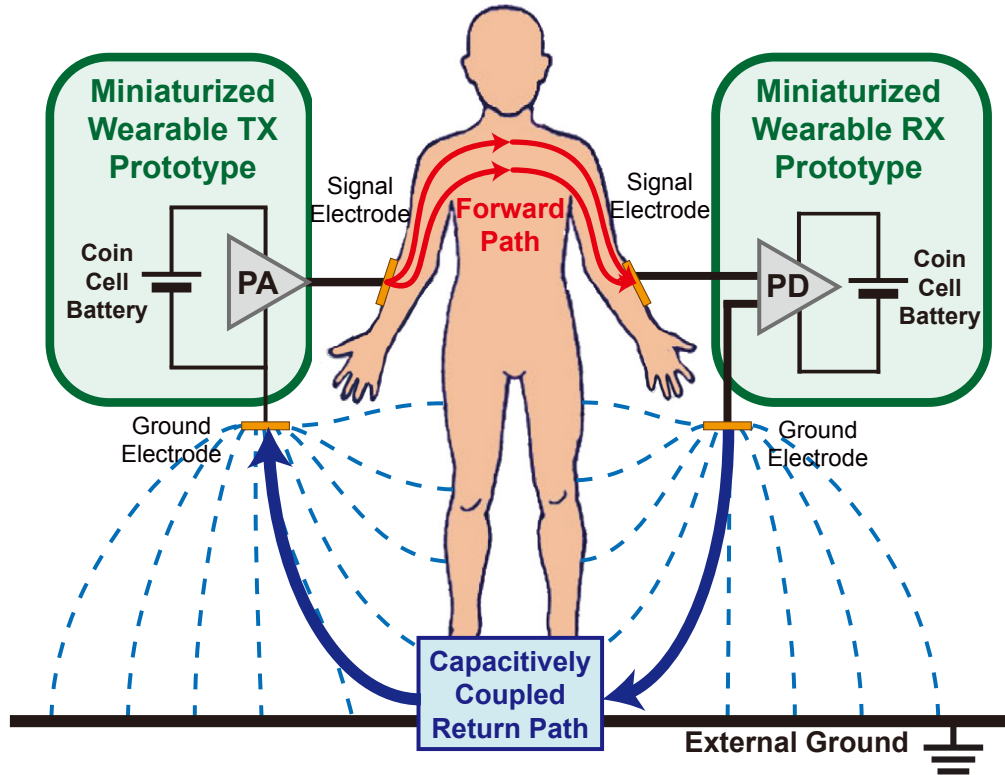


**Figure 2.2:** Proposed measurement setup using the battery-operated wearable prototypes for the accurate HBC path loss estimation.

wearable applications [6]. For these reasons, capacitive HBC systems are the focus of this work.

In order to estimate path loss in capacitive HBC links, it is necessary to use realistic form factors for the TX and RX units. While path loss measurements and models have been discussed at length in the literature [5–22], there is remarkably little agreement between results, making appropriate system design difficult. Conventionally, path loss measurements are made using a setup similar to what is shown in Fig. 2.1. Here, a benchtop (or portable, battery-powered) signal generator is connected to TX electrodes, and a benchtop (or portable, battery-powered) signal analyzer connected to RX electrodes detects the received signal. Energy is coupled either directly to the electrodes, or via a balun in an attempt to reduce the influence of the instrument ground planes on the measurements. Unfortunately, in all such experiments the ground planes of the

measurement instruments do influence the measurement results by creating a larger than expected return path, thereby underestimating the true path loss. Thus, it is imperative to use form factor-accurate-apparatuses to measure the true path loss of capacitive HBC links in intended devices.

This chapter describes the design and implementation of miniaturized, battery-powered capacitive HBC devices as illustrated in 2.2, and compares the measurement results with setups similar to those reported in the literature. It is shown that inclusion of any additional ground plane area, whether isolated by via a balun or not, serves to underestimate the resulting path loss by up to 33.6 dB in the presented experiments. To further validate the effects of grounding on capacitive HBC systems, and to provide an avenue to quickly and accurately quantify the performance of capacitive HBC links in different configurations, this contribution also introduces a hybrid electrostatic circuit - 3D finite element method (FEM) model for path loss simulations. It is found that simulations match measurement results to within 2.6 dB.

This chapter is organized as follows. Section 2.1 discusses several different measurement techniques employed in prior work. Section 2.2 presents details of the proposed measurement approach, including circuit-level details. Section 2.3 proposes the new hybrid simulation model for path loss estimation in capacitively coupled HBC systems. Section 2.4 presents lab measurements and simulation results. Section 2.5 concludes the chapter and summarizes the steps required to ensure accurate measurements and simulations.

## **2.1 Previous Measurement Configurations**

A capacitive HBC TX transfers energy across the human body by coupling energy to the body via an electrode, and to the environment via a ground plane. Typically, the electrode connected to the body is designed as a planar conductor mounted close to (or touching) the epidermis and carries the analog signal information, while the ground plane is placed facing outwards from the HBC device, thereby acting as an electrode to

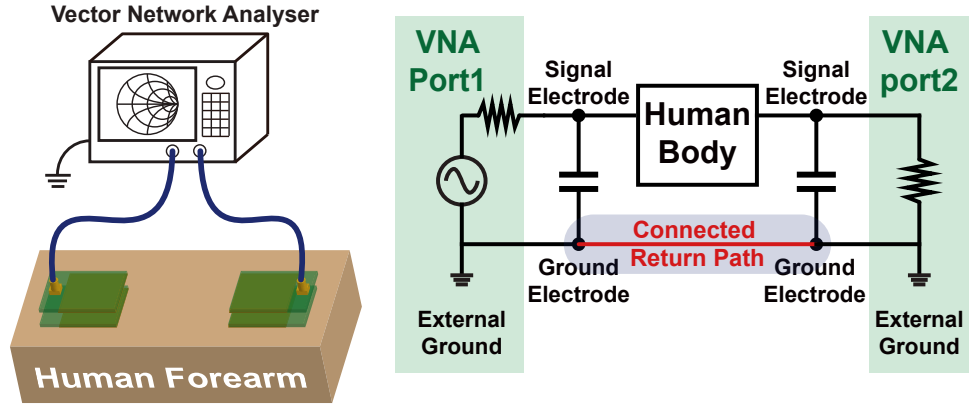
the environment and facilitating a return path. These two electrodes can be driven either single-endedly or differentially. The transmitted signal is then collected by a RX distally mounted on the body with a similar electrode configuration: the body-facing electrode receives the forward path information, while the environment-facing electrode receives the reference potential (or negative differential signal) via the return path by capacitive coupling.

Under practical constraints, capacitive HBC systems are typically employed to provide communication functionality to small, battery-powered, wearable sensing devices, as shown in Fig. 2.2. To measure and model the HBC channel, prior work has suggested the use of large bench-top devices such as Vector Network Analyzers (VNAs) or Signal Generators (SGs) and Spectrum Analyzer (SAs) as shown in Fig. 2.1. This section summarizes these measurement approaches and discusses in detail why they will give overly optimistic path loss results for small, wearable devices.

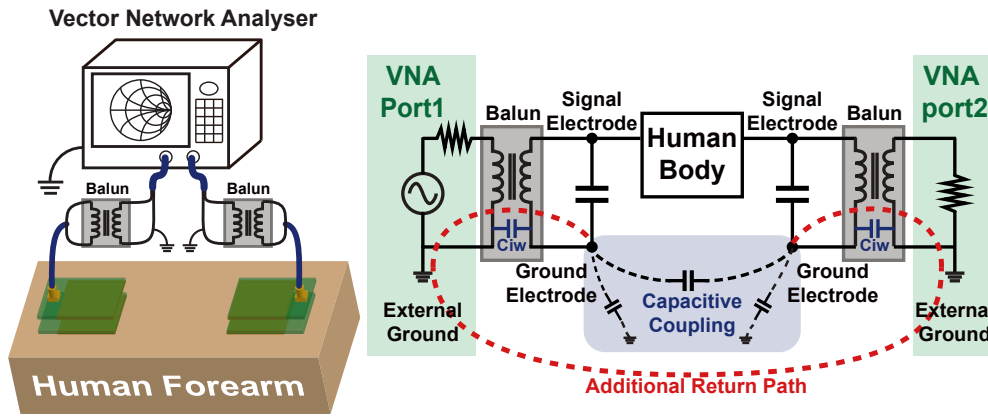
### **2.1.1 Measurements with a Vector Network Analyzer**

A VNA is a natural first choice to model the path loss of an HBC system, as impedances, path loss, and maximum available gain (MAG) can be easily computed via measured  $S$ -parameters. For these reasons, the earliest work to model capacitive HBC link employed a VNA in the general configuration illustrated in Fig. 2.3a [7, 8]. However, unlike conventional far-field wireless communication systems that have stable, independent grounds, the ground of a capacitive HBC system can dramatically affect link characteristics. Employing a VNA as illustrated in Fig. 2.3a creates a non-isolated, direct return path between the ground electrodes of the TX and RX nodes via instrument ground, thereby significantly underestimating the path loss compared to employing two completely isolated TX and RX devices.

To improve path loss estimation, it has been suggested to electrically isolate the two capacitive HBC devices via baluns placed at the VNA ports as illustrated in Fig. 2.3b. Prior work has suggested that this eliminates the direct return path [9], and



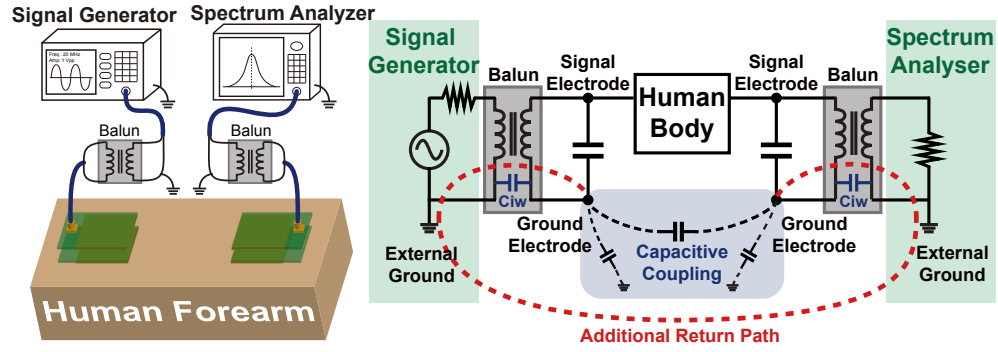
(a) Direct VNA connection



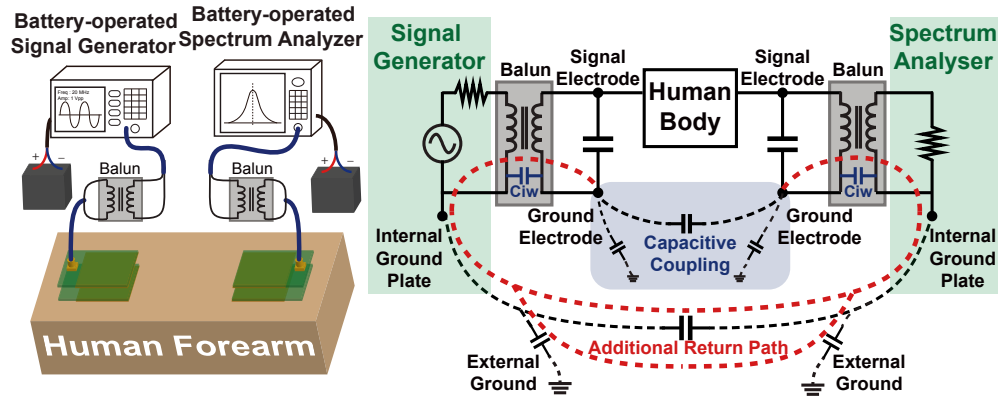
(b) VNA connected to TX and RX electrode pairs via two baluns

**Figure 2.3:** Conventional setups used to measure capacitive HBC links with a vector network analyzer, and their equivalent circuit models

has thus been utilized to report various channel modeling results [5, 10, 11]. While use of baluns indeed eliminates the direct return path connection, there is still a large *indirect* return path via the non-zero coupling through the employed baluns. It has been recently reported that the parasitic coupling path through the balun limits the accuracy of path loss measurements for wearable HBC systems [12]. As illustrated in Fig. 2.3b, the balun includes the interwinding capacitance ( $C_{iw}$ ) that inevitably occurs due to the physical proximity of two coils inside the balun. This parasitic path indirectly connects the ground HBC electrodes to instrument ground, which can result in a lower impedance connection than that of the return path via the external environment, thereby resulting in a measurement that does not accurately reflect the performance of small, miniaturized,



(a) an SG connected via a balun to the TX and an SA connected to the RX with a balun



(b) with the SG and SA battery-powered with no building-ground return path

**Figure 2.4:** Conventional setups used to measure capacitive HBC links with a signal generator and a spectrum analyzer, and their equivalent circuit models

battery-powered wearable HBC devices.

## 2.1.2 Measurements with Signal Generators and Spectrum Analyzers

To avoid even an indirect return path through instrument ground, prior work has suggested using two separate instruments to measure the capacitive HBC channel performance: an SG and an SA [6, 7, 13]. Although this configuration splits the TX and RX nodes to two different instruments, the ground electrodes are still connected to a common ground via parasitic or direct paths through each instrument (to earth or building ground), as illustrated in Fig. 2.4a. For this reason, other prior work has suggested

employing baluns to eliminate any direct DC return paths [5]. However, the parasitic interwinding capacitance problem remains, and thus this approach still does not offer sufficiently accurate measurements for small battery-powered wearable HBC devices.

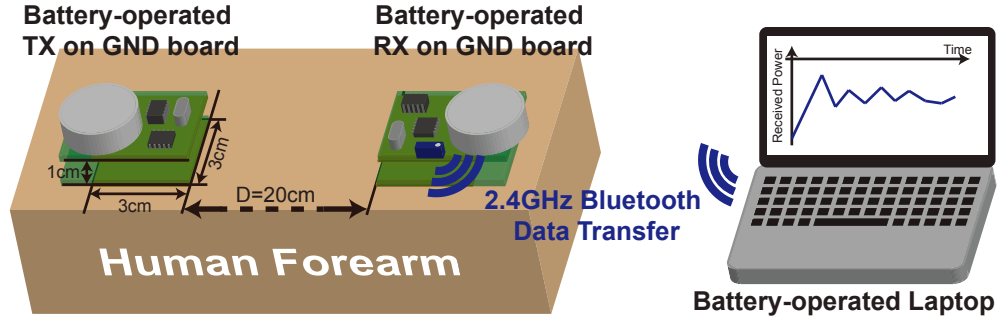
In order to eliminate the influence of instrument-based connection to earth or building ground, recent studies have employed battery-operated SGs and SAs, as illustrated in Fig. 2.4b. While this results in a slightly more realistic configuration to predict the path loss of small battery-powered wearable HBC devices, the employed measurement instruments are not nearly as small as the wearable devices that will eventually be used. Since the SG and SA both have large ground planes that are much larger than the ground electrodes on a miniaturized wearable HBC device, return path coupling to the environment is larger in this setup, resulting in an underestimation of path loss. To minimize this parasitic return path, several studies have employed a miniaturized battery-operated TX [14, 15]. However, a large ground-connected SA was still used as an RX, thereby resulting in a larger-than-desired return path coupling, again underestimating the loss of the end application - a miniaturized, battery-powered wearable HBC device.

## 2.2 Proposed Measurement Configuration

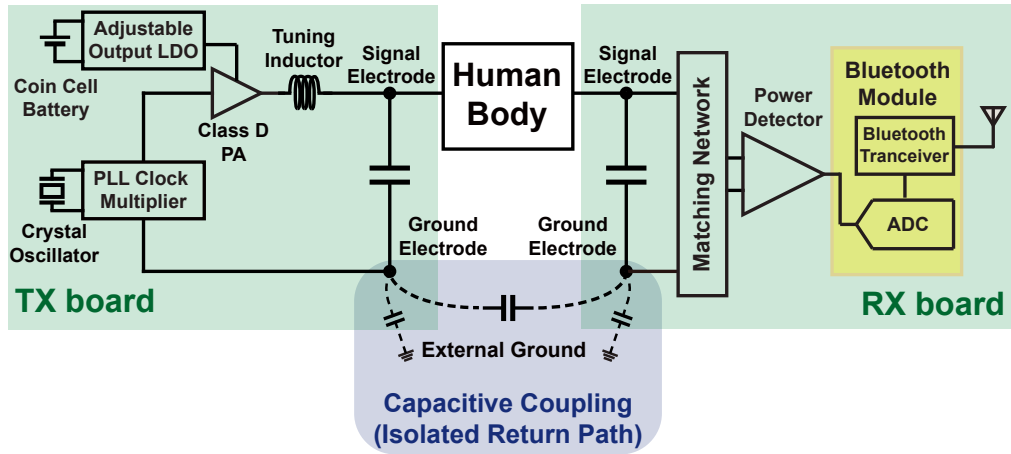
The best way to measure the channel characteristics of a capacitive HBC link amongst miniaturized wearable devices is to employ miniaturized wearable devices with representative form factors. In this manner, grounding effects, which are critically important in assessing performance as will be shown in Section 2.4, will be representative of practical implementations.

To this end, this section describes a measurement setup that employs miniaturized printed circuit boards (PCBs) with electrodes and electronics that can be used for path loss measurements. The proposed measurement setup is illustrated in Fig. 2.5a, and the system block diagram and resulting channel circuit model is shown in 2.5b.

The TX and RX devices each consist of two 30 mm  $\times$  40 mm PCBs that are



(a)



(b)

**Figure 2.5:** Proposed measurement setup and its equivalent circuit model

spaced apart by 10 mm as shown in Figs. 2.6a and 2.6b. Each PCB includes a 30 mm × 30 mm metal-plate electrode on the bottom layer finished with lead-free HASL for use as ground or signal electrodes. The PCBs were fabricated using 1.6 mm thick FR4 with 4 layers and 0.1 mm thick (1-oz) copper-wire routing. To ensure no connections were required to external power supplies, computers, or any other devices with large ground planes, the TX and RX devices are both powered via an on-board coin cell battery, and RX data is streamed wirelessly via a Bluetooth Low Energy (BLE) chip for processing on a laptop computer.

The electrode sizes affect path loss in HBC links. In this study, 30 mm × 30 mm electrodes were chosen to balance the amount of required power for reliable communication between TX and RX. Specifically, the 30 mm × 30 mm electrodes can provide

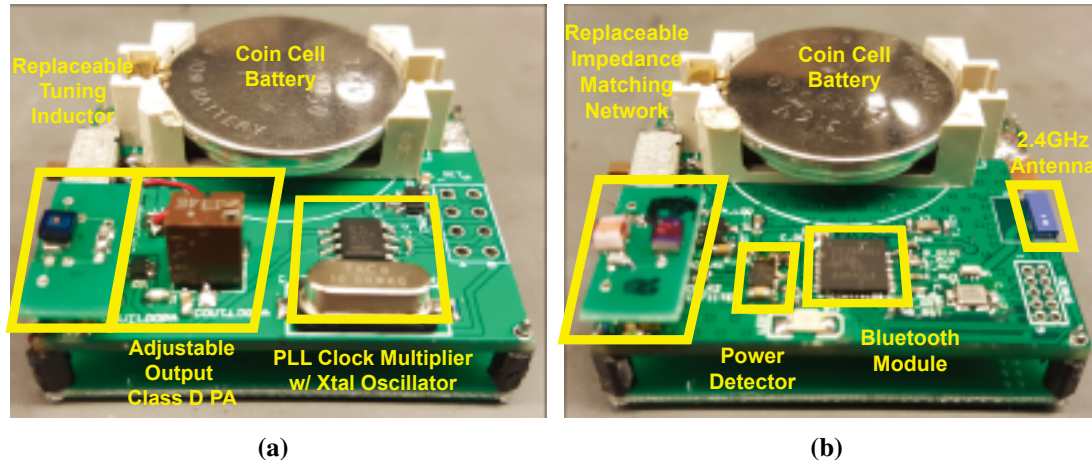


**Figure 2.6:** Photographs of the developed battery-operated HBC wearable prototype of (a) the transmitter unit and (b) the receiver unit

appropriate RX input power range (-30 to -50 dB), which is easily detectable by the employed RX circuitry, for a reasonable amount of TX output power (-10 dBm). While standard self-adhesive Ag/AgCl electrodes were also considered, the adhesive may not be desired in general-purpose consumer applications like smartwatches.

Unlike prior research prototypes that performed channel measurements at one or a limited set of frequencies [15–17], the proposed prototype enables measurement at multiple frequencies thanks to an embedded PLL-based clock multiplier and user-replaceable impedance matching/tuning components. Measurements with this setup were performed with a human subject standing in a typical laboratory environment, but with all grounded equipment in a 4 m × 4 m area removed.

The following subsections describe the employed measurement conditions, and describe the configuration of the TX and RX PCBs.

### 2.2.1 Gain Definition: Power Gain vs. Voltage Gain

There is still active debate on whether voltage or power gain is the best way to characterize an HBC channel: some researchers use voltage gain [5, 10, 18], while others use power gain [6–9, 11, 12, 14–17]. The authors of [19] concluded that voltage gain is more suitable for the description of an HBC channel because their measurements have

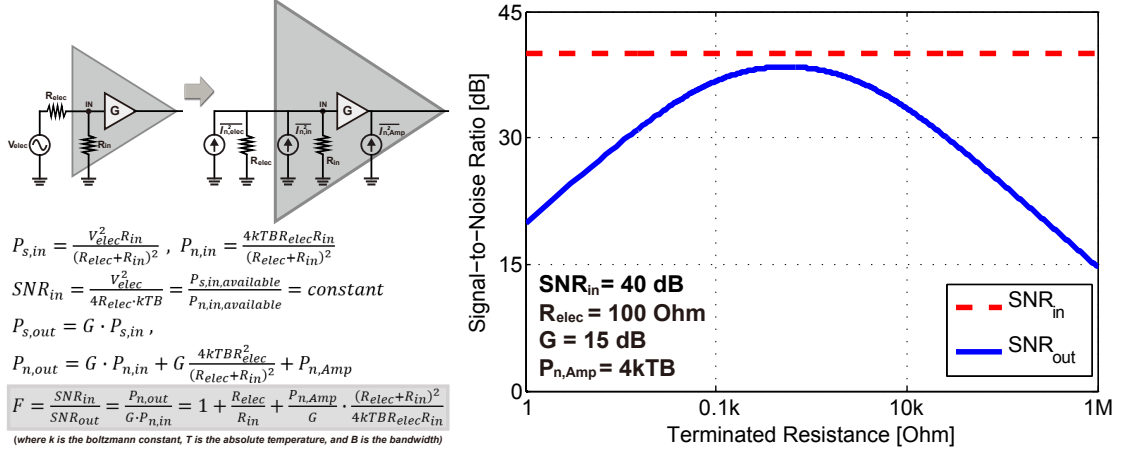


**Figure 2.7:** Simplified RX front-end model and its noise figure analysis result of output signal to noise ratio.

indicated that high RX impedance can deliver superior channel voltage gain.

However, voltage is not typically used to describe the quality of a communication system – Signal-to-Noise Ratio (SNR) is the preferred figure of merit. Employing a high RX input resistance indeed increases voltage gain, though at the expense of reducing the input signal power, which affects SNR. A simple noise model is illustrated in Fig. 2.7. It shows that the signal power reduces with the input resistance of the low noise amplifier (LNA),  $R_{in}$ . Ignoring the noise contribution of  $R_{in}$  (and including only the noise of the electrode resistance,  $R_{elec}$ ), it is shown that the SNR at the input of the RX is constant for all values of  $R_{in}$ . However, when the noise contributions of  $R_{in}$  and the LNA’s finite internal noise are included, it is shown that the noise figure of the system degrades for large  $R_{in}$ . Figure 2.7 plots the input and output SNR of this representative model using the specifications from a commercial off-the-shelf LNA (Analog Devices AD8350). These results reveal that the output SNR, and therefore the noise figure, degrades at high input impedances, thereby degrading the available channel quality for HBC systems.

The optimum output SNR and noise figure occurs at a specific value of input resistance. Thus, we believe that optimization of capacitive HBC links for power gain is the appropriate way to achieve the best possible SNR. For this reason, all measure-

ments in this chapter utilize impedance tuning and matching networks at each measured frequency in order to maximize power gain.

## 2.2.2 Electrode Impedance Measurements

In order to conjugate match the RX electrodes to maximize power gain (and therefore minimize path loss), the impedance of the capacitive HBC electrodes placed on a human body must be first measured. Unfortunately, the impedance of capacitive HBC electrodes can vary under different environmental conditions and the human body posture. Here, impedance measurements were taken using a VNA, and several representative measurement results are shown in Fig. 2.8. Such measurements were repeated over the course of six days, with each day comprising 20 measurements. The standard deviations averaged over 1 - 150 MHz are measured as  $19.04 \Omega$  for  $R_{TX}$ ,  $22.49 \Omega$  for  $X_{TX}$ ,  $35.48 \Omega$  for  $R_{RX}$ , and  $87.29 \Omega$  for  $X_{RX}$ .

Interestingly, it was found that the measured impedances exhibited a resonant peak at approximately 50 MHz. It is hypothesized that this is due to resonance between the body and the VNA itself (which has a large ground plane). A similar effect was also observed in the literature, as reported in [23]. Since this resonance is not expected to be seen by the miniaturized devices, it is useful to fit the general shape of the measured curves prior to developing frequency-specific matching networks. Using the

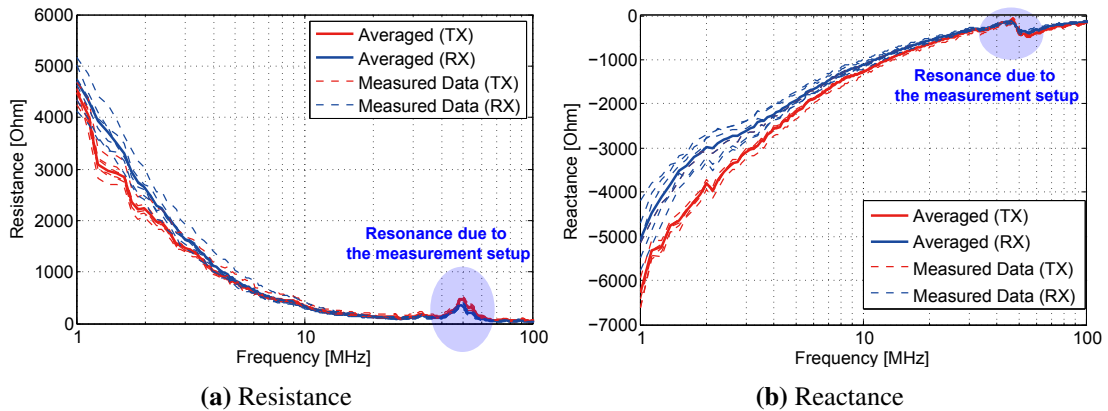


**Figure 2.8:** Multiple measurements of the impedance of HBC electrode pairs.

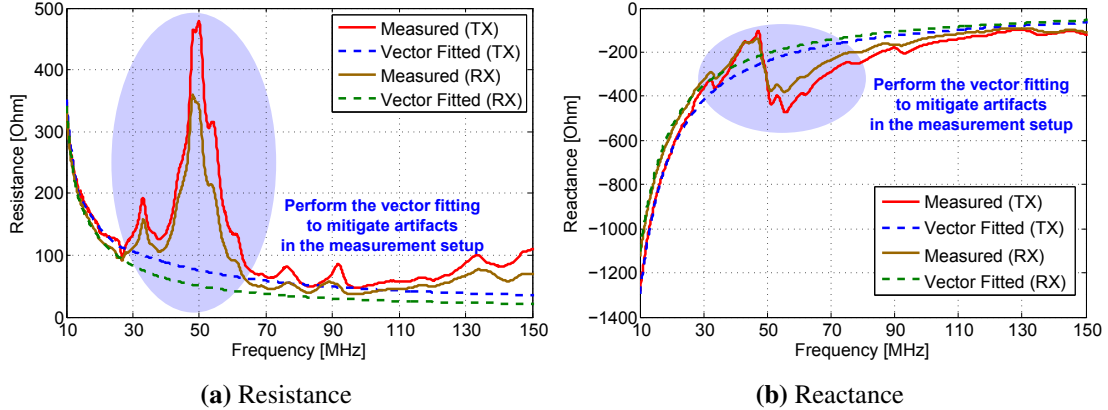


**Figure 2.9:** Vector fitting the averaged measured impedance

vector fitting approach described in [24] results in the zoomed-in curves shown in Fig. 2.9. These curves are then used to compute the impedance and resonate the TX and perform conjugate matching for the RX device.

### 2.2.3 Transmitter Circuitry Configuration

The TX architecture is shown in Fig. 2.10. The TX drives the electrode pair in a single-ended manner via a class-D power amplifier (PA). The PA comprises N & P-channel power MOSFETs (Fairchild semiconductor FDG6332C). Since the  $R_{on}$  of these power switches is low (up to  $0.7 \Omega$ ), it is not necessary to conjugate match to the electrode impedance, but instead it is best to simply tune-out the reactance of the electrode impedance as is typically done in PA design. At resonance, the delivered output power can be computed by dividing the square of the RMS output voltage by the electrode resistance. Power can then be controlled by either varying  $V_{DD,PA}$ , which is generated by an adjustable low-dropout (LDO) regulator (Texas Instrument TPS73601) powered from the battery, or by building a resonant impedance transformer. For simplicity, power is regulated to -10 dBm in this work by tuning the LDO output voltage.

In order to measure path loss at multiple frequencies, the TX is provisioned with a PLL clock multiplier (ON semiconductor NB3N511). With a 10, 12, or 25 MHz crystal reference oscillator, this chip can generate 20, 30, 40, 50, 60, 72, 80, 96, 125 or

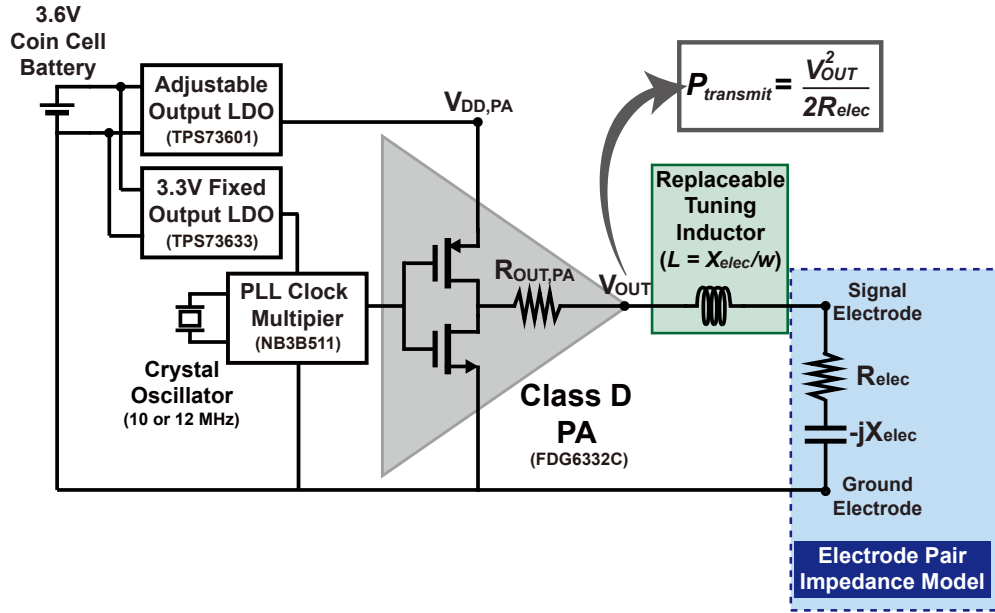


**Figure 2.10:** Prototype TX circuit configuration for operation at multiple frequencies and its transmitting power definition.

150 MHz signals depending on its pin configuration. The chip is powered by a 3.3 V fixed output LDO (Texas Instrument TPS73633). Each frequency configuration requires a different tuning inductor, which is soldered on the small daughter board and replaced for each discrete frequency measurement.

For the specific example of 20 MHz operation, a tuning inductor of  $4.3 \mu\text{H}$  is employed to cancel out the  $-540 \Omega$  reactance of the electrode pair. The PA was supplied with adjusted  $V_{DD,PA}$  for 160 mV  $V_{OUT}$  amplitude in order to regulate the output power of the  $127 \Omega$  load to 0.1 mW ( $-10 \text{ dBm}$ ) [25].

## 2.2.4 Receiver Circuitry Configuration

Figure 2.11 shows the schematic of the RX. In order to eliminate the effects of grounded measurement equipment and connecting cables on the path loss measurements, the proposed RX device measures received power using a discrete log power detector chip (Linear technology LT5537FA) and transmits the information using a Blue-

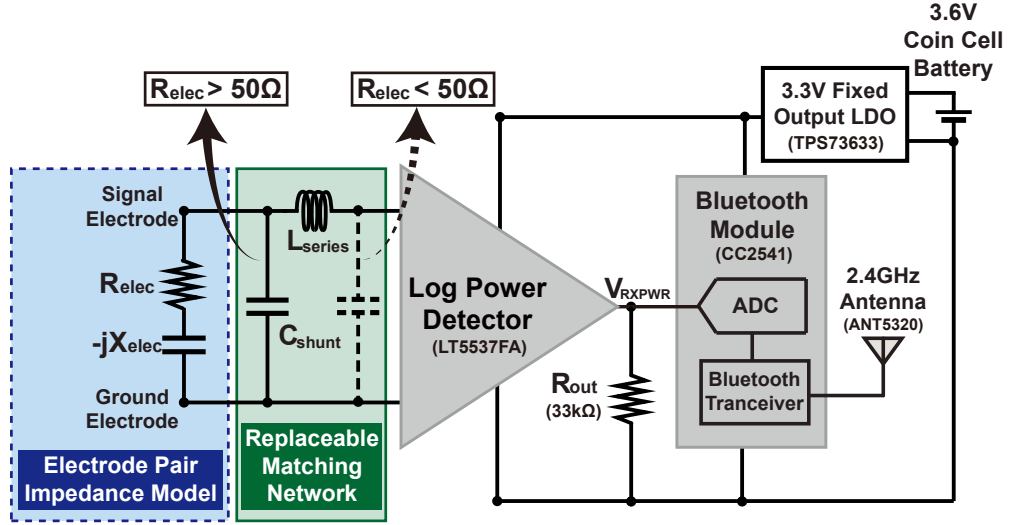


**Figure 2.11:** Prototype RX circuitry configuration with the replaceable matching network for supporting multi-frequency measurements.

tooth Low Energy radio (Texas instrument CC2541) and a 2.4 GHz ceramic chip antenna (Yageo ANT5320) to a battery powered laptop. The laptop was kept at least 3 m away from the TX and RX units during all measurements, as described in Section III. For minimizing the reflected loss of the interface between the input of the power detector and the vector fitted impedance of electrode pairs (shown in Fig. 2.9), the matching networks for each measured frequency are soldered on the replaceable daughter boards.

**Table 2.1:** Impedance Matching Network Configuration

Freq.	Calculated Ideal		Practical	
	$L_{series}$	$C_{shunt}$	$L_{series}$ (Nominal, Q)	$C_{shunt}$ (Nominal)
20 MHz	2.83 $\mu$ H	8.31 pF	2.79 $\mu$ H (2.7 $\mu$ H, 53)	7.0 pF (6.8 pF)
30 MHz	1.50 $\mu$ H	4.65 pF	1.56 $\mu$ H (1.5 $\mu$ H, 61)	3.8 pF (3.9 pF)
40 MHz	0.933 $\mu$ H	2.64 pF	0.98 $\mu$ H (1.0 $\mu$ H, 45)	1.8 pF (1.8 pF)
50 MHz	0.642 $\mu$ H	1.19 pF	0.66 $\mu$ H (0.68 $\mu$ H, 48)	0.59 pF (0.6 pF)
60 MHz	0.473 $\mu$ H	73.8 fF	0.46 $\mu$ H (0.47 $\mu$ H, 50)	0.58 pF (0.6 pF)
72 MHz	0.362 $\mu$ H	16.7 pF	0.35 $\mu$ H (0.33 $\mu$ H, 42)	9.6 pF (10 pF)
80 MHz	0.3 $\mu$ H	19.5 pF	0.29 $\mu$ H (0.3 $\mu$ H, 30)	12.8 pF (13 pF)
96 MHz	0.215 $\mu$ H	21.5 pF	0.213 $\mu$ H (0.22 $\mu$ H, 57)	19.1 pF (18+0.8 pF)
125 MHz	0.13 $\mu$ H	21.2 pF	0.137 $\mu$ H (0.15 $\mu$ H, 63)	18.9 pF (18+0.5 pF)
150 MHz	91.1 nH	19.7 pF	90.8 nH (91 nH, 49)	18.4 pF (18 pF)

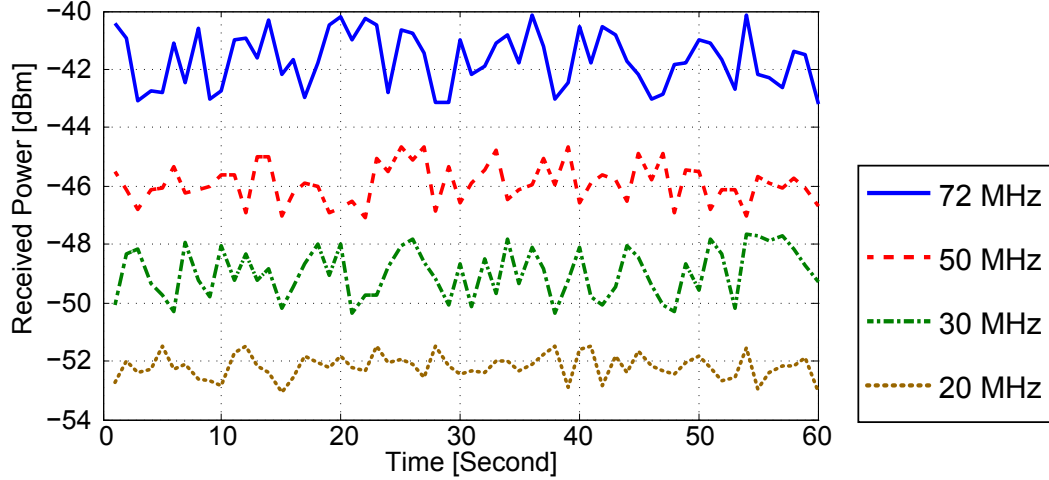


**Figure 2.12:** An example of power measurements using data received from the RX prototype operating at different frequencies.

As shown in Table 2.1, these single-stage L-matching networks are designed with series inductors and shunt capacitors for below -20 dB of reflected loss. All chips in the RX board are powered by a 3.3 V fixed output LDO (Texas Instrument TPS73633) connected to a 3.6 V coin cell battery. Fig. 2.12 shows a time-series measurement of received power, as computed in MATLAB (via the Bluetooth link) every second for 1 minute. These results were used to compute the average and standard deviation of path loss as will be reported in Section 2.4.

## 2.3 Proposed Simulation Model using Circuit & FEM Analysis

### 2.3.1 Hybrid Approach

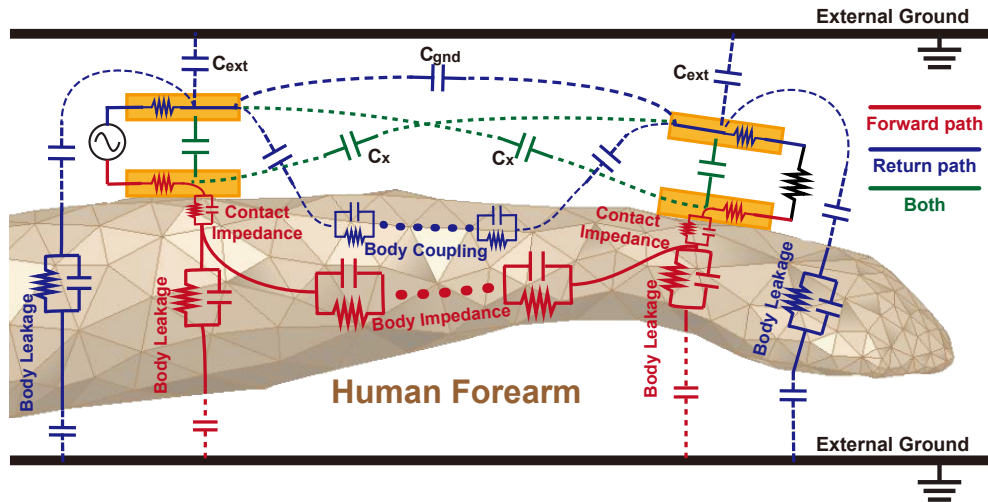
Simulating capacitive HBC links accurately is difficult due to the complicated physics that occurs at the boundary between the metallic electrode and biological tissue, and the complex geometry of the human body's interaction with arbitrary external environments. Previous works in capacitive HBC simulations can be typically broken up into two primary categories: electrostatic circuit analysis, and electromagnetic (EM)

finite element method (FEM) analysis.

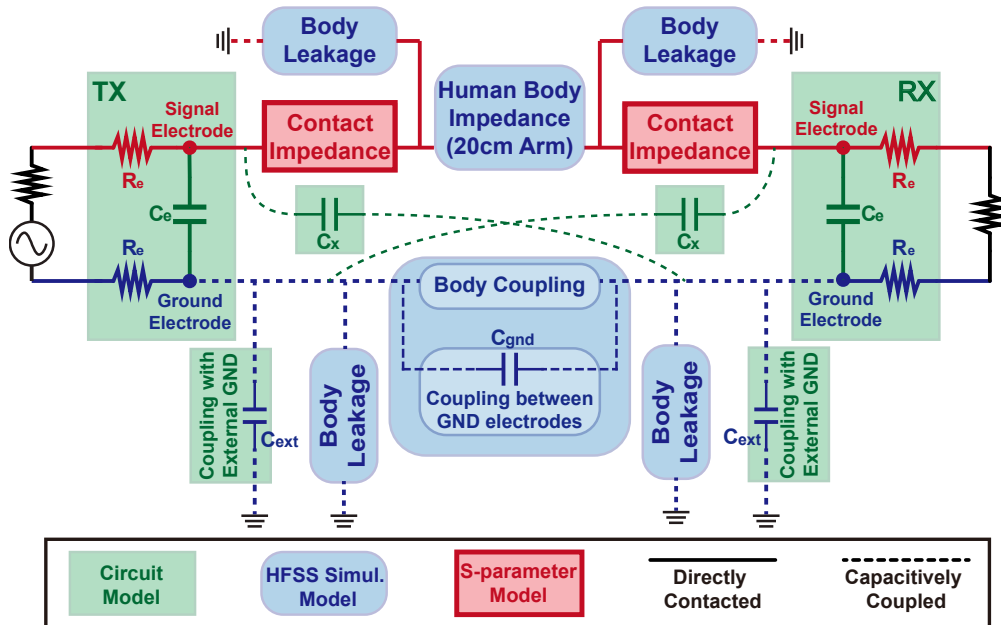
Conventionally, electrostatic circuit analysis can easily characterize the capacitive coupling effects occurring around metallic electrode plates and other conductive media. Under this assumption, prior art has developed distributed electrostatic circuit models based on the frequency-dependent conductive properties of biological tissues, and model the electrode-tissue interface with a complex contact impedance; the tissue-environment interface is then modeled with a capacitive impedance [6,20,21]. However, such models assume a single tissue type, longitudinal transmission over planar tissue geometries, and constant capacitive coupling to the environment, none of which are realistic assumptions. Thus, circuit models alone cannot accurately capture the complex geometries and tissue properties found in real world environments.

To overcome the limitations of circuit models, others have suggested building anatomically-accurate 3D FEM models and performing EM simulations to predict the performance of capacitive HBC links. Such simulation setups can better model the properties of different tissue layers, while also giving a more accurate estimation of the coupling to the environment. However, due to the algorithmic limitation of most EM simulation tools, this analysis method fails to accurately describe ionic conduction and diffusion that occurs at the interface between the electrode and the epidermis (i.e., the contact impedance in electrostatic circuit models), limiting the accuracy of such simulations. Prior work has shown that such simulations can deviate significantly from measurement results [18,22].

To overcome these challenges, Fig. 2.13 proposes a new simulation model that combines the strengths of electrostatic circuit analysis modeling (the electrode-tissue contact impedance) with the strength of FEM EM simulations (the ability to represent complex 3D geometries with accurate tissue properties) in a new hybrid approach that represents the complex behavior of capacitive HBC links much more accurately. Specifically, the proposed model incorporates the results from FEM EM simulations that model tissue properties and environmental coupling, together with measurement-derived  $S$ -parameters modeling electrode-tissue contact impedances, and lumped circuit models



(a) Physical representation of the proposed model



(b) Block diagram of the resulting model as simulated in a circuit simulator

**Figure 2.13:** A hybrid simulation model incorporating electrostatic circuit analysis with FEM EM analysis

describing electrode properties and TX and RX circuits. Each individual path is simulated, then brought together for system-level simulations in a circuit simulator (Cadence Design Environment). This method provides a more accurate path loss model by including all physical phenomenon in HBC channels such as the capacitive coupling amongst metal plates, body leakage and environmental coupling, signal transmission through

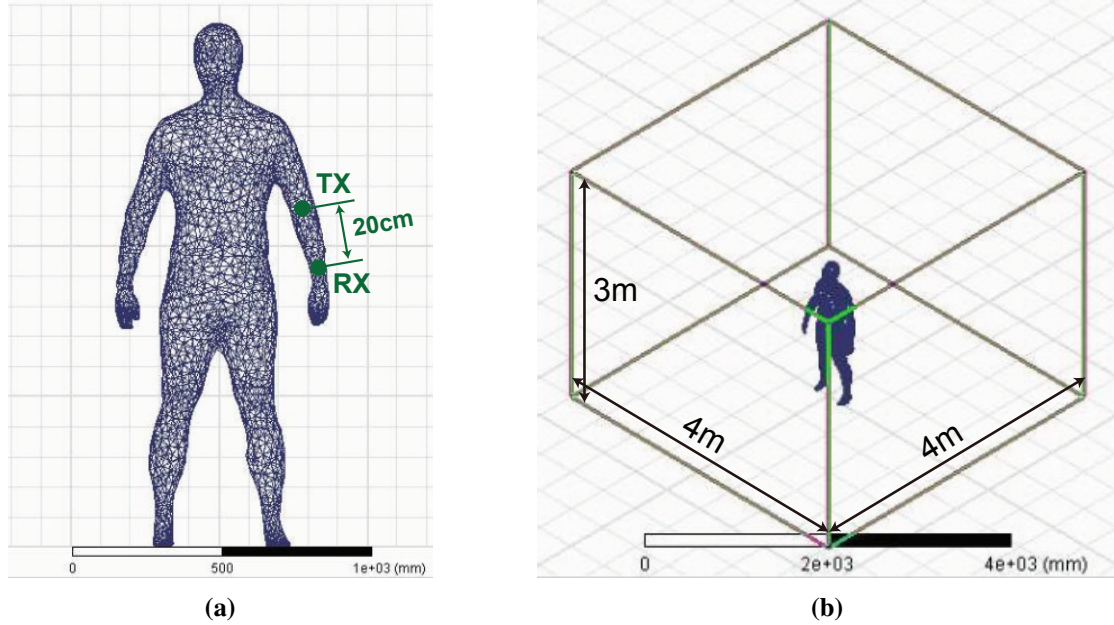


**Figure 2.14:** HFSS simulation model: (a) the realistic human body surface mesh and (b) the external ground model.

complex 3D anatomy, and contact impedances at the electrode-epidermis interface. An overview of the proposed simulation paradigm is shown in Fig. 2.13a, while Fig. 2.13b describes the block diagram used in the circuit simulator. The following subsections describe the methods used to determine each of the blocks found in Fig. 2.13b.

### 2.3.2 Electromagnetic Simulation Model

Figure 2.14a shows the mesh geometry of the 3D FEM simulation model used in this work, based on a 3D scan of a 30-year-old 173 cm-tall male subject [26]. The body was configured to contain biological tissues that were modeled with frequency-dependent relative dielectric permittivity and conductivity [27]. While it was possible to model many different layers of tissue types, simulation time in Ansys HFSS was prohibitive, and thus the properties of all employed tissues were instead averaged across the volume of the human body model. In all simulations, an external ground was implemented as a  $4\text{ m} \times 4\text{ m} \times 3\text{ m}$  perfect conductor box filled with air, as illustrated in Fig. 2.14b, in order to match measurement configurations described in Section 2.2.

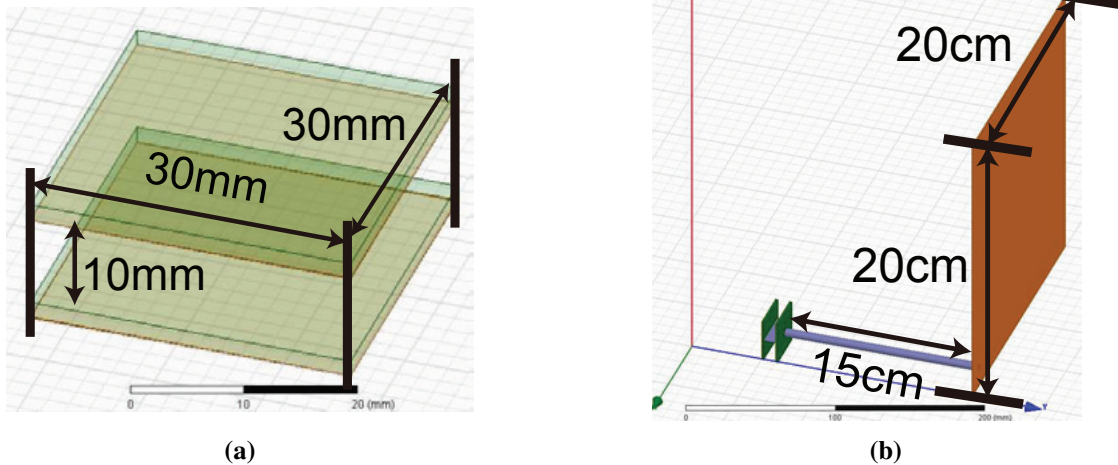


**Figure 2.15:** HFSS simulation electrode model: (a) the HBC electrode pair and (b) the internal ground plate of a spectrum analyzer

The electrodes were modeled as pairs of 30 mm  $\times$  30 mm rectangular metallic plates vertically separated by 10mm as shown in Fig. 2.15a, and placed 20 cm apart on the arm of the simulation subject. Also, a 20 cm  $\times$  20 cm copper ground plate illustrated in Fig. 2.15b is used to represent the additional (internal) ground plane of an SA placed 15 cm away from the wearable RX prototype in order to simulate the effects of large battery-powered equipment.

To create the composite block diagram depicted in Fig. 2.13b, it is necessary to individually simulate each block in isolation. The human body impedance on the forward path was determined, for example, by placing only the two signal electrodes on the skin and finding the resulting  $S$ -parameters via a HFSS simulation. Similarly, the coupling between the two ground electrodes was simulated using two ground plates that were floating on top of the body in the same position they would normally be during full system operation. The coupling of each metallic electrode to environmental ground via the body (i.e., body leakage) was simulated with each electrode individually. The simulation results of these paths are then combined to create the blue HFSS simulation model blocks shown in Fig. 2.13b. Since all simulations were observed to be linear, and the system is assumed to be time-invariant, superposition of all simulation results is possible.

### 2.3.3 Electrostatic Circuit Simulation Model

The remaining blocks in Fig. 2.13b were determined either analytically, or via measurements. Due to simple geometries, electrostatic circuit models can easily determine the impedances of the electrodes themselves, and the capacitive coupling between the electrodes and the external environment. These results are primarily capacitive and do not change significantly with frequency, as their properties are primarily determined by the physical dimension and positioning of the metal plates. Thus, the green circuit model blocks found in Fig. 2.13b can be represented with simple combinations of resistance and capacitance. Table 2.2 shows the values employed for each of these blocks.

**Table 2.2:** Electrostatic Circuit Modeling Component Values

	Resistance or Capacitance
Electrode Resistance ( $R_e$ )	3.42 $\Omega$
Inter-electrode Capacitance ( $C_e$ )	1.89 pF
Cross-coupled Capacitance ( $C_x$ )	31.9 fF
Ground-coupled Capacitance ( $C_{ext}$ )	1.45 pF

The contact impedance between the metal electrode and the epidermis is, on the other hand, frequency-dependent and difficult to model using conventional EM simulators. Since it is not easy to directly derive a multi-parameter circuit model that accurately describes the frequency-dependent behavior [28,29], 1-port measurements, described in

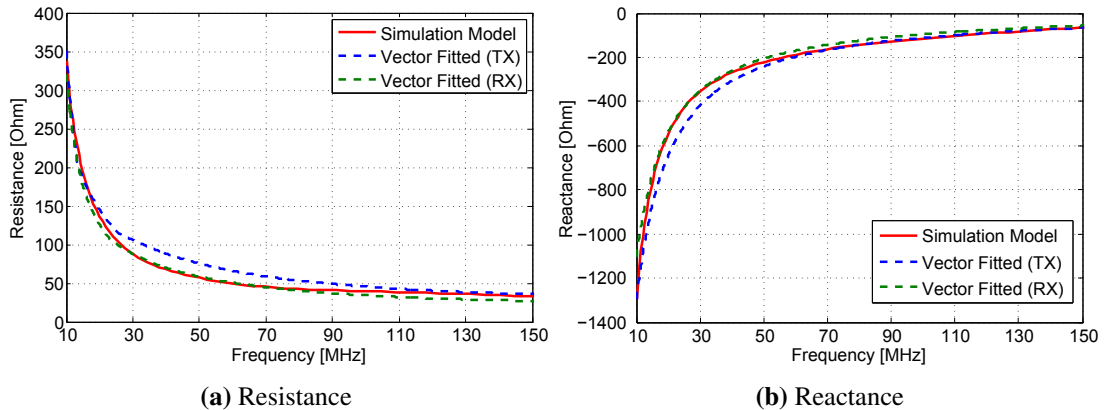


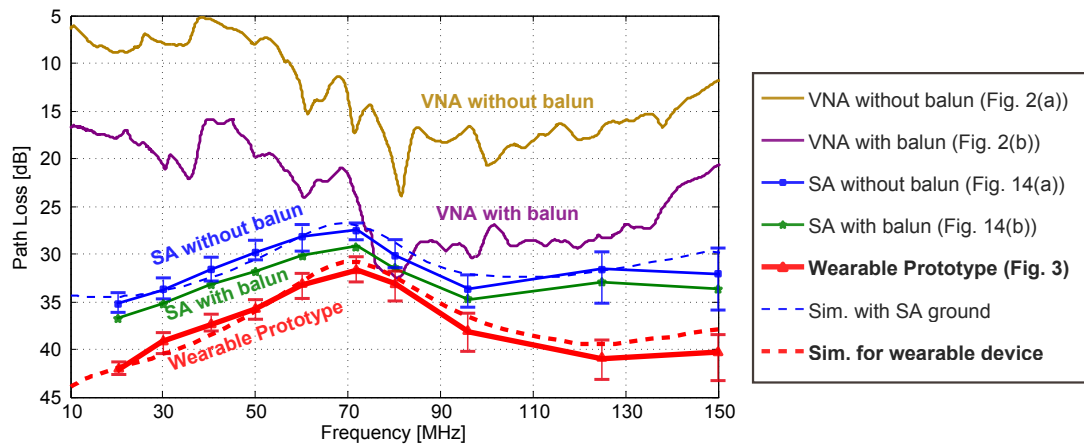
**Figure 2.16:** Measured input impedance of electrode pairs placed on the skin, and the corresponding  $S$ -parameter simulation models.

Section 2.2, are used to create an  $S$ -parameter model that can be directly inserted as the red Contact Impedance blocks into the block diagram of Fig. 2.13b. Measured results from both TX and RX electrodes, and the resulting  $S$ -parameter-based model are shown in Fig. 2.16.

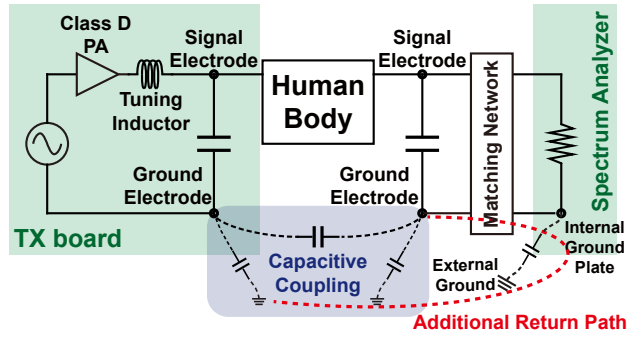
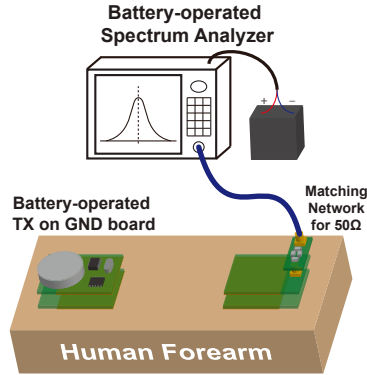
## 2.4 Results

Figure 2.17 summarizes path loss measurements on a human body and simulation results for a variety of instruments and grounding scenarios as described in Sections 2.1, 2.2, and 2.3. The topmost curve (“VNA without balun” in gold) shows measurement results of TX and RX devices directly connected to ports 1 and 2 of a VNA (Keysight E5071C), respectively, as illustrated in Fig. 2.3a. In this configuration, no matching is performed and the TX and RX devices consist only of the two parallel plates and an U.FL connector. Since a VNA is driving the electrodes, path loss is computed via measured  $S$ -parameters using the maximum available gain (MAG) formula (Eqn. 2.1), which gives the best possible path loss result assuming ideal matching.

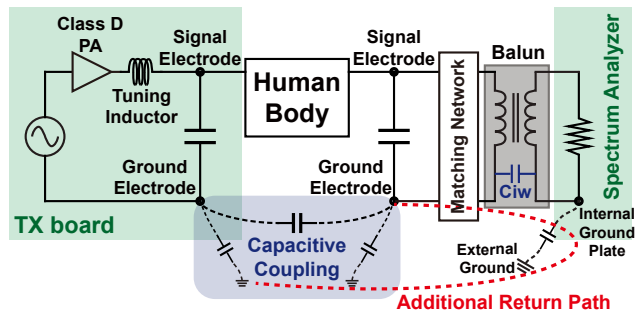
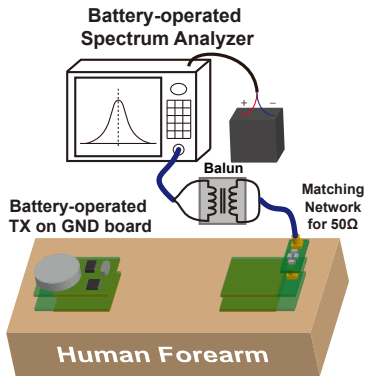
$$MAG = \frac{|S_{21}|}{|S_{12}|} \times (K - \sqrt{K^2 - 1}) \text{ for } K > 1 \quad (2.1)$$



**Figure 2.17:** Measured (solid) and simulated (dashed) path loss results of miniaturized wearable capacitive HBC devices compared to conventional measurement setups using a VNA or a SA.



(a) without a balun



(b) with a balun

**Figure 2.18:** Measurement configurations for the validation of the effect caused by the internal ground plates of large battery-powered spectrum analyzers.

$$\text{(where } K = \frac{1 - |S_{11}|^2 - |S_{22}|^2 + |\Delta|^2}{2|S_{21}S_{12}|} \text{ and } \Delta = S_{11}S_{22} - S_{12}S_{21}\text{)}$$

It can be seen that this configuration is by far the most optimistic, significantly underestimating the path loss due to the direct return path coupling.

The next curve (“VNA with balun” in violet) again utilizes a VNA, but in this case with a balun (Mini-Circuits FTB-1-1 (0.2 - 500 MHz)) inserted between each port in order to isolate grounds at DC, as illustrated in Fig. 2.3b. While this increases the path loss as expected, the coupling through the baluns still presents a low impedance return path at MHz frequencies, again significantly underestimating path loss. Between 10 and 150 MHz, this configuration achieved a minimum path loss of approximately 15.8 dB at 40 MHz.

To decouple the grounds between TX and RX, the next measurement (“SA without balun” in blue) utilizes the battery-powered TX device described in Section 2.2.C, and a battery-powered spectrum analyzer (Anritsu MS2712E), as illustrated in Fig. 2.18a. The TX device was programmed to operate at one of eight discrete frequencies using the on-board PLL clock multiplier, and both the TX and RX matching networks were manually changed and optimized at each frequency. As anticipated, measurement results here show more path loss than when using a VNA due to the decoupled grounds. This approach achieved optimal path loss of 27.5 dB ( $\sigma = 0.8$  dB) at 72 MHz within the measured frequency range (20 to 150 MHz). Path loss was measured by computing power gain of 60-second measurements over three days, and then averages (solid points) and peak variations (error bars) were computed. A simulation model was also constructed under this configuration, whose results are shown as the dotted blue curve (“Sim. with SA ground”). In this case, the simulation setup shown in Figs. 2.14 and 2.15 was employed, though with the ground plate electrode connected to an additional 20 cm x 20 cm ground plate located 15 cm away, representing the internal ground plane of the battery-powered SA as depicted in Fig. 2.15b. Simulation results (MAG from Cadence *S*-parameters simulation) match measurement results to within 2.2 dB across the 20 to 150 MHz frequency range.

An additional experiment was also conducted by connecting the RX to an SA via a balun (“SA with balun” in green) in order to help decouple its large ground plane from the RX as illustrated in Fig. 2.18b. All cases with the battery-powered SA showed larger path loss than the VNA results, however, the results are still optimistic due to the additional coupling path by the internal ground plate of SA.

The final measurements presented here utilize the battery powered TX and RX devices (“Wearable Prototype” in red) as described in Section 2.2 and illustrated in Figs. 2.5 and 2.6. In this case, the TX and RX devices are coupled only via the body and the environment, and are representative of the size of devices that may actually be used in realistic capacitive HBC applications. This case was also measured by computing power gain of 60-second measurements over three days as illustrated in Fig. 2.12. As shown

**Table 2.3:** Measured and Simulated Path Loss of Capacitive HBC Channel

Freq.	Measurement			Simulation	
	Averaged	Peak variation	Std. deviation	Simulated	Diff.
20 MHz	42.2 dB	+0.9 dB / -0.8 dB	0.43 dB	42.0 dB	-0.2 dB
30 MHz	39.1 dB	+1.1 dB / -1.5 dB	0.61 dB	40.5 dB	+0.6 dB
40 MHz	37.5 dB	+1.3 dB / -1.1 dB	0.75 dB	38.6 dB	+1.1 dB
50 MHz	35.8 dB	+1.2 dB / -1.2 dB	0.76 dB	35.9 dB	+0.1 dB
60 MHz	33.2 dB	+1.4 dB / -1.8 dB	0.93 dB	32.8 dB	-0.4 dB
72 MHz	31.7 dB	+1.5 dB / -1.4 dB	1.14 dB	30.9 dB	-0.8 dB
80 MHz	33.1 dB	+1.1 dB / -1.7 dB	1.23 dB	32.2 dB	-0.9 dB
96 MHz	38.1 dB	+2.2 dB / -2.4 dB	1.52 dB	36.5 dB	-1.6 dB
125 MHz	41.0 dB	+2.3 dB / -2.7 dB	1.73 dB	39.4 dB	-1.6 dB
150 MHz	40.3 dB	+1.9 dB / -3.8 dB	2.2 dB	37.8 dB	-2.5 dB

in Fig. 2.17, path loss follows a similar trend vs. frequency as the SA experiments with baluns, yet with path loss results that are 1.6 to 5.5 dB greater. From 10 to 150 MHz, the optimal path loss is 31.7 dB ( $\sigma = 1.14$  dB) at 72 MHz for the 30 mm  $\times$  30 mm electrodes, separated by 20 cm. From this data, path loss results in VNA and SA measurement setups are underestimated by up to 33.6 and 8.2 dB, respectively. Simulation results using the model developed in Section 2.3 match to within 2.5 dB. The results of the wearable, battery-powered configuration are summarized in Table 2.3.

## 2.5 Conclusion

Capacitive HBC links can potentially offer power and interference advantages over conventional narrow-band, over-the-air radio approaches in body-area network applications. Just like any other communication system, link budgets must be understood prior to transceiver design, and thus accurate path loss models in capacitive HBC systems are required. Unfortunately, most prior work has measured the path loss of capacitive HBC systems using large benchtop equipment that significantly underestimates losses through inclusion of unintended coupled return paths. This chapter presents detailed analysis, measurements, and simulations of capacitively coupled HBC systems.

The results reveal that inclusion of large ground planes, whether they are isolated or not with baluns, can significantly affect path loss results. Accurate measurements therefore demand testing apparatuses that are of the same physical size and have the same grounding configurations as devices that will eventually be employed in commercial products. By combining the strengths of electrostatic circuit modeling, which predicts the behavior of electrode-tissue interfaces well, and 3D FEM EM models, which offer more accurate geometric representations, a hybrid simulation model is proposed and shown to be accurate to within 2.5 dB of measurements. In summary, designers of future capacitive HBC systems should:

- employ power gain instead of voltage gain in order to optimize link SNR;
- impedance match the electrode-RX interface to maximize received signal power;
- not characterize capacitive HBC links using VNAs or grounded instruments – baluns help but do not perfectly isolate ground electrodes at MHz frequencies;
- include the effects of internal ground plates of any equipment used to measure path loss;
- simulate path loss using a hybrid electrostatic circuits - FEM EM that captures most physical phenomenon in capacitive HBC systems;
- or employ other coupling mechanisms, such as magnetic resonant coupling [30], which due to their inherently non-referenced nature, eliminate grounding effects altogether and therefore ease modeling and reduce environmental variability.

Chapter Two is largely a reprint of material as it appears in "Channel Modeling of Miniaturized Battery-Powered Capacitive Human Body Communication Systems" by Jiwoong Park, Harinath Garudadri, and Patrick P. Mercier in IEEE Transactions on Biomedical Engineering (TBME), February. 2017. The dissertation author was the primary investigator and author of this work.

## Chapter 3

# Energy-Efficient Intra-Body Wireless Data Transfer via Magnetic Human Body Communication

Wireless communication systems have transformed how humans interact with electronic devices and their environments. Thanks to pioneering work by the likes of Maxwell, Marconi, Hertz, Tesla, and others, wireless systems based on the propagation of far-field electromagnetic (EM) waves are well understood and have been engineered to enjoy robust operation when used with devices that for example continuously monitor electrophysiological processes [31–33] such as electromyogram (EMG), electrocardiogram (ECG), and electroencephalogram (EEG), and physiochemistry such as glucose [34, 35], lactate [36], and electrolytes [37]. However, propagation of far-field radio frequency (RF) energy is inherently inefficient around the human body due to significant energy absorption by relatively highly conductive ( $\sigma=2$  Siemens/m at 2.4 GHz) biological tissue [1, 2] (Fig.3.1a), making the power consumption of conventional radios too high for many miniaturized wearable and medical devices that must support high data rates and long battery life [38]. For example, Fig.3.1b shows the power consumption breakdown of a wireless EEG monitoring device featuring a Texas Instruments CC2642R [39] Bluetooth Low-Energy (BLE) v5.0 module and an Intan Technologies RHD2216 [40] 16-channel EEG front-end. Due to high losses around the human body, the BLE radio is engineered to support an 89-dB link budget, implying a worst-case wireless link efficiency of  $1.3 \times 10^{-9}$ ; as a result, the BLE module consumes up to 90% of the device’s power budget.

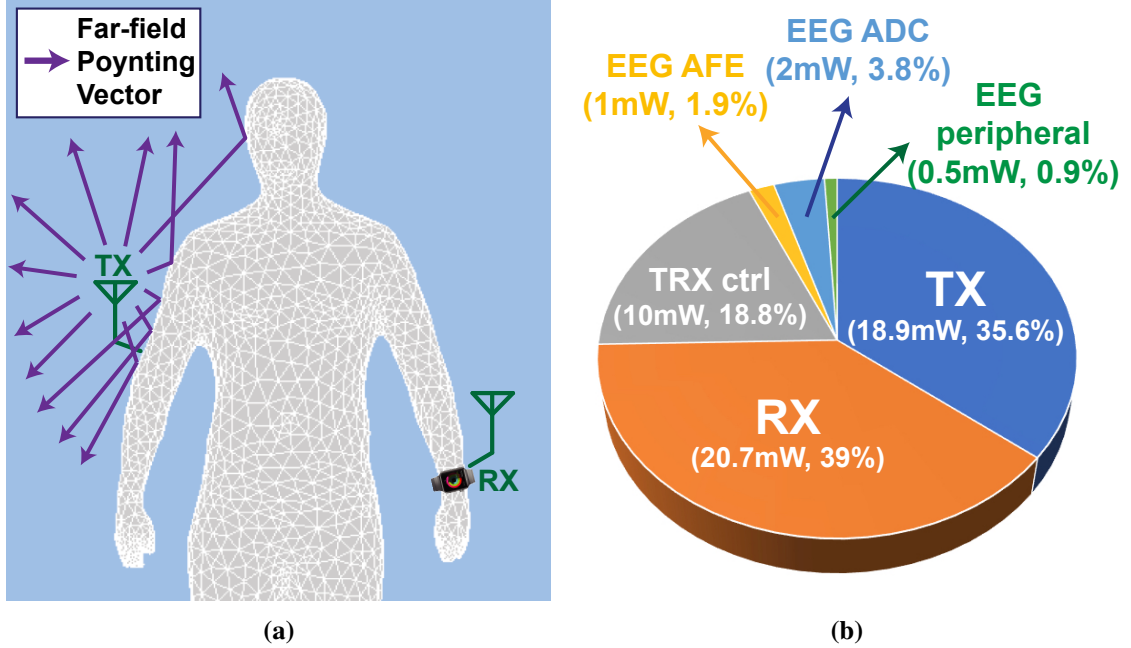


**Figure 3.1:** (a) RF broadcasting communication techniques (e.g. Bluetooth and UWB) and (b) the power consumption breakdown of a wireless EEG monitor system employing a conventional RF (Bluetooth LE v5.0) technique.

This chapter shows that the high permittivity of biological tissue at 10s to 100s of MHz can be exploited to: a) enhance far-field radiation energy inside the human body, which has favorable distal path loss properties (attenuation proportional to  $1/r^2$ ) compared to near-field-only magnetic coupling systems (attenuation proportional to  $1/r^6$ ), and b) help guide generated far-field waves inside the human body in a leaky waveguide-like manner, thereby enabling low-loss intra-body communications for ultra-low power and high energy efficient wireless systems. Since the far-field behavior within a couple of wavelengths (noting that a wavelength  $\lambda$  is 1.6 m in tissue, which has a relative permittivity,  $\epsilon_r$ , or 80 at 21 MHz) cannot be described using conventional dielectric waveguide analysis due to a non-uniform propagating direction (i.e., omni-directional propagation), we developed ray-tracing-like EM analysis techniques to describe the far-field waveguide-like behavior and summed these results with near-field coupling analysis in order to model path loss across a human limb. This analysis is then validated with simulation and experiment, both of which reveal path loss results as low as 10 dB

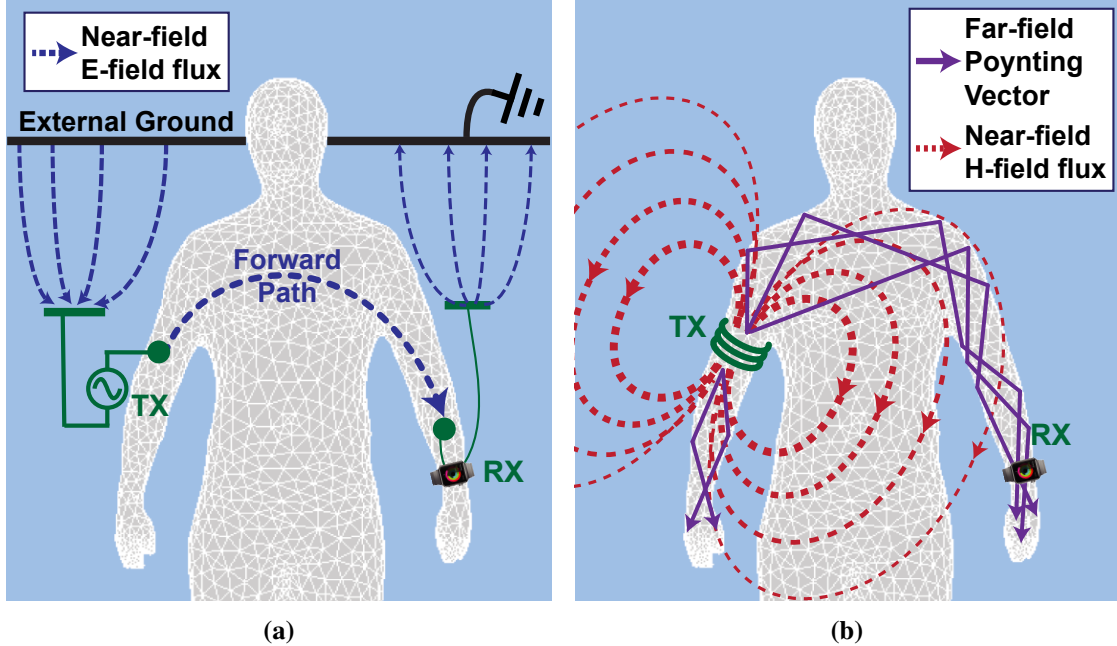


**Figure 3.2:** Human Body Communication: (a) Capacitive-coupled electric HBC (eHBC) and (b) the proposed magnetic HBC (mHBC).

(i.e., a link efficiency of  $10^{-1}$ ) over varying postures when generating magnetic fields using resonantly coupled coils [30, 41]. In contrast, electric human body communication (eHBC) systems, which capacitively-coupled electric fields (Fig.3.2a) into the body, exhibit 30-40 dB path loss, both with significant variability with posture and environment [5, 6, 15, 42].

The proposed magnetic human body communication (mHBC) technique, illustrated in Fig.3.2b, improves intra-body communication efficiency by 1,000-1,000,000 $\times$  over prior approaches, thereby paving the way to new types of ultra-low-power biomedical monitoring devices. Recently, we have successfully developed an experimental microchip that demonstrates a reduction of power dissipation in transceiver circuits to less than  $40 \mu\text{W}$  for a 30 dB link budget (link efficiency of  $10^{-3}$ ) via mHBC [43, 44]; however, the physics of this approach have not yet been investigated. In this chapter, while addressing the theoretical background of mHBC with analysis, simulations, and measurements, an EEG monitoring device is designed with off-the-shelf components to demonstrate the effectiveness of the proposed technique in a representative body-

area network application. Experimental results demonstrate correct and robust mHBC operation, with a  $2,000\times$  reduced transmission power despite a  $1000\times$  worse receiver sensitivity than BLE v5.0 modules, all of which can help enable dramatically improved battery life of wearable devices.

## 3.1 Theoretical Background

### 3.1.1 Characterization of Magnetic Fields in the Human Body

The complex power density (Poynting vector) generated by a generalized magnetic dipole (for mHBC) or electric dipole (for eHBC) is given by:

$$\begin{aligned}\vec{W} &= \frac{1}{2}(\vec{E} \times \vec{H}^*) \\ &= \frac{\eta k^6 I_o^2 a^4}{32} \left\{ \hat{r} \sin^2 \theta \left[ \frac{1}{(kr)^2} + j \frac{1}{(kr)^5} \right] - \hat{\theta} \sin 2\theta \left[ j \frac{1}{(kr)^3} + j \frac{1}{(kr)^5} \right] \right\} \quad (\text{magnetic})\end{aligned}\tag{3.1}$$

or

$$\begin{aligned}&= \frac{\eta k^4 I_o^2 d^2}{32\pi^2} \left\{ \hat{r} \sin^2 \theta \left[ \frac{1}{(kr)^2} - j \frac{1}{(kr)^5} \right] + \hat{\theta} \sin 2\theta \left[ j \frac{1}{(kr)^3} + j \frac{1}{(kr)^5} \right] \right\} \quad (\text{electric})\end{aligned}\tag{3.2}$$

where  $I_o$  is the current magnitude,  $a$  is the radius of loop current,  $d$  is the dipole length,  $k$  is the wave number,  $\eta$  is the radiation impedance,  $r$  is the observation distance, and  $\theta$  is the polar angle of the observation point [45] as derived in Appendix A. Here, the  $(1/kr)^2$ ,  $(1/kr)^3$ , and  $(1/kr)^5$  terms represent the far-field radiation, mid-field induction, and near-field quasi-static components of power density, respectively. Assuming the human body has relative permittivity  $\epsilon_r$ , the complex power density of a magnetic

dipole can be categorized and rewritten with  $k = \sqrt{\epsilon_r}k_o$  and  $\eta = \eta_o/\sqrt{\epsilon_r}$  as follows:

$$Im_{near}(\vec{W}) = \frac{\eta_o k_o I_o^2 a^4}{32r^5} (\hat{r} \sin^2 \theta - \hat{\theta} \sin 2\theta) \quad (near-field) \quad (3.3a)$$

$$Im_{mid}(\vec{W}) = -\hat{\theta} \epsilon_r \frac{\eta_o k_o^3 I_o^2 a^4}{32r^3} \sin 2\theta \quad (mid-field) \quad (3.3b)$$

$$Re(\vec{W}) = \hat{r} \sqrt{\epsilon_r^3} \frac{\eta_o k_o^4 I_o^2 a^4}{32r^2} \sin^2 \theta \quad (far-field) \quad (3.3c)$$

where  $k_o$  is the wave number in free space and  $\eta_o$  is the radiation impedance in free space. Similarly, an electric dipole can be written as:

$$Im_{near}(\vec{W}) = \frac{1}{\epsilon_r} \frac{\eta_o I_o^2 d^2}{32\pi^2 k_o r^5} (\hat{\theta} \sin 2\theta - \hat{r} \sin^2 \theta) \quad (near-field) \quad (3.4a)$$

$$Im_{mid}(\vec{W}) = \hat{\theta} \frac{\eta_o k_o I_o^2 d^2}{32\pi^2 r^3} \sin 2\theta \quad (mid-field) \quad (3.4b)$$

$$Re(\vec{W}) = \hat{r} \sqrt{\epsilon_r} \frac{\eta_o k_o^2 I_o^2 d^2}{32\pi^2 r^2} \sin^2 \theta \quad (far-field) \quad (3.4c)$$

Figures 3.3a and 3.3b illustrate the classified power density of magnetic and electric dipoles, respectively, when placed in either free space or in biological tissue ( $\epsilon_r = 80$  at 21 MHz) with  $d = 1$  cm,  $a = 2\pi$  cm,  $I_o = 1$   $\mu$ A, and  $\theta = 45^\circ$ . Unlike conventional EM systems which operate either in the near- or far-field regimes and thus one of the radiation, induction or quasi-static term dominates, all three terms are comparable at 10s of MHz across the human body ( $r < 2$  m) since the near-field dominant region decreases from  $\sim 2$  m to  $\sim 30$  cm in tissue, and thus conventional EM analysis based on either far- or near-field phenomena is not appropriate. Thus, all analysis of mHBC systems should consider all modes of operation, similar to what is needed in recent work on wireless charging of small implants [46,47].

Interestingly, Fig.3.3a and its corresponding equations reveal that far-field radiation power from a magnetic dipole is enhanced in tissue at human-compatible distances due to the high relative permittivity of tissue; this is also similar as the radiation efficiency enhancement by dielectric loading for electrically-small high- $Q$  loop antenna [48]. The enhanced far-field energy confined in the human body enables body-

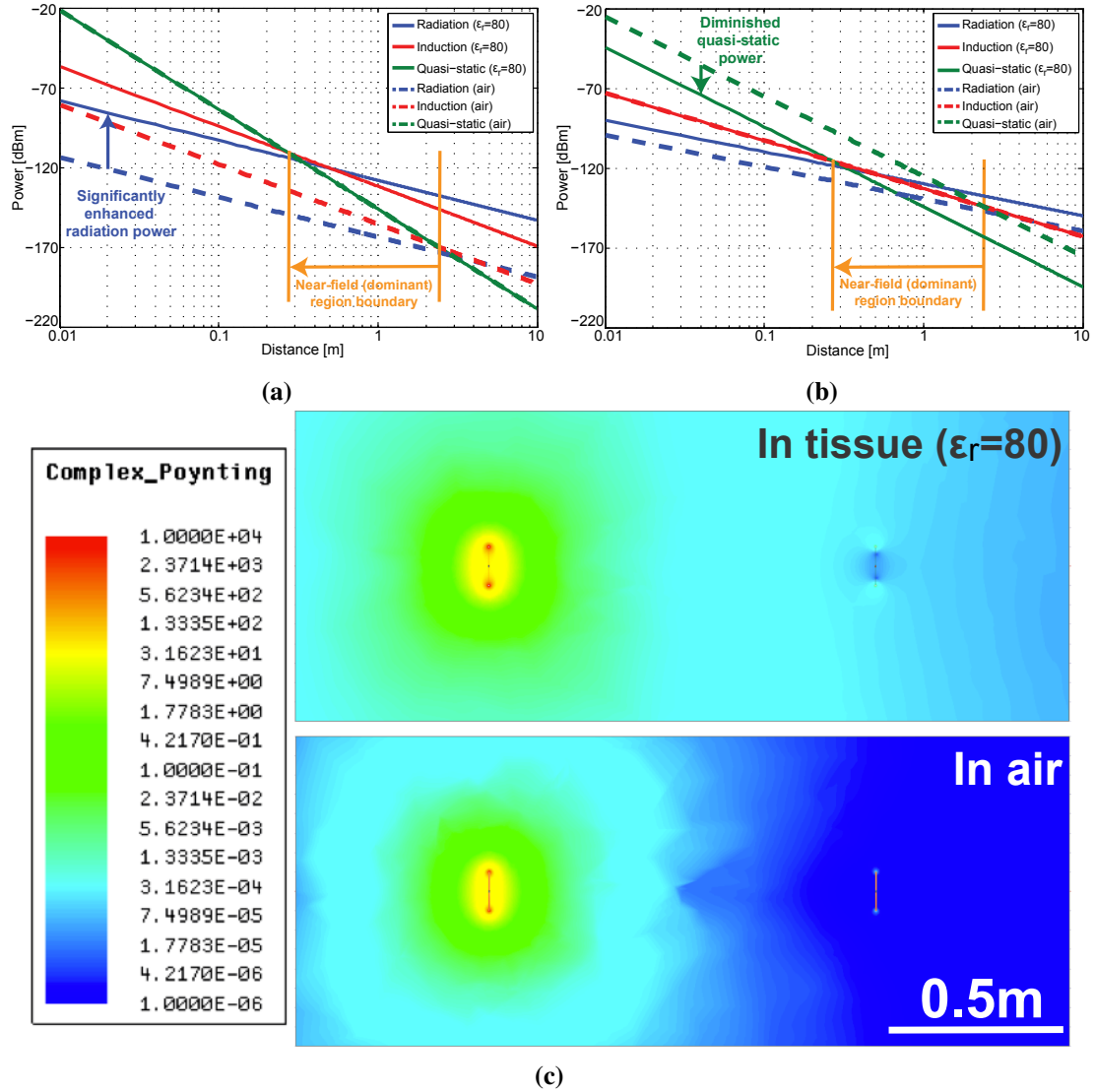


**Figure 3.3:** Classified power density generated by: (a) a magnetic dipole antenna, and (b) an electric dipole antenna placed in biological tissue or in air. (c) 3D FEM simulation results of a magnetic dipole antenna in biological tissue or in air.

range wireless coverage with  $1/r^2$  attenuation in the body and less path loss fluctuation by coil misalignment [49]. 3D finite element method simulations, as shown in Fig.3.3c in free space and in tissue, validate that, for the same amount of input power, the presence of tissue can increase power transfer between coils. In contrast, quasi-static power from an electric dipole degrades inversely proportional to  $\epsilon_r$  in biological tissue, thereby suggesting that mHBC transducers have an intrinsic field-generation-benefit over their

eHBC counterparts. Similar conclusions have been made regarding antennas in seawater [50, 51].

### 3.1.2 Human Body as a Leaky Dielectric Waveguide

When mHBC coils are wrapped around anatomy (e.g., like a wristwatch or a headband), the far-field component of generated EM waves internally reflects between the tissue-air boundary, thereby creating a dielectric waveguide-like effect that serves to guide these waves along the body, ultimately helping to decrease path loss.

To analyze this behavior, first consider a simplified model of a human limb, represented by a cylinder, with TX and RX coils wrapped around as illustrated in Fig.3.4a. In this model, the field excitation of the TX is considered as an ideal magnetic dipole placed at the center of the cylinder's cross-section (i.e., the  $xy$ -plane in Fig.3.4a), which would nominally support a family of circularly symmetric  $TE_{0m}$  guiding modes along the limb under normal circumstances (i.e., at higher frequencies than the cutoff frequencies of guiding modes). However, the  $TE_{01}$  mode (the lowest order mode with magnetic dipole excitation) of dielectric waveguide propagation has a cutoff frequency of  $\sim 260$  MHz for a 5 cm limb radius [52, 53], and thus conventional waveguiding analysis is inappropriate to address wave behavior at 10s of MHz. Although dielectric waveguides operating below the cutoff frequency can still guide waves and be modeled in a leaky mode [54], such classical guide-mode analysis relies on a waveguide that is several multiples of the wavelength long such that all wave vectors can be assumed to have uniform incident direction like a plane wave. In contrast, mHBC typically operates within one wavelength ( $\sim 1.6$  m at 21 MHz in tissue) where the far-field EM waves are radiated omnidirectionally as described in Eqn. (3.3c), and thus a new analytical method is required to deal with the behavior of non-plane waves inside a cylindrical body shape.

To do this, the field pattern of the magnetic dipole can be split into near-, mid-,

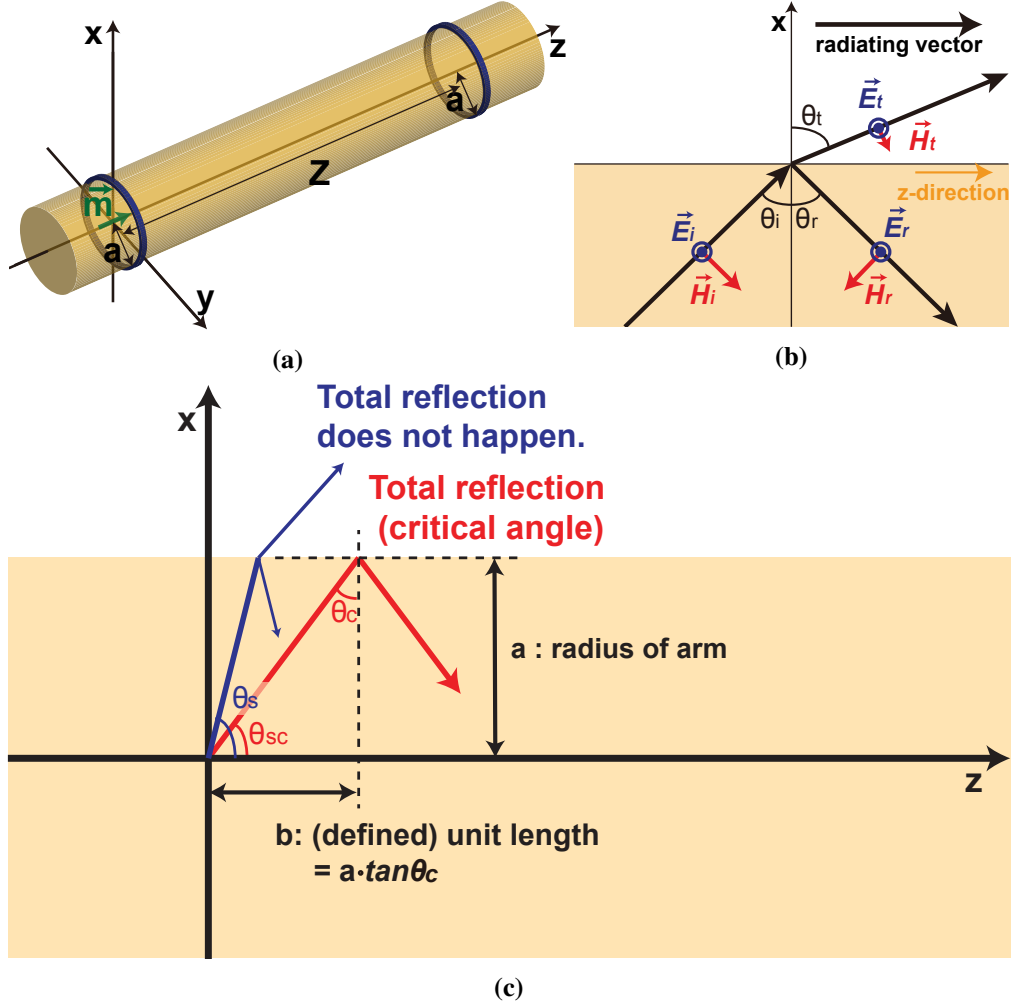


**Figure 3.4:** (a) Analytical model for cylindrical dielectric waveguide of a human limb, (b) incidence, reflection, and transmission of perpendicularly polarized EM wave at the tissue-air boundary, and (c) total reflection condition.

and far-field components:

$$\vec{H}_{near} = \frac{k^3 I_o a^2}{4} \left(\frac{1}{kr}\right)^3 (\hat{r} 2 \cos \theta + \hat{\theta} \sin \theta) e^{-j(kr - \omega t)} \quad (3.5a)$$

$$\vec{E}_{mid} = -\hat{\phi} \frac{j \eta k^3 I_o a^2}{4} \left(\frac{1}{kr}\right)^2 \sin \theta e^{-j(kr - \omega t)} \quad (3.5b)$$

$$\vec{H}_{mid} = \frac{j k^3 I_o a^2}{4} \left(\frac{1}{kr}\right)^2 (\hat{r} 2 \cos \theta + \hat{\theta} \sin \theta) e^{-j(kr - \omega t)} \quad (3.5c)$$

$$\vec{E}_{far} = \hat{\phi} \frac{\eta k^3 I_o a^2}{4} \left(\frac{1}{kr}\right) \sin \theta e^{-j(kr - \omega t)} \quad (3.5d)$$

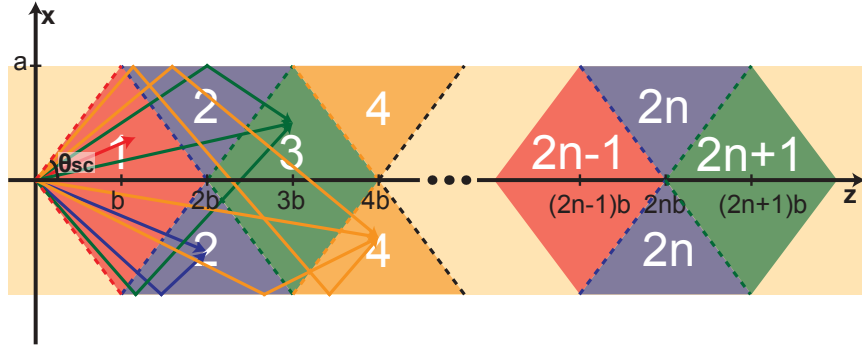
$$\vec{H}_{far} = -\hat{\theta} \frac{\eta k^3 I_o a^2}{4} \left(\frac{1}{kr}\right) \sin \theta e^{-j(kr - \omega t)} = \frac{1}{\eta} (\hat{r} \times \vec{E}_{far}) \quad (3.5e)$$

Here, the near- and mid-field components arising from the magnetic dipole are stored in a reactive power represented as the imaginary part of Poynting vector, and do not reflect at the tissue-air boundary. Thus, the average B-field of the near- and mid-field components can be easily analyzed using the boundary condition for quasi-static E- and H-field (see Appendix B). As illustrated in Fig.3.3a, the power density of the near- and mid-field components at 21 MHz dominate the far-field component in at distances under  $\sim 2$  m in air; however, the enhanced far-field radiation inside the body enables longer communication range because the far-field portion attenuates with  $1/r^2$  rather than  $1/r^3$  (mid-field) or  $1/r^5$  (near-field). In other words, the high permittivity of human tissue at 10s of MHz enables a near-field component that is un-degraded from operation in air, while simultaneously enhancing mid- and far-field components, the latter of which helps overcome the nominal distance restrictions of conventional near-field coupling approaches [41, 46, 47, 55].

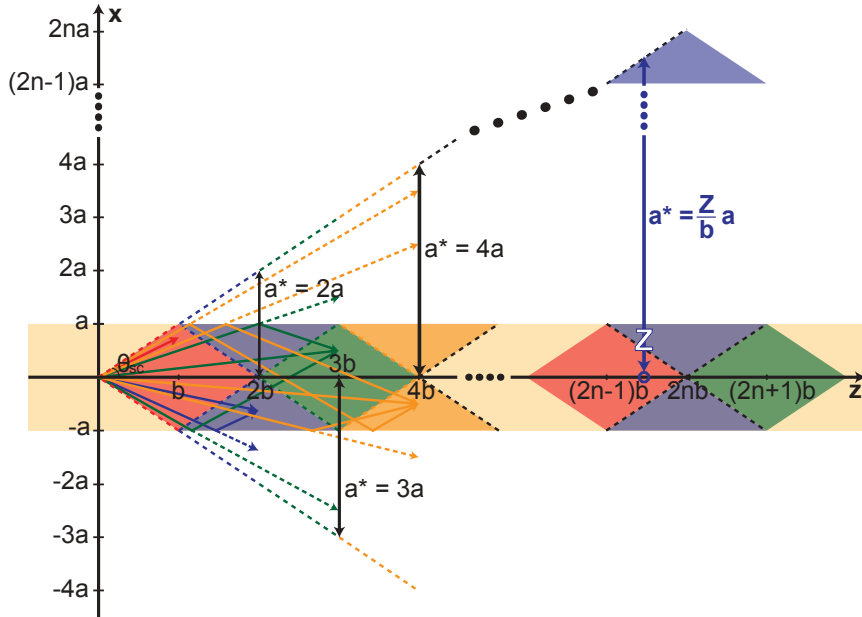
Importantly, the leaky waveguide behavior in the cylindrical limb shape helps to further improve path loss in the region where the far-field radiation dominates over the others (i.e.,  $r > 0.25$  m where  $\epsilon_r = 80$  at 21MHz). Unlike the near- and mid-field components, the far-field components form a transverse EM (TEM) wave along omnidirectional radiation direction vector  $\hat{r}$ , and thus fundamental wave theory regarding the boundary conditions does apply in the far-field in tissue (though the non-uniformity, as described above, requires new analysis). Interestingly, when perpendicularly-polarized TEM waves arrive at the tissue-air boundary, reflection and transmission can occur according to Fresnel equations as depicted in Fig.3.4b and by:

$$\Gamma_{\perp} = \frac{\sqrt{\epsilon_r} \cos\theta_i - \cos\theta_t}{\sqrt{\epsilon_r} \cos\theta_i + \cos\theta_t} \quad (3.6a)$$

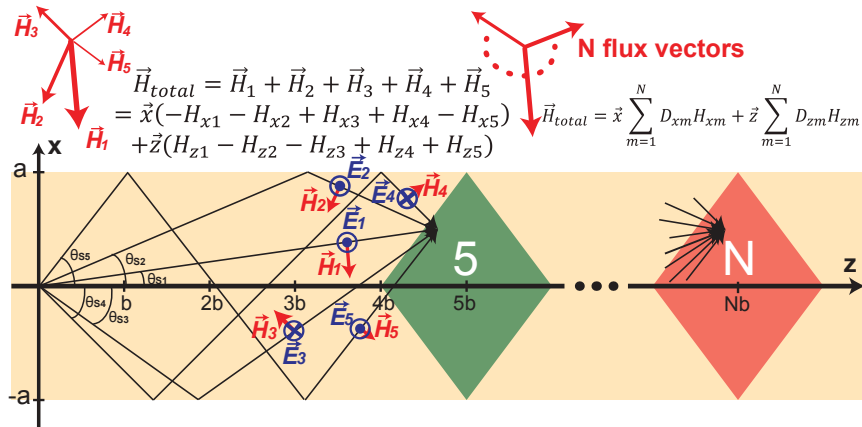
$$T_{\perp} = \frac{2\sqrt{\epsilon_r} \cos\theta_i}{\sqrt{\epsilon_r} \cos\theta_i + \cos\theta_t} \quad (3.6b)$$



(a) Generalization of the number of rays reaching the observing point



(b) Effective-radius model for simplified calculations



(c) Rotating H-fields needed to utilize the simplified model in E

Figure 3.5: Analysis of leaky dielectric waveguide excited by an ideal magnetic dipole.

For total reflection to occur (i.e.,  $|\Gamma_{\perp}| = 1$ ),  $\cos\theta_t$  should be zero or imaginary. With this condition, the critical incident angle ( $\theta_c$ ) can be derived as:

$$\theta_i \geq \theta_c = \arcsin\left(\sqrt{\frac{1}{\epsilon_r}}\right) \quad (3.7)$$

As an example, when the center of a TX coil is placed on the center axis of a cylindrical human arm,  $\theta_c$  is  $6.4^\circ$ , which means that total reflection occurs if the radiation angle from the source ( $\theta_s$ ) is smaller than the critical radiation angle ( $\theta_{sc} = 90^\circ - \theta_c = 83.6^\circ$ ) as depicted in Fig.3.4c. Here, the distance where total internal reflection begins to occur is defined as the unit length,  $b = a \cdot \tan\theta_c$ .

To quantify how total internal reflection serves to fortify magnetic field strength distally along the human body, a ray-trace-like model, shown in Fig.3.5a, is used to average flux density (B) across an RX coil with area  $A_2 = \pi a^2$  based on how many flux vectors, whose numbers increase with unit length  $b$ , reach distance  $z=Z$ . To simplify analysis, an increasing number of totally reflected flux vectors can be summed by a representative model of a cylinder whose radius is effectively expanded ( $a^* = aZ/b$ ) to contain the same total number of flux vectors without reflection as depicted in Fig.3.5b. When the initial radiation pattern has cylindrical symmetry as shown in Eqns. (3.5d) and (3.5e), the far-field propagation in a cylindrical waveguide can be easily described by converting from a cylindrical coordinate system to a rectangular one through the cross-section of the cylindrical medium. Here, to account for the change in vector direction during reflection, it can be shown that the H-field of perpendicularly polarized EM waves on the xz-plane cross-section ( $\phi=0$ ) has only  $\hat{x}$  and  $\hat{z}$  vector components that can be rotated as illustrated in Fig.3.5c and by:

$$\begin{aligned} D_{xm} &= -1 \text{ (when } m = 4n - 3 \text{ or } 4n - 2) \\ &= 1 \text{ (when } m = 4n - 1 \text{ or } 4n) \\ D_{zm} &= -1 \text{ (when } k = 4n - 2 \text{ or } 4n - 1) \\ &= 1 \text{ (when } m = 4n - 3 \text{ or } 4n) \end{aligned} \quad (3.8)$$

where  $n$  is a natural number. The average far-field B-field passing through an RX coil placed at  $z=Z$  in the cylindrical tissue model can then be derived (see Appendix B) as shown below:

$$B_{far,avg}(Z \approx Nb) = B_{x,far,avg}(Z) + B_{z,far,avg}(Z) \quad (3.9)$$

$$(where \ B_{x,far,avg}(Z) = \frac{\epsilon_r \mu_o k_o^2 I_o}{2} \sum_{m=1}^N D_{xm} \left[ \frac{(m-1)aZ}{\sqrt{Z^2 + (m-1)^2 a^2}} - \frac{maZ}{\sqrt{Z^2 + m^2 a^2}} \right]$$

$$and \ B_{z,far,avg}(Z) = \frac{\mu_o \epsilon_r k_o^2 I_o}{2} \sum_{m=1}^N D_{zm} \left\{ \ln \left[ \frac{ma + \sqrt{Z^2 + m^2 a^2}}{(m-1)a + \sqrt{Z^2 + (m-1)^2 a^2}} \right] \right.$$

$$\left. - \frac{ma}{\sqrt{Z^2 + m^2 a^2}} + \frac{(m-1)a}{\sqrt{Z^2 + (m-1)^2 a^2}} \right\}$$

These results of far-field waveguide analysis can be simply added to the average B-field of near- and mid-field components derived in Appendix B to compute the total flux density as proposed and proved in [56]:

$$|B_{total,avg}(Z)|^2 = [B_{z,far}(Z) + B_{z,near,avg}(Z)]^2$$

$$+ [B_{x,far}(Z) + B_{x,near,avg}(Z)]^2 \quad (3.10)$$

$$+ |B_{r,mid,avg}(Z)|^2 + |B_{\theta,mid,avg}(Z)|^2$$

$$(where \ B_{x,near,avg}(Z) = \frac{\mu_o I_o}{2} \left( \frac{1}{Z^2} - \frac{Z}{\sqrt{Z^2 + a^2}^3} \right),$$

$$B_{z,near,avg}(Z) = \frac{\mu_o I_o a \sqrt{2Z^2 + a^2}}{2Z^2 \sqrt{Z^2 + a^2}^3},$$

$$B_{r,mid,avg}(Z) = j \sqrt{\epsilon_r} \frac{\mu_o k_o I_o a}{Z \sqrt{Z^2 + a^2}},$$

$$and \ B_{\theta,mid,avg}(Z) = j \sqrt{\epsilon_r} \frac{\mu_o k_o I_o}{2} \left( \frac{1}{Z} - \frac{1}{\sqrt{Z^2 + a^2}} \right)$$

Although this mathematically-derived wave propagating model is based on a cylindrical limb which has no realistic curvature and no closed end, it is sufficient to help explain how magnetic coupling can have longer coverage along human limbs than over the air.

### 3.1.3 mHBC Wireless Channel Link

The above analysis showed how to compute magnetic flux density (B) across an mHBC system. To estimate path loss of a wireless mHBC channel, it is necessary to compute the ratio of received power to available power at the source based on computed magnetic flux density. An mHBC system can be mapped to a magnetically-coupled circuit model as shown in Fig.3.6, which can be used to compute the maximum available gain (MAG) as follows:

$$\begin{aligned}
 MAG(z) &= \frac{P_{load,max}(z)}{P_{source,available}} = \frac{\omega^2 M(z)^2 / [8R_2(R_s + R_1 + \frac{\omega^2 M(z)^2}{2R_2})^2]}{V_s^2 (R_1 + \frac{\omega^2 M(z)^2}{2R_2}) / [2R_2(R_s + R_1 + \frac{\omega^2 M(z)^2}{2R_2})^2]} \\
 &= \frac{\omega^2 M(z)^2}{4R_1 R_2 (1 + \frac{\omega^2 M(z)^2}{2R_1 R_2})} \quad (3.11)
 \end{aligned}$$

The mutual inductance, M, largely determines the path loss and is defined as how much the magnetic field flux generated by the current of the primary coil flows through the inner dimension of the secondary coil, and can be computed by:

$$M(z) = \frac{\Phi_{21}(z)}{I_1} = \frac{1}{I_1} \int_{A_2} B_1(z) dA = \frac{A_2}{I_1} B_{total,avg}(z) \quad (3.12)$$

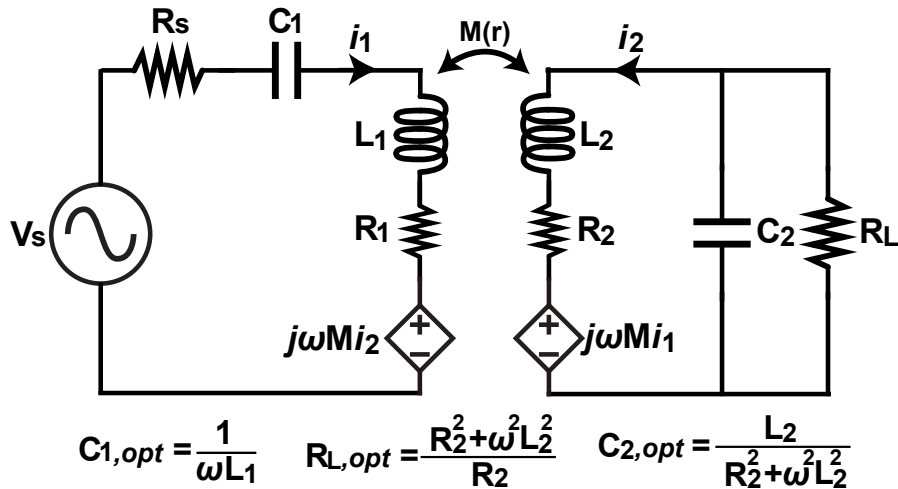


**Figure 3.6:** The simplified circuit model of magnetic resonance coupling for maximum power gain estimation

### 3.1.4 Health Safety of mHBC

Computing the magnetic flux density also enables estimation of the power dissipated in human tissue to determine if it complies with tissue heating safety standards. To estimate the power dissipated in tissue, imagine a coil of conductive tissue located inside the cylindrical limb model as depicted in Fig.3.7a, which can be a path for eddy currents induced by the TX coil. The resistance of this modeled coil can be estimated as:

$$R_{coil\ in\ tissue}(a_{eddy}) = \frac{2\pi a_{eddy}}{\sigma da dz} \quad (3.13)$$

With the resistance of this modeled coil, the eddy current and its power density can be derived as:

$$\begin{aligned} |I_{eddy}(a_{eddy}, z)| &= \left| \frac{j\omega\Phi(z)}{R_{coil\ in\ tissue}} \right| = \frac{\omega\pi a_{eddy}^2 B_{total,avg}(z)}{R_{coil\ in\ tissue}} \\ &= \frac{1}{2}\omega\sigma a_{eddy} B_{total,avg}(z) da dz \\ P_{eddy}(a_{eddy}, z) &= \frac{1}{2}|I_{eddy}|^2 R_{coil\ in\ tissue} = \frac{1}{4}\omega^2\sigma\pi a_{eddy}^3 da dz [B_{total,avg}(z)]^2 \\ p_{v,eddy}(a_{eddy}, z) &= \frac{P_{eddy}(a_{eddy}, z)}{2\pi a_{eddy} da dz} = \frac{1}{8}\omega^2\sigma a_{eddy}^2 [B_{total,avg}(z)]^2 \end{aligned} \quad (3.14)$$

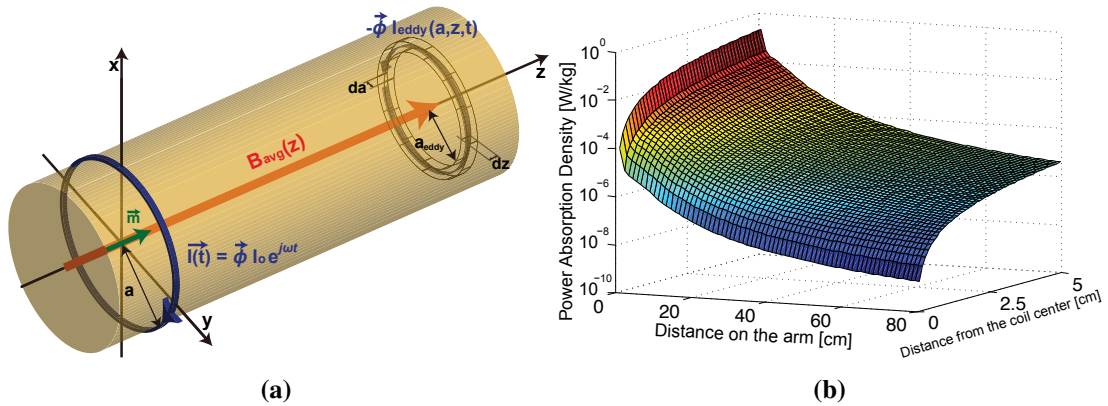


**Figure 3.7:** (a) the power absorption estimating model by a coil of the conductive tissue and (b) its result.

Fig.3.7b shows the local power absorption density induced by 0 dBm mHBC transmitter coil. Here, power density ( $\text{W}/\text{cm}^3$ ) is represented in units of  $\text{W}/\text{kg}$  assuming an averaged tissue mass density ( $1.1 \times 10^{-3} \text{ kg}/\text{cm}^3$ ) in order to compare to the averaged specific absorption rate (SAR) regulation ( $1.6 \text{ W}/\text{kg}$ ) which is commonly used as the restriction for transmitting power of wireless communication systems [57]. Here, the peak local power density of  $0.23 \text{ W}/\text{kg}$  from the 0 dBm transmitter is well under SAR limits. Since in practice the required TX power is actually much lower than 0 dBm and the averaged SAR should have a lower value by averaging in volume, practical mHBC systems should be well under SAR limits.

## 3.2 Results

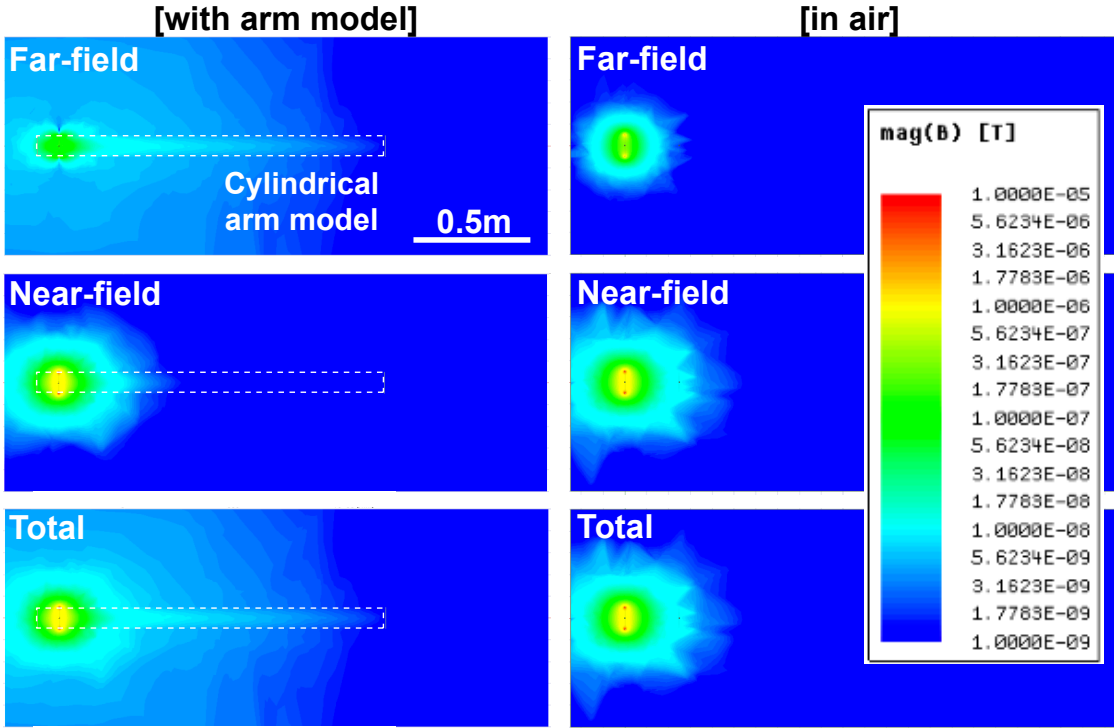
### 3.2.1 Validation of Analysis with FEM simulations

Figure 3.8 shows the simulated B-field pattern with and without 1.4-m cylindrical arm model, respectively, illustrating that far-field components tend to be more concentrated along the cylinder due to the tissue-air boundary, while near-field components remain the same regardless of the presence of tissue, as expected. Figure 3.9a contrasts simulated B-field magnitude averaged in the cross-section of the limb model to results from the developed far-field and near-field model in Eqns. (3.9) and (3.10). The full-field EM simulation analysis matches well with the developed model until near the end of the cylinder (which has a finite length in simulation but an infinite length in the analytical model), while also showing the off-body fall-off of magnetic flux. The far-field component of the B-field, which has slow attenuation ( $1/r$ ), dominates the near-field beyond the near-field region boundary, which recall was shrunk to 0.25 m inside the body (at 21 MHz with  $\epsilon_r=80$ ), in Fig. 3.9a, while providing better communication coverage than over-the-air quasi-static near-field which has fast attenuation ( $1/r^3$ ) within a 2-m body area as depicted in Fig. 3.9b. The enhanced far-field inside the body results in the better B-field propagation ( $\sim 10\times$  higher in simulation and  $\sim 30\times$  higher

in analysis at the edge of the body model in Fig. 3.10a), which improves the channel gain described in Eqn. (3.11). With the impedance properties of the designed mHBC coils and the averaged B-field results from analysis and simulation models, the channel gain (MAG) can be estimated and be compared to the measured MAG as shown in Fig. 3.10b. The developed model predicts path loss with  $<1.8$  dB error for distances  $> 1$  m. At lower distances, the coils become strongly coupled [41] and the analytical model underestimates path loss.

### 3.2.2 Measurement Results

To validate the developed physics and demonstrate the benefits of mHBC over other wireless body-area networking approaches, prototype coils were developed to wrap around the wrist (e.g., like a smartwatch) or head (e.g., like a headband or hat) and used to perform channel measurements and deliver sensor information across the



**Figure 3.8:** The 3D FEM simulated B-field pattern of far-field, near-field, and total field with the cylindrical human limb model and in air

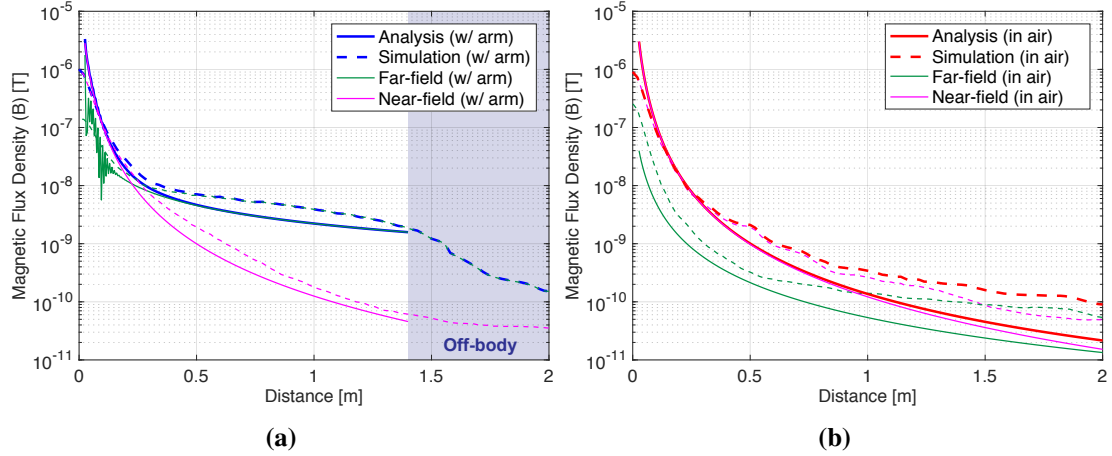


**Figure 3.9:** (a) the analysis and simulation results of B-field magnitude averaged within the cross section of the limb model and (b) within the same dimension in air,

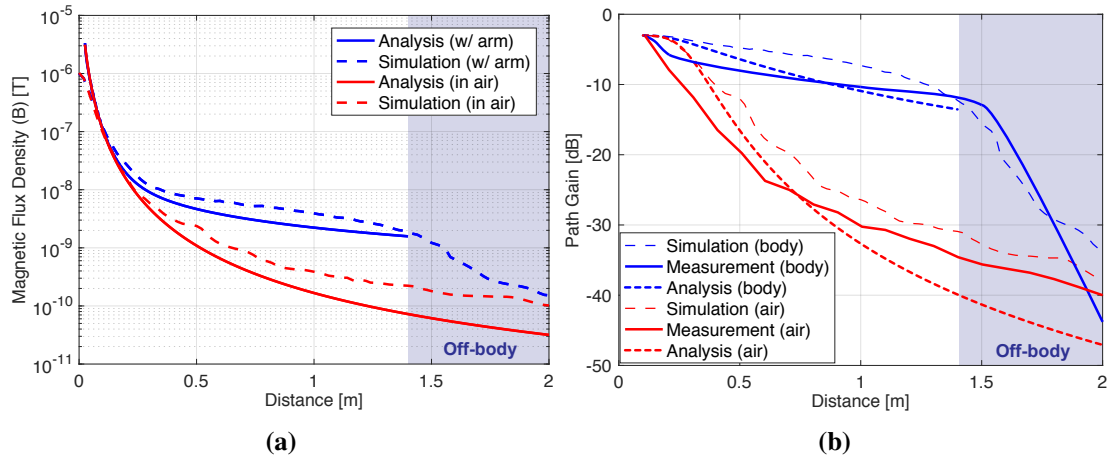


**Figure 3.10:** (a) the total averaged B-field magnitude comparison between with body and in air and (b) the estimated path gain from analysis and simulation and its comparison to the measured path gain.

body. Figure 3.11a shows measured path loss across the human body when a coil is placed on a stationary wrist, while another coil is moving along outstretched arms to increase the distance between the coils. These results are contrasted with the developed mHBC model along with other communication approaches.

Here, mHBC achieves a path loss less than 13.1 dB across the body, which is 25 dB better than prior-art eHBC techniques [15], and >70 dB better than a 2.4 GHz Bluetooth RF measured with a ceramic chip planar inverted-F antenna (Yageo

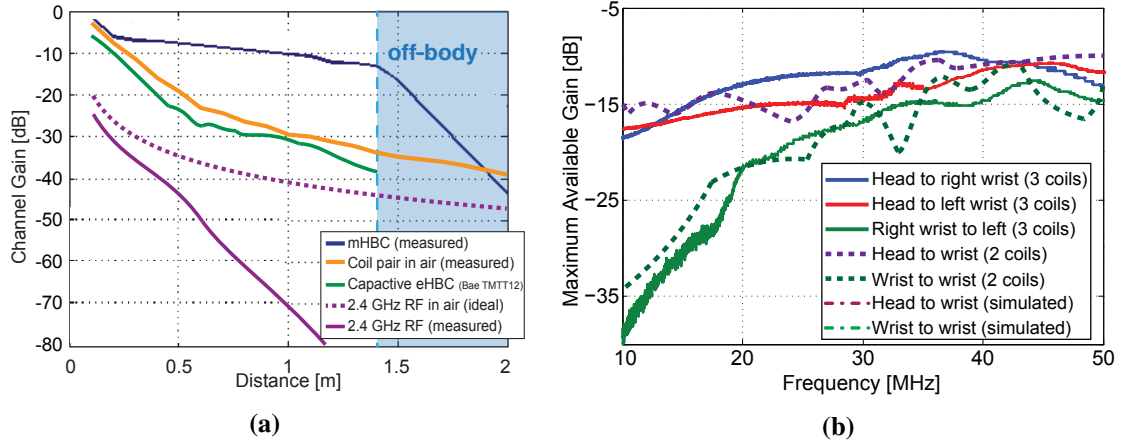


**Figure 3.11:** Experiment results: (a) path loss vs. distance (wrist to wrist) compared to conventional techniques and (b) Path loss of three coherent coils in a single mHBC system compared to a two-coil system

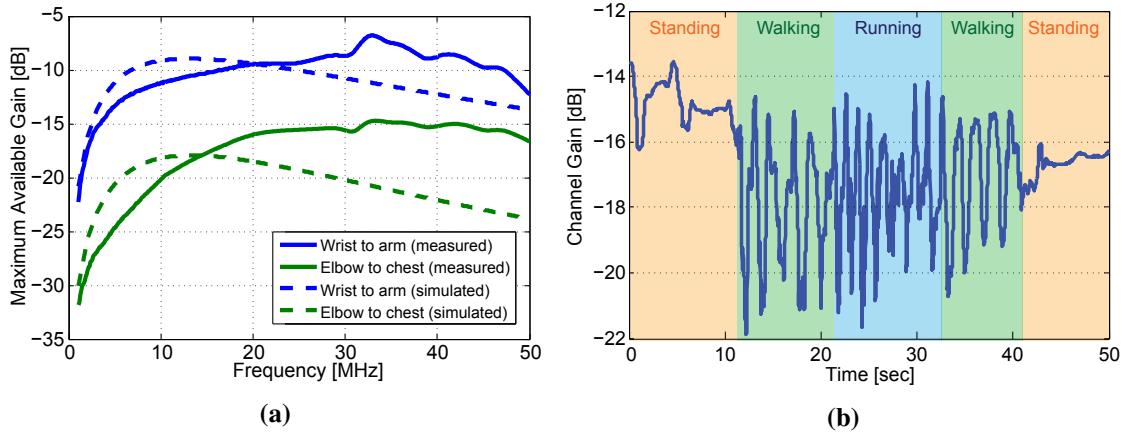


**Figure 3.12:** Additional results: (a) path loss across 40 cm between two wrap-around coils (wrist-to-arm) or between a planar chest-worn patch and a wrap-around coil on an arm and (b) Path loss fluctuation during motion (wrist-to-head)

ANT5320LL24R2455A) over a  $30 \times 30 \text{ mm}^2$  ground plane of 1 oz 2-layer copper PCB mimicking the form factor of wearable devices such as a smartwatch. Importantly, measurements results performed using the same setup as mHBC, but in this case without the human body present (i.e., measurements performed in air), reveal path loss degradation of up to 30 dB compared to including the body in the channel, which helps validate the enhanced far-field component and leaky dielectric waveguiding effect of the human body.

To demonstrate that multiple coils can be used within a single body-area network in both wrap-around and planar coil geometries, Figs. 3.11b and 3.12a show measurement results of two- and three-coil systems communicating between the head and one or two wrist (3.11b) or between the wrist and a chest-worn patch (3.12a), demonstrating  $<15$  dB path loss at optimal frequencies in all cases. Note that the two-coil system measurement results are from [30]. Motion of the human body, which adversely affects conventional wireless channels via significant path loss variation (e.g., path loss down to 90 dB [58], is shown in Fig.3.12b to fluctuate path loss by up to 7.8 dB, which can be easily managed by high-efficiency, low-complexity receiver circuitry.

### 3.2.3 System Demonstration

To demonstrate that mHBC can be used in realistic scenarios, a wearable EEG data acquisition system was developed to measure brain activity and deliver sensed information from the head to a wrist-worn RX device (Fig. 3.15). Figure 3.13a shows that measured symbol-error-rate (SER) curves achieve reliable performance at data rates up to 656.25 kbps at transmit powers below -33 dBm for -65 dBm RX sensitivity (in contrast, most Bluetooth radios utilize  $>0$  dBm transmit power and  $<-95$  dBm RX sensitiv-

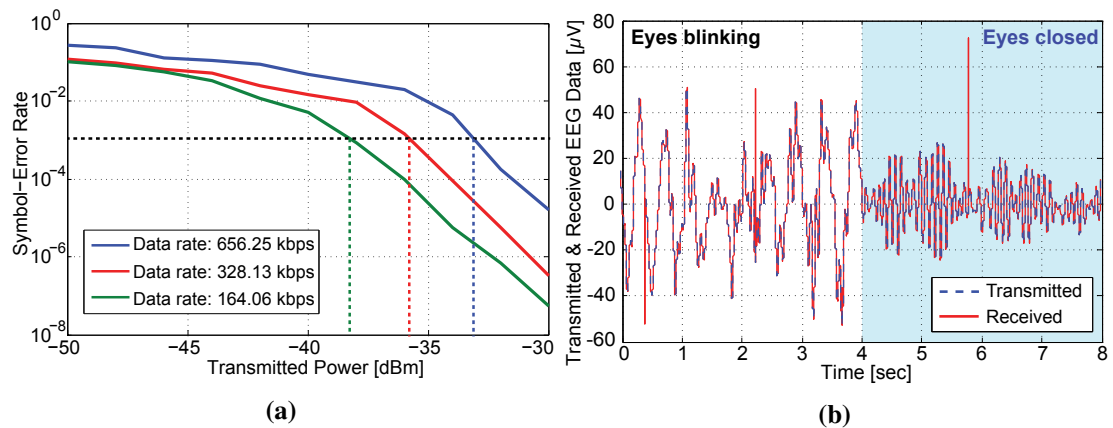


**Figure 3.13:** Demonstration results: (a) symbol-error rate curves at various data rates and (b) Comparison between the acquired EEG data in the TX unit and the demodulation result of received data on the RX side with -35 dBm transmit power.

ity for BAN), thereby demonstrating a  $2,000\times$  reduction in transmit power with lower RX complexity for high sensitivity compared to the CC2642R module. Measurement results of captured EEG data before and after mHBC transmission across the body in Fig. 3.13b reveal that the developed mHBC system can reliably transmit sensed information across the body with  $<10^{-5}$  SER, demonstrating that mHBC is a practical technique to achieve reliable communication around the body. The dramatic reduction in transmit power and RX sensitivity can improve battery life of a wearable system incorporating a 20 mWh Li-ion battery from 20 hours to  $>40,000$  hours, enabling more convenient, long-term operation of wearable devices for improved monitoring and diagnostics.

## **3.3 Methods and Material**

### **3.3.1 Simulation Methods**

All 3D finite-element-method (FEM) simulations are performed in Ansys HFSS to validate the channel performance of the proposed mHBC concept using realistic body surface meshes. To this end, two 3D meshes obtained by scanning the geometry of two separate postures of a standing male subject with a WB4 laser are utilized. Mesh data was provided by NEVA Electromagnetics Inc. [26], and the resulting model is shown in Fig. S1A. Although this silhouette model excludes internal organs and features, the model is sufficient to characterize the field behavior at the tissue-air boundary.

In addition to physical geometry, the dielectric properties of biological tissue must be also considered for realistic simulation results. Since the dielectric properties of tissue depend on the operating frequency as reported in [27], the FEM model should incorporate the relative permittivity and conductivity with frequency-dependencies as depicted in Figs. 3.14b and 3.14c. However, since the employed 3D body model is a single uniform piece without layers such as skin, organs, and bones, the dielectric properties, which are on average similar to one another compared to air, are instead averaged across the body, weighted by their respective volumes, and assigned to the

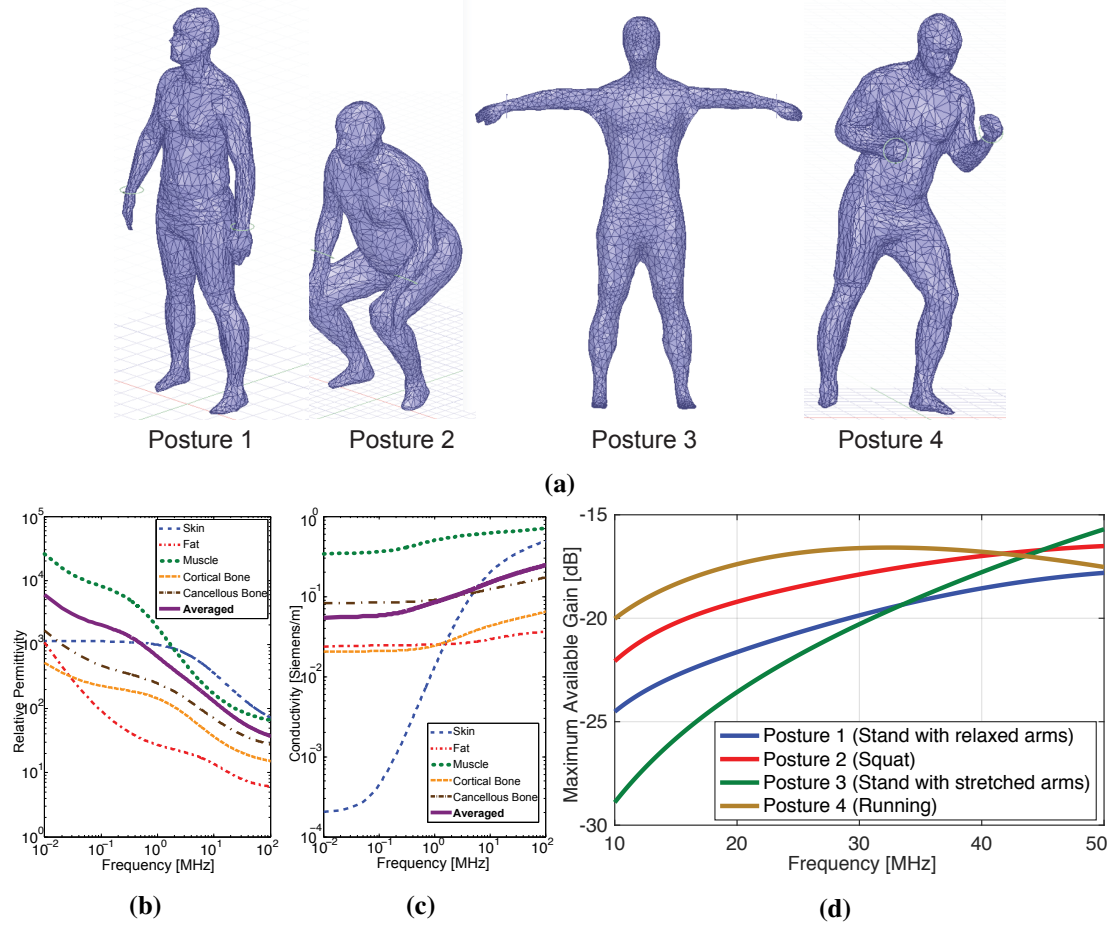


**Figure 3.14:** Practical human body model and its simulation results: (a) body surface meshes for HFSS, dielectric properties of human tissues: (b) relative permittivity and (c) conductivity, and (d) path loss simulation results.

lumped body model. Thus, Fig. S1B shows not only the dielectric properties of several important tissue types but also their weighted average. Here, Fig. 3.14d depicts the simulation results of the various postures shown in Fig. 3.14a, while validating the measured path loss fluctuation (up to 7.8dB at 21 MHz) by natural human body motion shown in Fig. 3.12b. The cylindrical model, employed to validate the proposed analytic model in Fig. 3.8, used a 1.4-m length and 10-cm diameter single bulk cylinder assigned as the material with  $\epsilon_r = 80$  and  $\sigma = 0.2$  Siemens/m at 21 MHz. The 10-cm diameter coil was implemented with 2.6-mm diameter copper wires with appropriate shunt tuning capacitance for resonance at 21 MHz.

Magnetic fields are generated and received in FEM simulations using circular copper coils. For coil placement around arms and legs, 10 cm diameter coils with 2.6 mm diameter copper wires were implemented. For coil placement around the head, 18 cm diameter coils were employed. To resonate at the HFSS solution frequency (nominally set to be 21 MHz), the designed coils were shunted with capacitors tuned for 21 MHz resonance after initial simulations revealed coil inductance. Also, to ensure the accuracy of results from HFSS simulations, a Delta- $S$  of 0.01 was used for the convergence value of  $S$ -parameters, resulting in greater than 700,000 meshes. The simulations applied a mixed order of basis functions to address both near-field and far-field radiation.

### 3.3.2 Measurement Materials and Methods

In order to validate the performance of mHBC systems as predicted from the developed analytical model and simulation results, path loss was measured with a vector network analyzer (VNA). Unlike eHBC systems, which cannot employ large benchtop instruments due to the parasitic return path by the internal ground plates of instruments [42], magnetic coupling operates without needing reference potentials, and thus path loss through mHBC links can be measured directly by a benchtop VNA [30]. In this work, a Keysight E5071C VNA (Santa Rosa, CA), was employed. The coils were implemented with enameled copper wires with PVC tube insulation to minimize the electric body coupling, and sized to be the same as in the FEM simulations.

Again in contrast to eHBC schemes, which have difficult matching electrode capacitance due to severe environmental/posture variation and the requirement of large (e.g.,  $>1$  mH) inductors, mHBC coils can be easily matched via small (e.g., pF) ceramic capacitors, and this matching is robust to environmental and posture variation. Since matching is easily achieved, rather than designing matching networks at each individual frequency tested, path loss can instead be measured via maximum available gain (MAG), which is the best achievable path loss assuming the TX and RX are conjugate-matched, via measurement of  $S$ -parameters and the following equation:

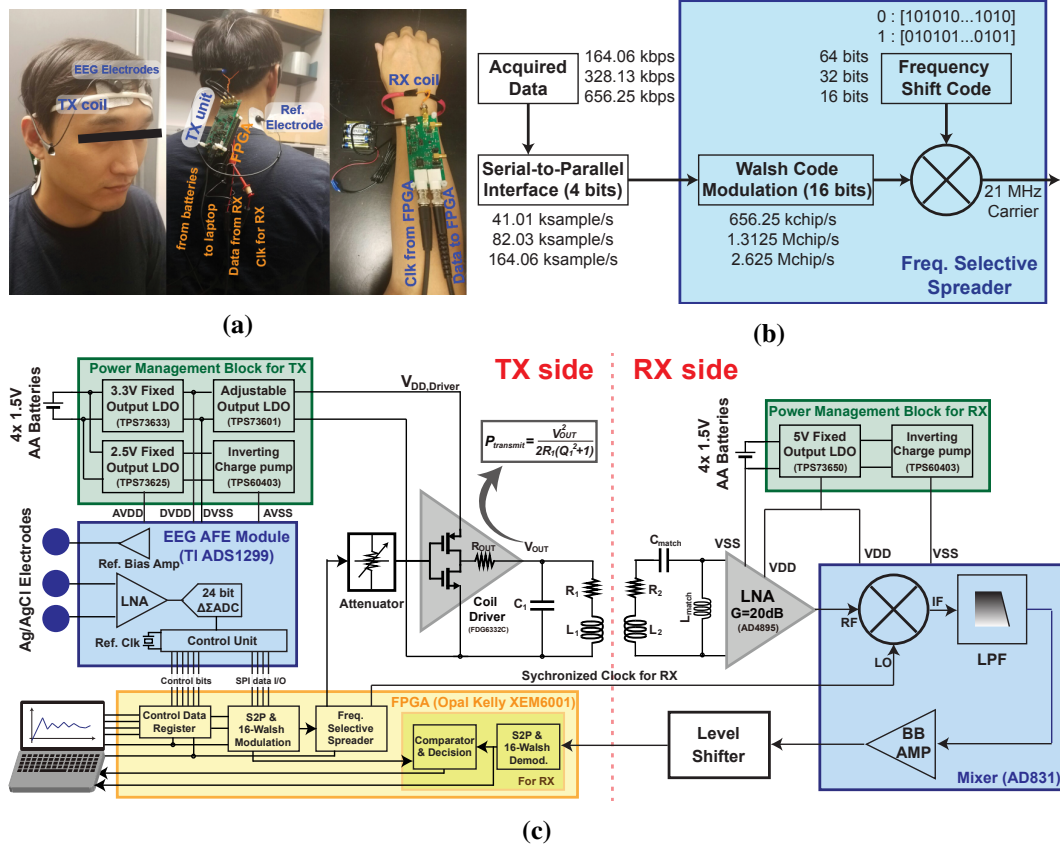


**Figure 3.15:** EEG demonstration: (a) the EEG data transfer prototype, (b) the block diagram of frequency selective digital transmission (FSDT) modulation, and (c) a hardware configuration for the EEG data transfer system.

In this work, S-parameters were measured ten times in three different instances, and the results averaged before computing MAG. To validate that measurement of MAG was satisfactory in determining path loss, a 21 MHz resonator was constructed, and MAG and  $S_{21}$  measurements matched within 1.75 dB. Measurement of EEG transmission from the head to the wrist via mHBC required the development of a full transceiver system. A photograph of the developed system is shown in 3.15a. The transceiver system was engineered to be compatible with the IEEE 802.15.6 [59] employed for eHBC, which uses frequency selective digital transmission (FSDT) for data modulation. As shown in Fig. 3.15b, the FSDT scheme utilizes a frequency selective spreader to directly generate a 21 MHz carrier transmitting data signal with a 16-bit Walsh code. A block diagram of the hardware prototype is shown in Fig. 3.15c.

The mHBC TX unit, placed on the head, performed EEG acquisition with a Texas Instruments ADS1299 analog front-end (AFE) module (Dallas, TX) that employs programmable gain low noise amplifiers, 24-bit  $\Delta\Sigma$  analog-to-digital converters, and an internal reference bias driver. The TX was controlled by an Opal Kelly (Portland, OR) XEM6001 field-programmable gate array (FPGA) to control the operation of the EEG AFE module as well as modulate the acquired EEG data via the FSDT scheme as described in Fig. S2B. The 18 cm diameter TX coil (637.2 nH with  $Q$  factor of 27) transmitted the modulated FPGA output via a driver comprised of N & P-channel power MOSFETs (Fairchild Semiconductor FDG6332C). The output power was set with an adjustable VDD, Driver from a low-dropout regulator (Texas Instrument TPS73601). To constrain the transmitting power from the TX coil to below -30 dBm, a resistive attenuator was placed between the 3.3 V FPGA output and the power driver. To mimic the operation of battery-power wearable products, the developed prototype included a power management block incorporating LDOs (Texas Instrument TPS73633 and TPS73625) and an inverting charge pump (Texas Instrument TPS60403).

The mHBC RX unit connected to a 10 cm diameter RX coil on the wrist and demodulated received data after a 20-dB gain LNA (Analog Devices AD4895) and a 0-dB conversion gain mixer (Analog Devices AD831). An impedance matching network was designed for the interface between the RX coil (300.1 nH with 95.23  $Q$  factor) and the 50  $\Omega$  input of the LNA at 21MHz. To simplify synchronization between transmitting and receiving nodes, the FPGA provided the reference clock for down-conversion operation in the mixer. Level shifters were employed at the interface between the FPGA and the output of the mixer. Finally, the FPGA performed the Walsh demodulation.

## 3.4 Conclusion

This paper has presented an energy-efficient way to improve the limited coverage of inductive-coupling-based near-field communication by employing the human body as a leaky dielectric waveguide for far-field radiation. Analytical modeling, 3D

FEM simulations, and experimental evidence suggest that at distances larger than approximately 25cm, the far-field component indeed dominates inside the human body, in part due to the high permittivity of human tissue ( $\epsilon_r > 80$ ) that enhances the far field radiation and shortens the wavelength, while offering a more favorable  $1/r^2$  attenuation compared to the  $1/r^6$  attenuation of near-field components. Since the human body is on the same order of size as the wavelength in tissue (e.g., 1.6 m at 21 MHz), conventional leaky dielectric waveguide analysis, which requires an assumption of a uniform plane wave (i.e., a waveguide that is at least multiple wavelengths long), is not appropriate for analysis, and thus the proposed ray-tracing-like analytical method is proposed.

The developed theoretical analysis, 3D FEM simulations, and measurements of mHBC systems in representative scenarios all agree that mHBC offers a multi-order-of-magnitude path loss improvement over other forms of wireless communication around the human body. Additionally, measurement results revealed relatively constant path loss variation during natural human motion. Low path loss and low variation will help enable the design of low-complexity, low-power integrated transceiver circuits in future work to ultimately enable wireless body-area connectivity at much lower power than current solutions provide. This will help facilitate further improvements in size and/or battery life of wearable devices for applications ranging from sports, fitness, medicine, personal entertainment, and beyond.

Chapter Three is largely a combination of material as it is submitted to Proceedings of the National Academy of Sciences of the United States of America (PNAS): "Energy-Efficient Intra-Body Wireless Communication via a Human Body Dielectric Waveguide" and as it appears in "Magnetic Human Body Communication," in Annual International Conference of the IEEE Engineering in Medicine and Biology Society (EMBC), August 2015, which both are written by Jiwoong Park and Patrick P. Mercier. The dissertation author is the primary investigator and author of this work.

## **Chapter 4**

# **A Sub-10 pJ/bit 5 Mbps Magnetic Human Body Communication Transceiver Demonstrating High-Fidelity Audio Trans-Body Delivery**

Advances in wearable devices such as wireless headphones, head-mount displays, and medical monitoring sensors have offered exciting opportunities to improve lifestyle in terms of both entertainment and health. Nearly all such wearable devices require wireless communication functionality, either directly to cellular or WiFi access points, or via a local body area network (BAN) which then connects to commodity wireless equipment via a single node (e.g., a smartphone or smartwatch). Since wearable devices must be sufficiently small to comfortably fit within human anatomy, and since radios often dominate the power consumption of such devices [38], ultra-low-power BANs are typically preferred over direct communication to distal access points.

The most popular BAN approach today is Bluetooth Low Energy (BLE). However, this 2.4 GHz RF standard was originally designed for free-space communication at a distance of  $>10$  m, rather than for a short-range BAN: the broadcasting nature of 2.4 GHz RF results in severe loss across the human body, which absorbs RF energy quite well at 2.4 GHz, thereby significantly increasing path loss over free space scenarios [1, 60], as illustrated in Fig. 4.1a. As a result, BLE transceivers must support large

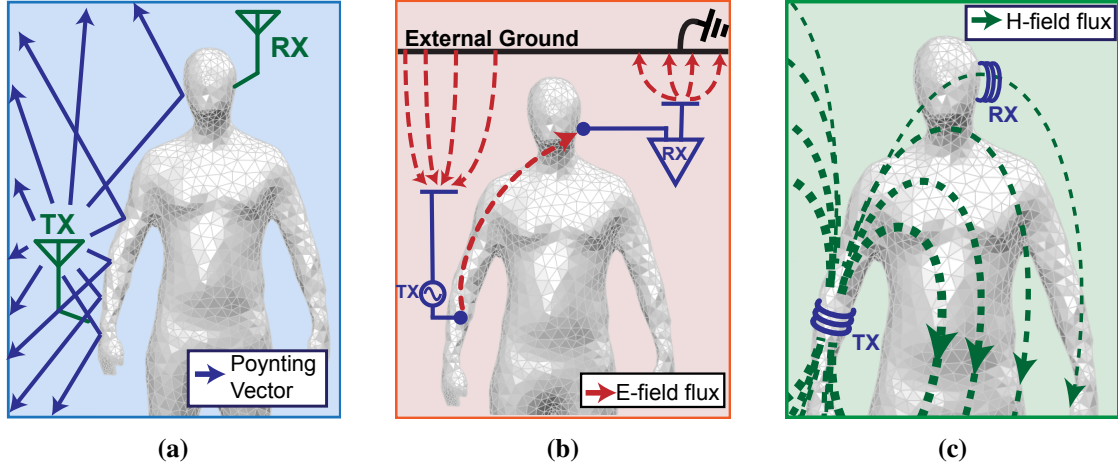


**Figure 4.1:** (a) Conventional RF broadcasting (e.g. Bluetooth). (b) Capacitively-coupled eHBC. (c) mHBC.

amounts of power-expensive amplification (e.g.,  $\sim$ mW-scale for 1 Mbps data transfer), causing BLE to dominate the power of wearable devices, to the point that small devices such as wireless earbuds have battery lives of only a few hours.

Instead of broadcasting RF energy, researchers have proposed using the human body itself as a conduit for lower-frequency quasi-static fields, as illustrated in 4.1b, which theoretically supports lower path loss [61]. Since then, many electric-field-based human body communication (eHBC) transceivers have been demonstrated [62–70]. In general, these transceivers have demonstrated improved energy-efficiency over conventional RF approaches due to improved path loss. However, as will be described in Section II, path loss measurements were not necessarily done correctly in most cases, with actual losses higher, which will result in reduced energy efficiency in practice. In addition, capacitive coupling to the body and the environment can change substantially with posture and normal movement, which requires bulky dynamically-tunable inductors [71] that are difficult to efficiently implement over a wide range of conditions.

To further reduce path loss and improve the ability to dynamically tune for varying posture and environmental conditions, we have previously proposed magnetic human body communication (mHBC) [30], illustrated in Fig. 4.1c. In mHBC, path loss has been measured to be as low as 10-20 dB across a  $\sim$ 1 m human body, which compares

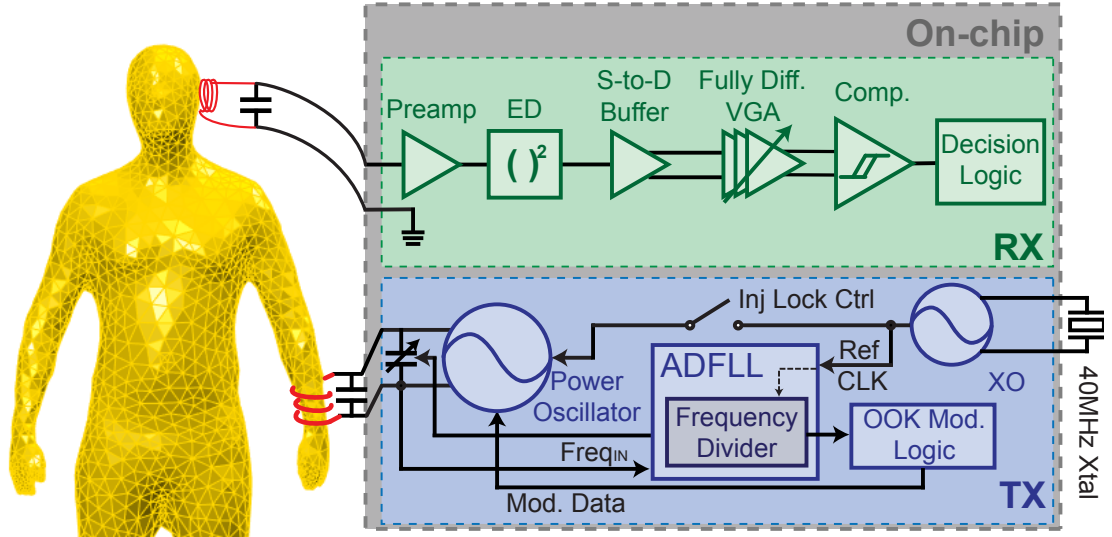


**Figure 4.2:** System block diagram of the proposed mHBC transceiver.

favorably to  $\sim 80$  dB in RF, or  $\sim 40$  dB in eHBC. Theoretically, a lower path loss enables the design of transceivers that require less amplification and less complexity, resulting in reduced power consumption towards a longer battery life for wearable devices.

This chapter start by briefly describing the mHBC technique in general and contrasting to other BAN approaches in Section 4.1. In Sections 4.2 and 4.3, we discuss how to design a low-power mHBC transmitter (TX) and receiver (RX), respectively, that can each operate at high instantaneous data rates to support high energy efficiency. Section 4.4 then reports the performance and specifications of the implemented mHBC transceiver. Finally, Section 4.5 verifies that the proposed mHBC transceiver depicted in Fig. 4.2 works in a practical scenario via the demonstration of 5 Mbps high-fidelity (Hi-Fi) audio data transfer between phone-mounted and ear-mounted prototypes.

## 4.1 Wireless Body Area Network Approaches

### 4.1.1 Sub-6 GHz Radio Frequency

The most traditional way to communicate across the body involves propagating RF waves operating in one of the main Industrial, Scientific, and Medical (ISM)

bands between 400 MHz and 5 GHz. Due to the relatively high conductivity of biological tissues at frequencies in the high-MHz range and beyond, the human body ends up blocking a large fraction of broadcast power from a body-worn antenna, as loosely illustrated in Fig. 4.1a. For example, the body shadowing effect increases the 1.5 m channel loss of a 2.4 GHz Bluetooth communication link from 40 dB to upwards of 85 dB [1], as summarized for various BAN-relevant distances in Fig. 4.3. Another study reported that a 17-cm-long ear-to-ear communication link has 98.2 dB channel loss due to high insertion loss around the brain [60]. Such severe path loss degradation requires higher power communication circuits to achieve higher TX output power as well as better sensitivity and wider dynamic range for RXs. Furthermore, due to the broadcasting nature of sub-6 GHz RF communications, all such systems must support elaborate medium access control techniques to support multi-user access in congested environments, while

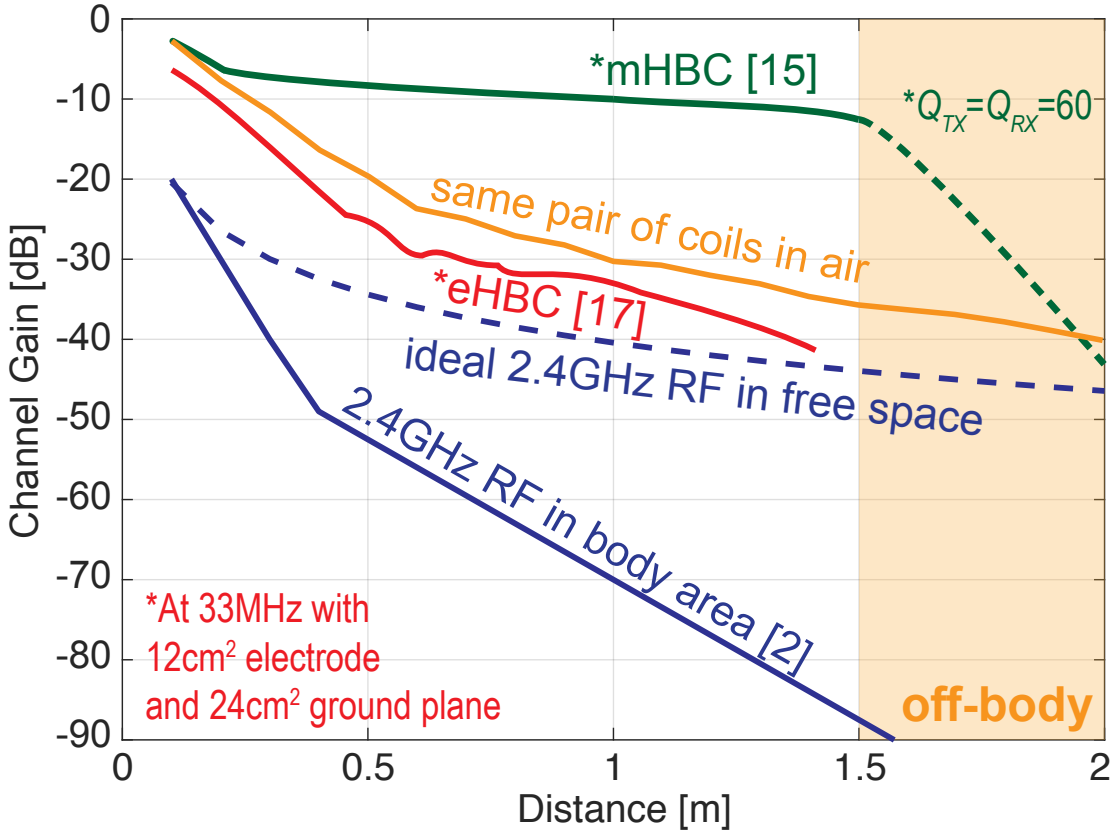


**Figure 4.3:** Channel gain comparison of mHBC to previous wireless BAN approaches.

also providing careful encryption services to data privacy and security, both of which may require even more power consumption. For this reason, researchers have explored other BAN techniques in an attempt to reduce power.

### **4.1.2 Electric Human Body Communication**

In 1995, researchers proposed to use the human body as a conduit of quasi-static electric fields [3]. While there are multiple ways to accomplish this, the most popular to date relies on capacitive coupling. Capacitive eHBC specifically attempts to improve channel gain by employing the human body as a forward signal path while utilizing the naturally-occurring capacitive coupling with the environment as a return path as illustrated in Fig. 4.1b. Many early studies showed that path loss in capacitive eHBC systems could be quite good: for example down 40 dB across the body [15]. However, most such studies did not perform path loss measurements correctly: the presence of large ground planes of measurement and test equipment inadvertently resulted in high-quality capacitive return paths that caused artificially better path loss. In general, the only way to accurately measure eHBC path loss is via battery-powered form-factor-accurate devices [42]. When done in this manner, measurement results reveal worse path loss than previously estimated (e.g., 32 dB over 20 cm at 72 MHz in [42], or 49 dB over 25 cm at  $<1$  MHz in [72]), though still with arguably advantageous performance over far-field RF approaches in a BAN. Figure 4.3 summarizes the path loss results in [15], though it should be noted that due to the large employed electrode and ground planes enable better path loss than a smaller form-factor-accurate prototype would.

Capacitive eHBC approaches also have favorable multi-user access and security/privacy benefits, since the signals are much more localized to the human body than broadcasting RF. Unfortunately, as a result, capacitive eHBC approaches are also very sensitive to environmental and postural variation. As a capacitive interface, these approaches require a variable inductive matching network, if narrowband tuning and passive voltage gain are desired for maximum sensitivity, which can be difficult to imple-

ment efficiently and reliably over a wide range of conditions [42, 64, 71]. Alternatively, wideband high-impedance termination can be used, which eases variation requirements at the expense of the absence of passive voltage gain [72].

Thus, while there is still promise and potential for eHBC-based BANs, challenges remain. The next subsection will show that mHBC offers additional significant advantages that make it an arguably even more attractive approach.

### 4.1.3 Magnetic Human Body Communication

Part of the challenge of capacitive eHBC systems is the differential nature of voltage measurements: they require both a sensing and a reference electrode. In capacitive eHBC systems, this configuration means that both the forward and return paths, which are both highly variable, together determine the path loss. In addition, while the human body is conductive, it is not exactly an excellent conductor, which reduces the forward path gain.

The idea for mHBC came from two ideas: the human body is magnetically inert ( $\mu_r \approx 1$ ), and magnetic fields can be sensed in a single-ended manner (i.e., without requiring a reference point), easing implementation requirements and reducing the impact of environmental variation. With  $\mu_r \approx 1$  the thought was that magnetic fields should exist within the body just as they would do in air. If mHBC were to operate only in the near field, this conclusion would be correct.

To our surprise, however, the path loss between two coils in both simulations and measurements was actually better with the body in the way at 10s of MHz than when operating in air [30]. Measurement results in air and on the body are summarized in both [30] and Fig. 4.3. On the body, path loss can be as low as 10 dB, which is far better than RF or eHBC approaches. Due to the inherently single-ended nature, environmental variations are low, and any existing variation can be easily handled by simple capacitive tuning (described in Section 4.2). Additionally, magnetic fields fall off rapidly away from the body, providing some of the same multi-user access and privacy/security

benefits of eHBC systems.

While initially surprising, we hypothesize that the improved performance is due to the presence of far-field components that have favorable properties at these frequencies on the body. Specifically, it can be briefly noted that due to the high permittivity of biological tissue ( $\epsilon_r > 80$ ), the near-field region boundary ( $\lambda/2\pi$ ) is reduced to 0.13 m in tissue at 40 MHz due to the enhanced far-field radiation which has slower attenuation ( $1/r^2$ ) than the near-field quasi-static ( $1/r^6$ ). It is also known in the literature that magnetic loop antennas (i.e., coils) show better performance than electric dipole antennas in high dielectric dissipative medium such as seawater, which has similar permittivity but higher conductivity than biological tissue [50, 51]. Thus, it can be noted that the proposed mHBC approach, when operating at 10s of MHz across the body, is distinctly different from conventional near-field magnetic approaches, for example Near Field Communication (NFC), or Near Field Magnetic Induction (NFMI), by utilizing components ranging from the near- to the far-field in a similar manner to recent work on mid-field wireless power transfer [49]. With that being said, the far-field contributions and subsequent advantage is currently only a hypothesis, and the exact physics describing mHBC are still under investigation and will be disseminated in a future publication.

Inclusion of far-field components also offer another advantage: less susceptibility to TX-RX misalignment. Figure 4.4 shows the measured results of maximum available gain (MAG) and the phase shift of an mHBC channel across various different postures, demonstrating reduced path loss variation (i.e.,  $<4$  dB across an mHBC channel). Here, the channel gain measurement was performed with a wristband coil pair ( $Q=60$ ) insulated with thick PVC tube to minimize the effect of capacitive eHBC-like coupling. It can be noted that while path loss experiences very little fluctuation with posture, the phase shift of the mHBC channel does strongly depend on the angle between the two coils. As a result, it is not desirable to employ phase-based modulation schemes in low-power mHBC implementations. Instead, amplitude- or frequency-modulated waveforms are more appropriate. In this work, we employ OOK modulation at 40 MHz.

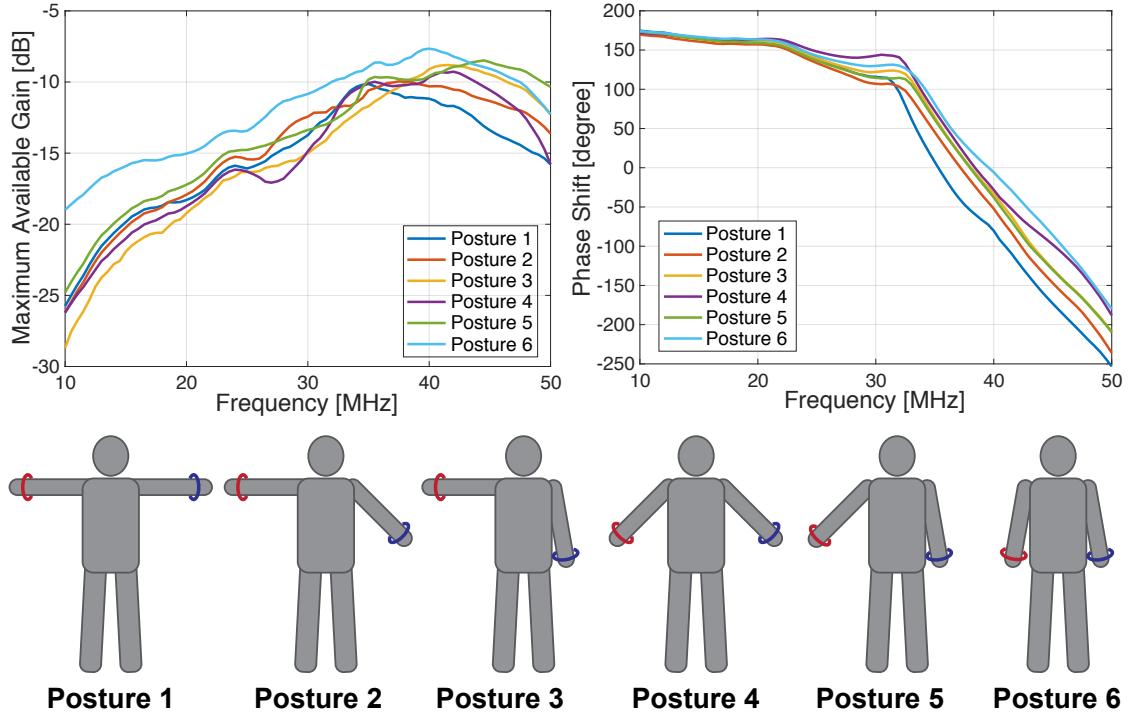


**Figure 4.4:** Measured results of maximum available gain and phase shift of the mHBC channel with various body postures.

Instead of capacitive coupling, magnetic resonance coupling is implemented in wireless BANs to address the shortcomings of E-field-based wireless technologies. Since the H-field energy travels freely through the biological tissues as illustrated in Fig. 4.1c, mHBC exhibits excellent path loss compared to the E-field based approaches, as plotted in Fig. 4.3 [15]. Also, unlike the eHBC system, the mHBC system establishes a wireless communication link without reference potential, thereby minimizing the environmental influence and variations by user’s moving and postures. Interestingly, magnetic energy can be confined inside a human body; therefore, it provides path gain enhancement and rapid off-body path loss attenuation that enable high-secured and energy-efficient data transferring [30].

Due to the extremely good path loss, mHBC offers a significantly relaxed link budget to help reduce required transceiver complexity and power. For example, Fig. 4.5 illustrated a BLE link budget that, due to the additional 44 dB of body shadowing

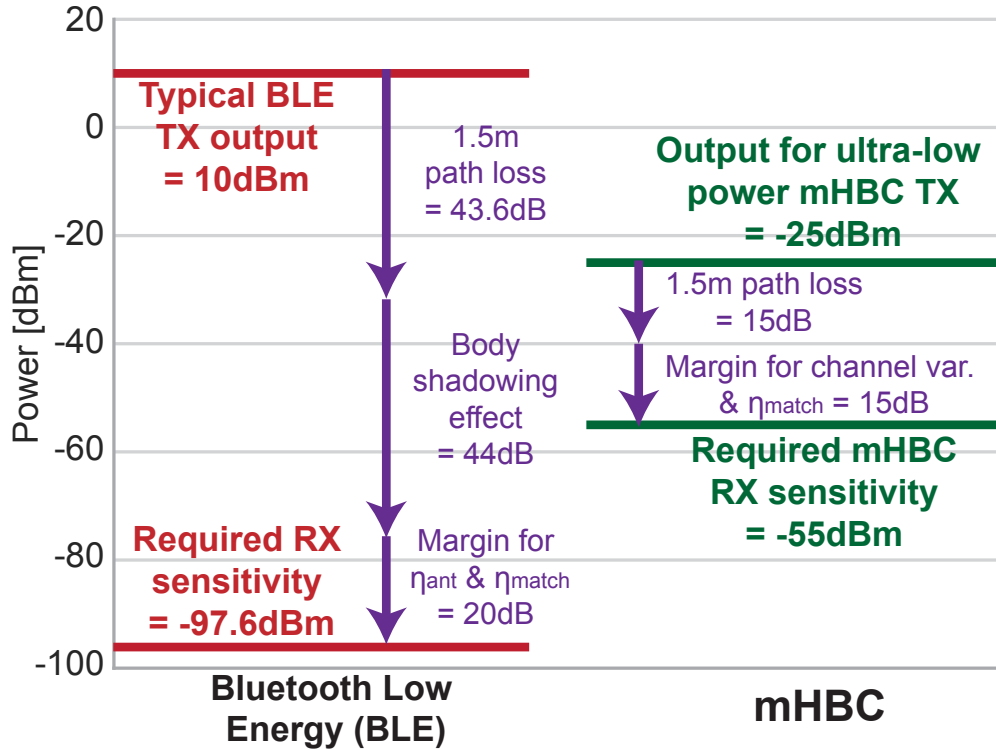


**Figure 4.5:** Comparison of required receiver sensitivity between 2.4 GHz RF Bluetooth Low Energy and mHBC.

effect on top of the 43.6 dB path loss across 1.5 m plus margin for matching efficiencies, antenna gain, and so on, requires an RX sensitivity of -97.6 dBm for a 10 dBm TX output power, which requires mW-level power consumption. In contrast, the low mHBC path loss, plus margin for channel variation and matching, permits significantly reduced TX power and sensitivity. Due to fixed overheads in both transmit and receiver circuits, it does not make sense to push TX power too low, or RX noise figure too high, in order to arrive at an optimally-low transceiver power consumption. For example, a -25 dBm TX output power and an -55 dBm RX sensitivity are reasonable link budget selections to enable energy-efficient operation to cover a 1.5 m body-area link. This link budget enables a dramatic reduction in transceiver power consumption, as will described in the Sections 4.2-4.4.

## 4.2 mHBC Transmitter Implementation

As described in the previous section, the relaxed link budget offered by mHBC affords a very relaxed TX output power specification. Unlike in conventional RF TXs where the output power is so high that the power amplifier largely determines the overall TX efficiency, the power of all downstream components in the TX matters when transmitting such a small amount of power (i.e., -25 dBm is  $3 \mu\text{W}$ ), which motivates a simple, low-complexity TX architecture.

Figure 4.6a depicts a conventional TX architecture used in many low-power RF applications. With such a low output power in mHBC, the power overhead of the syn-

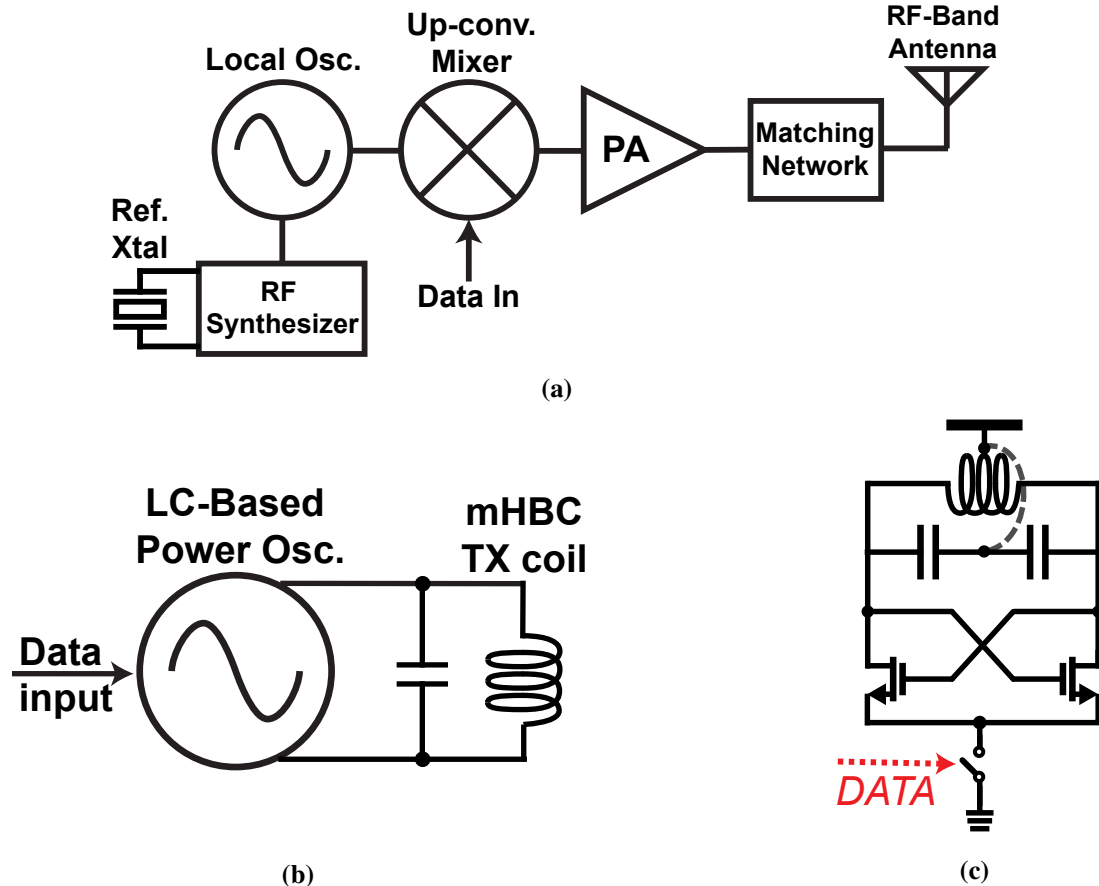


**Figure 4.6:** (a) A generic low-complexity TX architecture used in low-power wireless BANs. (b) An energy-efficient TX architecture for relatively-low TX output power. (c) A cross-coupled LC oscillator employed for the mHBC TX PO.

thesizer, the mixer, and the power amplifier can be significant, thus deteriorating the global TX efficiency of the architecture [73]. A simpler, lower-overhead approach instead utilizes an inductor as both a radiative and resonant element at RF, as depicted in 4.6b [74, 75]. This architecture is well-suitable for mHBC applications, as a coil is already needed to generate magnetic fields across the body, and can thus be simultaneously re-purposed as a resonator in a power oscillator (PO). The general structure of the power oscillator is shown in 4.6c, where the tail current source is modulated in order to quench and regenerate the oscillation for on-off-keying (OOK) modulation. Interestingly, capacitively tuning the inductor to the correct frequency enables, in conjunction with the oscillator’s positive feedback structure, automatic impedance matching of the coil, and thus no additional matching network is needed.

However, the proposed PO-based TX encounters two principal challenges related to mHBC applications, specifically regarding a trade-off between  $Q$ , path loss, and data rate, and frequency stability during motion; both of these will be described in more detail below.

## 4.2.1 Challenges of PO-based Direct-Modulation Transmitters

### Bandwidth-Path Loss Trade-off

The achievable 3-dB bandwidth of the transmitter is defined by  $f_o/Q$ . This definition implies that  $Q$  cycles are nominally required to generate or quench an oscillation to create an OOK symbol. Figure 4.7a illustrates this by showing how long it takes the PO to turn on and off for various  $Q$ -factors. Due to this restriction, a  $Q$  of 50 at 40 MHz, for example, limits the transmission data rate up to approximately 800 kbps. While faster data rates are technically possible, the oscillator does not have time to settle or quench, resulting in amplitude-shift-keying-like (ASK-like) modulation with a poor modulation index due to high- $Q$  filtering, as illustrated in Fig. 4.7b. Obviously, reducing the  $Q$  of the TX coil can ensure sufficient bandwidth for fast data transmis-

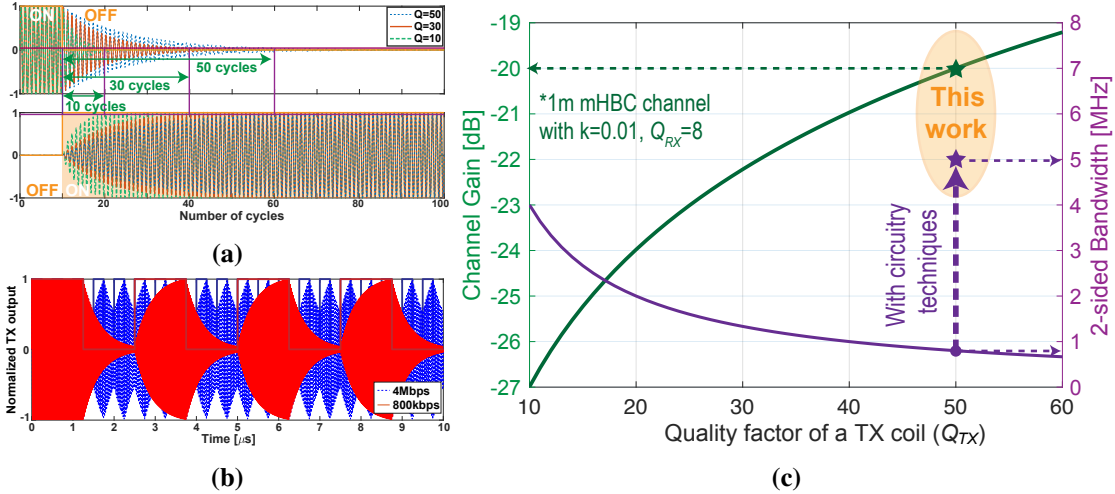


**Figure 4.7:** Bandwidth limitation caused by high  $Q$  coils: (a) Shut-down and start-up time of the PO that needs for  $Q$  cycles; (b) too fast data rate results in a poor modulation index; and (c) the trade-off between bandwidth and the channel gain.

sion. However, this  $Q$  comes with an important trade-off: path loss of mHBC systems is generally improved with higher  $Q$  coils. This trade-off is depicted in Fig. 4.7c, which shows that for the indicated coupling coefficient and  $Q_{RX}$ , going from a  $Q_{TX}$  of 10 to 50 improves the path loss by 7 dB. However, at the same time, the bandwidth decreases from 4 MHz to 800 kHz. This trade-off is one of the reasons why conventional NFC protocols utilizing low-frequency (13.56 MHz) near-field coupling cannot support high data rate communications. The specific goal of the TX design is to obviate this trade-off and enable high data rates without sacrificing path loss. Section 4.2.2 will describe how this TX design will be accomplished.

## Inductance Variation

It is well known that the inductance of a flexible wearable coil can fluctuate with normal human motion. Although rigid inductors could be used in certain embodiments (e.g., integrated into the housing of a smartphone), their inductance can still vary with environmental variation, albeit less severely than physically flexible coils. Thus, some form of inductance compensation would be useful.

Our experiments indicate that flexible wearable inductors can have inductance

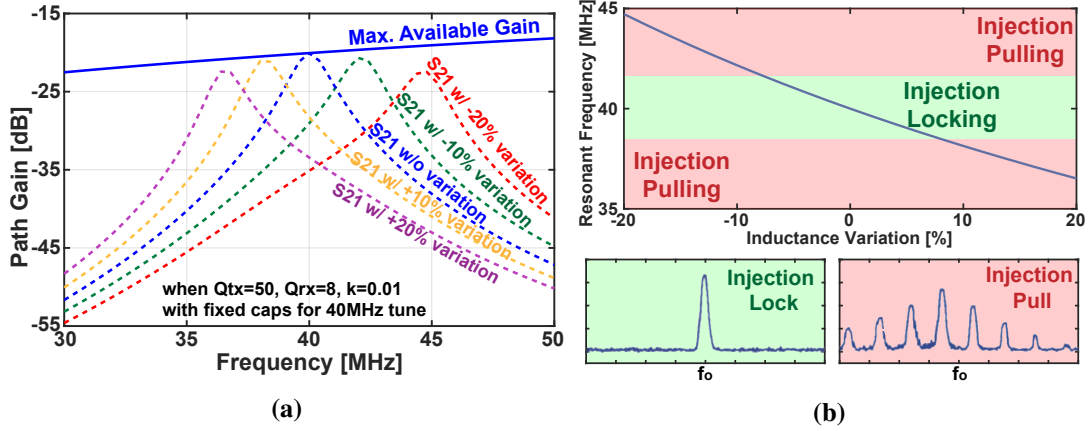


**Figure 4.8:** The inductance fluctuation of wearable mHBC coils: (a) path gain degradation by resonant frequency mismatch between TX and RX; and (b) an example of circuit malfunction: injection pulling.

variation of up to 20%. Figure 4.8a illustrates how such variation might affect path loss: without compensation, path loss could degrade by up to 15 dB at a carrier frequency of 40 MHz. One possible solution to this is to injection-lock the power oscillator. Figure 4.8b shows that injection locking can help over a  $\pm 8\%$  range, but if the resonant frequency of the PO is out of the locking range, the TX output generates harmonic tones that destroy signal fidelity. Fortunately, this inductance variation only occurs at human time scales (milliseconds), and the circuits shown in Section 4.2.2 will be able to compensate for this variation with more than sufficient speed.

## 4.2.2 TX Circuit Design

Figure 4.9 shows the proposed mHBC TX circuit design to mitigate the challenges and trade-offs described above. The PO consists of a center-tapped mHBC coil, a capacitive digital-to-analog converter (DAC) for frequency tuning, a cross-coupled pair, and a tail current source used for data modulation. To rapidly kick-start oscillations without having to wait for  $Q$  cycles as a conventional implementation would, the PO is injection locked via a 40 MHz crystal oscillator (XO) and transistors  $M_{i1}$  and  $M_{i2}$ , which together serve to accelerate oscillator start-up time by  $13.3\times$ . Injection

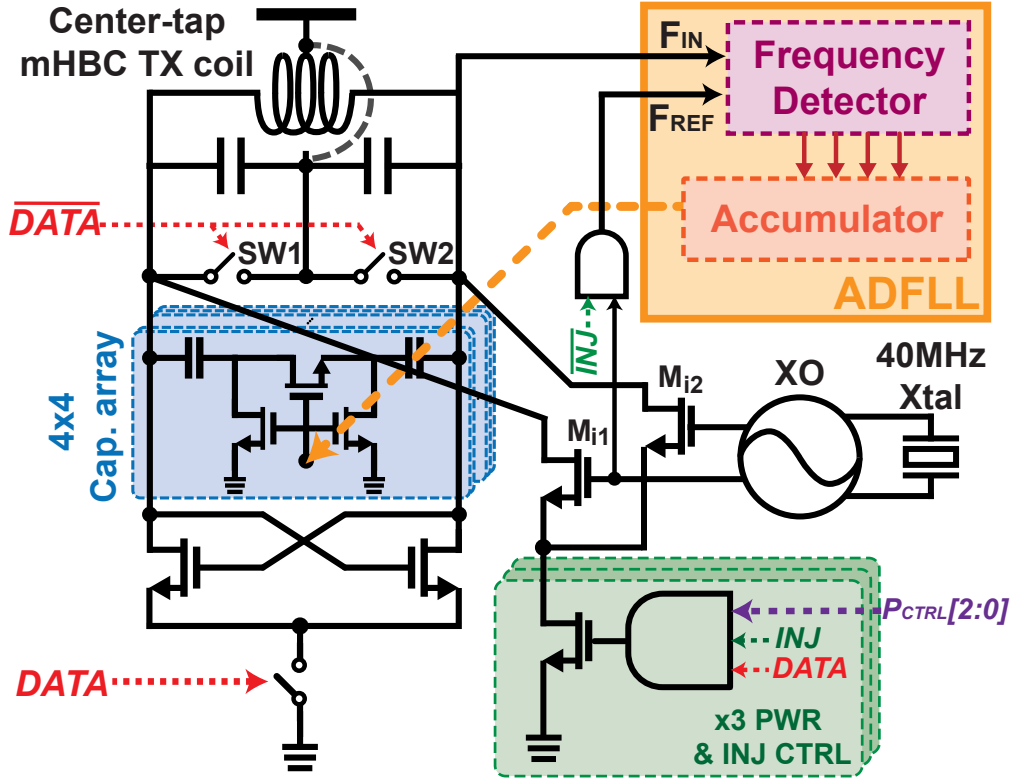


**Figure 4.9:** Proposed TX implementation for fast-data-rate communication and with dynamic resonant frequency calibration.

power control is enabled via a 3-bit binary weighted current source, enabled only when injection control is enabled and the OOK symbol to be transmitted is a logic “1”. To rapidly quench oscillations without having to wait for  $Q$  cycles, switches SW1 and SW2 are introduced, which serve to dynamically reduce the tank’s  $Q$ -factor during off times while improving the quench rate by  $10.5\times$ .

In order to ensure the TX is tuned to the correct center frequency, and to further ensure that injection locking is most beneficial, an all-digital frequency-locked-loop (ADFLL) is employed. The fast control bit output (2.5 Moutput/s) of the ADFLL depicted in Fig. 4.10 [76] enables automatic LC oscillation tuning within  $10\text{-}20\ \mu\text{s}$ , and is only activated between packets every  $1\text{-}10\ \text{ms}$ , which is sufficient to compensate for slow inductance changes ( $>50\text{-ms}$  scale) of wearable coils.

The proposed rapid kick-start and quenching circuits, along with the ADFLL,



most ultra-low-power receiver architectures utilize a direct envelope-detector-based approach [77–80]. The following subsection will discuss the typical challenges of such approaches, and how mHBC can help.

### 4.3.1 Design Challenges of Direct-ED Receivers

The most problematic characteristic of direct-ED receivers is that they demodulate everything at their input to baseband - including interferers. Figure 4.11a shows the common-source-amplifier-based (CS-amp-based) ED with an RC low-pass filter implemented in the proposed mHBC RX. Because this ED performs down-conversion utilizing 2nd-order intermodulation harmonics, the conversion gain,  $A_{v,conv}$ , is determined by the 2nd-order transconductance,  $g_{m2}$ , of the employed MOSFET, and the magnitude of the input fundamental carrier tone. Without careful filtering, all broadband interference will be down-converted to baseband, which causes demodulation failure as illustrated in Fig 4.11b. To minimize this issue, [78–80] implemented high- $Q$  front-end filters to reject interference.

Fortunately, mHBC can alleviate the interference susceptibility thanks to its physically-inherited properties. First of all, an mHBC receiver naturally has a decent bandpass filter via its RX coil. Since there is no easy way to enable wideband data reception at the RX without a priori knowledge of the incoming data, a low- $Q$  coil must

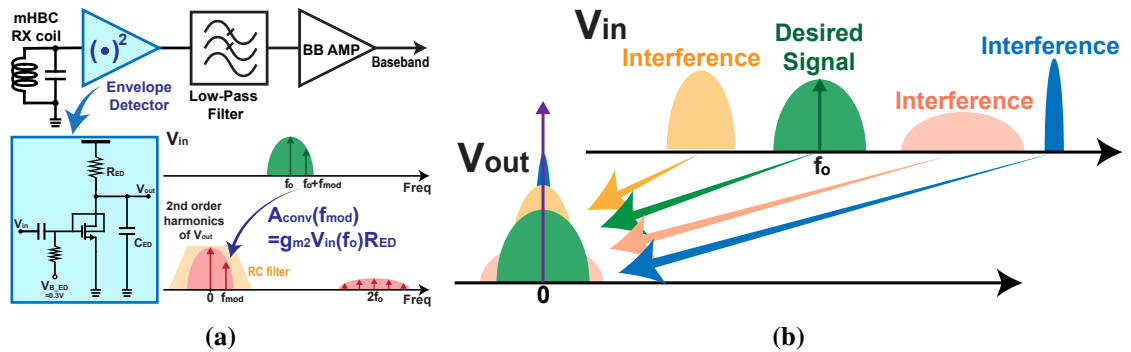


**Figure 4.11:** (a) A CS-amp-based ED with a RC filter and its down-conversion gain by 2nd-order inter-modulation. (b) The interference issue plaguing non-coherent down-conversion receivers without channel selection filters.

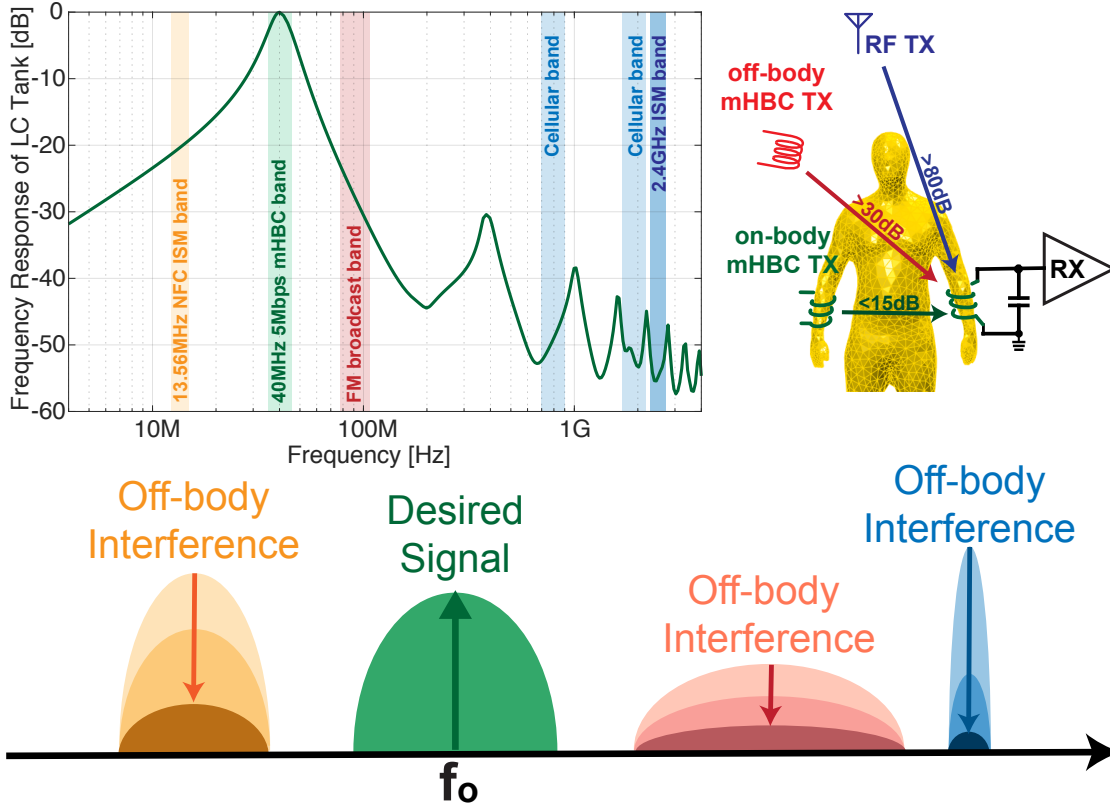


**Figure 4.12:** An additional benefit of mHBC: interference rejection by the RX coil and the human body channel itself.

be used (noting that the same coil as the TX could be used, but with intentionally de- $Q$ -ing resistors added to the tank). Despite a lower than desired  $Q$  (e.g.,  $Q_{RX}=8$  here for 5-Mbps data transfer), the coil still has the frequency response shown in Fig. 4.12, which shows rejection of interference at the 2.4 GHz ISM band, the FM radio band, and the 13.56 MHz NFC ISM band by up to 56 dB, 33 dB, and 22 dB, respectively. More importantly, the body itself helps to provide additional rejection. As depicted in Fig. 4.3, RF radios and other off-body magnetic sources (e.g., NFC) have up to 80dB and 25dB more path loss around the body than on-body mHBC, respectively.

Therefore, a direct-ED architecture, when used in an mHBC receiver, can tolerate reasonable levels of out-of-band interference, and can thus help enable a low-power implementation. Anecdotal testing of the developed receiver in a typical un-shielded lab environment did not show any interference sensitivities. In-band interference, however,

can potentially directly degrade the ability to receive the correct signals. While in-band interference is expected to be rare at 40 MHz, a very proximal mHBC user could potentially cause tangible interference. To mitigate this, frequency division multiplexing (FDM) or time division multiple access (TDMA) functionality can be added in future work.

It should also be noted that  $A_{v,conv}$  of ED is determined by the voltage magnitude of the fundamental input tone, which can result in poor gain and noise performance depending on the input signal level. For instance, the -55 dBm RX input power of the target RX sensitivity produces a 2 mV input voltage swing with the designed RX mHBC coil. Given a power budget of 3  $\mu$ W (0.6 V and 5  $\mu$ A) and  $R_{ED}$  of 80 k $\Omega$  (for  $V_{OUT} > 100$  mV),  $A_{v,conv}$  is only 0.443 (-7 dB) and the noise figure (NF) is 55.5 dB, which provides -39.5 dBm RX sensitivity - not good enough. To mitigate this problem, a preamplifier was implemented for better  $A_{v,conv}$  and NF, and finally better RX sensitivity. At 40 MHz, the preamplifier power is not exorbitant and is well justified to help improve sensitivity.

### 4.3.2 RX Circuit Design

The overall receiver architecture is shown in Figure 4.13. As described above, a preamplifier is placed in front of the ED to improve RX sensitivity. The amplifier utilizes an n-type dynamic-threshold MOSFET (DTMOS) for inclusion of  $g_{mb}$ . Fig. 4.14a shows that this improves transconductance efficiency ( $g_m/I_D$ ) by up to 17% when

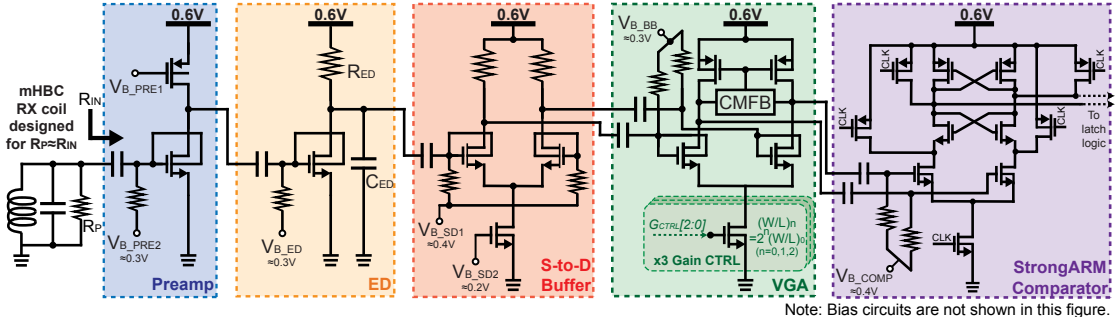


**Figure 4.13:** Proposed ultra-low power and energy-efficient mHBC RX architecture and its circuit-level design.

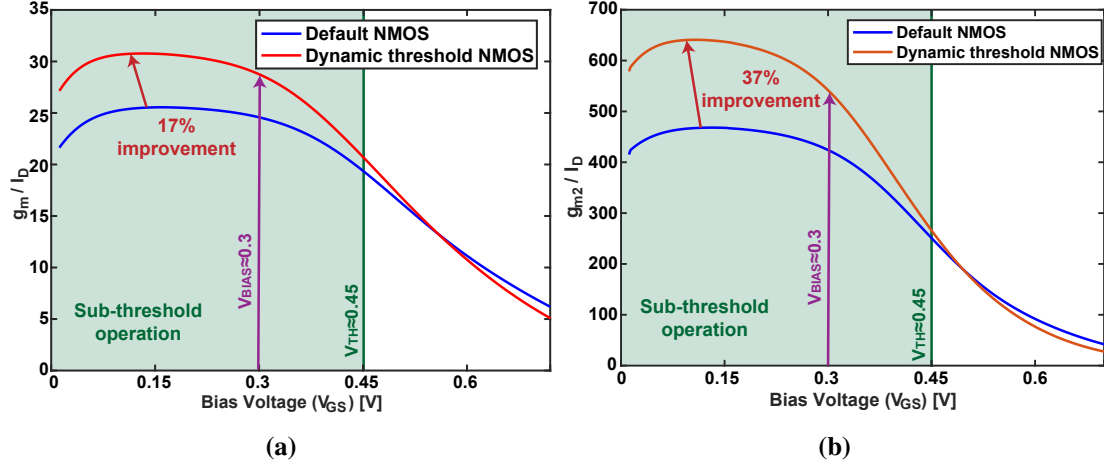


**Figure 4.14:** Improvement of (a) first-order transconductance efficiency and (b) second-order transconductance efficiency of an n-type dynamic-threshold MOSFET in deep sub-threshold operation.

biased into deep subthreshold. The preamplifier was designed to achieve a voltage gain of 19 dB and a noise figure of 31.6 dB, all for 1.8  $\mu\text{W}$  of power consumption. While the noise figure may at first glance sound awful, the power consumption is extremely low and, most importantly, the achieved sensitivity meets the needs of the mHBC link budget, as will be described shortly.

The CS-amp-based ED also employs an n-type DTMOS amplifier, in this case, to enhance the 2nd-order transconductance via  $g_{mb2}$ , enabling a 37% improved 2nd-order transconductance efficiency ( $g_{m2}/I_D$ ) as shown in Fig. 4.14b. By cascading the preamplifier and ED, the down-conversion front-end was designed to achieve  $A_{v,conv} = 31.1$  dB and a noise figure of 35.9 dB for 2 mV RX input voltage, which results in -59.1 dBm RX sensitivity with 2.4  $\mu\text{W}$  total power consumption. This RX front-end meets the needs of the proposed mHBC system.

After envelope detection, a single-to-differential (S-to-D) buffer is used to lessen susceptibility to power supply fluctuations and provide low-pass filtering that helps to reject high-frequency harmonics. Here, the S-to-D buffer was designed with low- $V_t$  devices to minimize input capacitance in order to ensure a 2.5 MHz cut-off frequency of the ED RC filter ( $R_{ED}=400$  k $\Omega$  and  $C_{ED}=150$  fF). The S-to-D buffer then drives

a fully-differential 3-bit variable gain amplifier (VGA). While the VGA compensates the variable noise level of an ultra-low power comparator, a common-mode feedback (CMFB) circuit adjusts the common-mode voltage of VGA output to the appropriate value to minimize the error of the next-stage comparator. Also, by implementing the oversampling decision scheme in an ultra-low power StrongARM comparator and the following latch logic, the RX architecture can successfully demodulate data without a power-hungry synchronization block. For the better impedance matching performance between the mHBC RX coil and the RX input, the RX coil was designed for the parallel resistance ( $R_P$ ) at the resonant frequency (40MHz) of the LC tank to have the same resistance value of the RX input.

## 4.4 Measurement Results

As summarized in Fig. 4.15, the mHBC TRX was fabricated in  $1 \times 1 \text{ mm}^2$  in 65 nm LP CMOS, and operates with a 0.6 V supply while supporting up to 5 Mbps OOK modulation at 40 MHz with a high- $Q$  ( $>50$ ) TX coil. The core area of the chip is only  $0.12 \text{ mm}^2$  as illustrated by the layouts shown in Fig. 4.15. The full transceiver requires two external coils, several off-chip shunt tuning capacitors, and a reference crystal. Depending on the power source (e.g., battery voltage), some sort of power management circuits would be needed too [e.g., a 0.6 V low-dropout (LDO) regulator].

Figure 4.16 shows the measured TX output waveform under the worst-case modulation that alternates between 1s and 0s at 5 Mbps. With the implementation of the accelerated quenching and oscillation kick-start circuits, the mHBC TX improves the ASK-like modulation index from 15.4% to 84.7%. Figure 4.17 shows OOK spectrum results modulated by externally-applied pseudo random binary sequence (PRBS) bits at data rates of 1.25, 2.5, and 5 Mbps. The signal spectral results were received by an mHBC RX coil across a pre-measured 12-dB-path-loss channel (10 cm distance in air with  $Q_{TX}=50$  and  $Q_{RX}=8$  of the wire-wound wearable coils designed only for test-bench measurements) including bandpass filtering by the RX coil and a narrowband

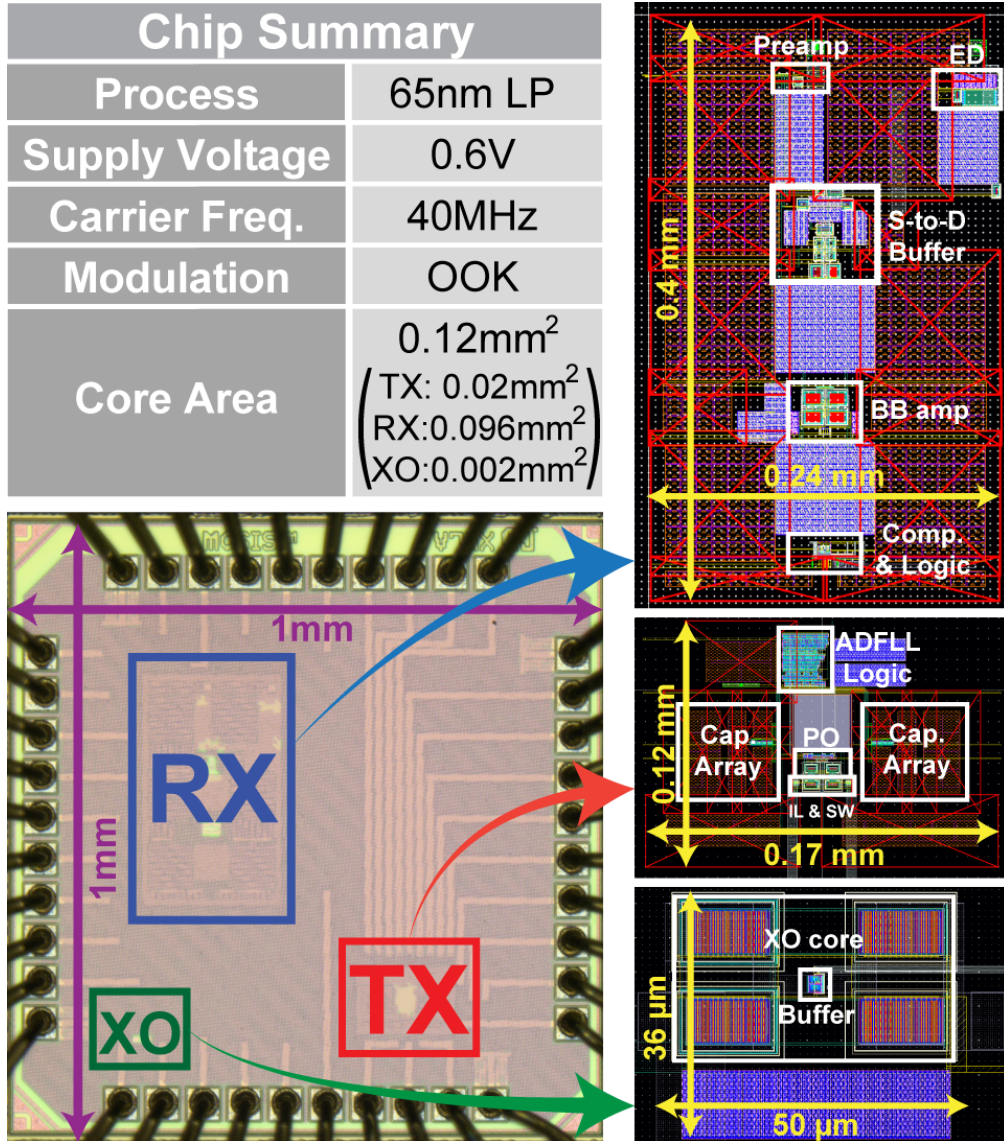


**Figure 4.15:** A implementation summary table, the die photograph, and the layouts of the proposed mHBC transceiver

matching network only for the 50  $\Omega$  spectrum analyzer input. When de-embedding the filtering of the measurement setup, the main lobe of the modulated TX output is estimated to have a 3-dB bandwidth of 1.24, 2.38, and 4.7 MHz at data rates of 1.25, 2.5, and 5 Mbps, respectively (ignoring the large carrier feedthrough tone due to the lack of phase scrambling).

Figure 4.18 depicts the spectrum and frequency tracking results of dynamic res-

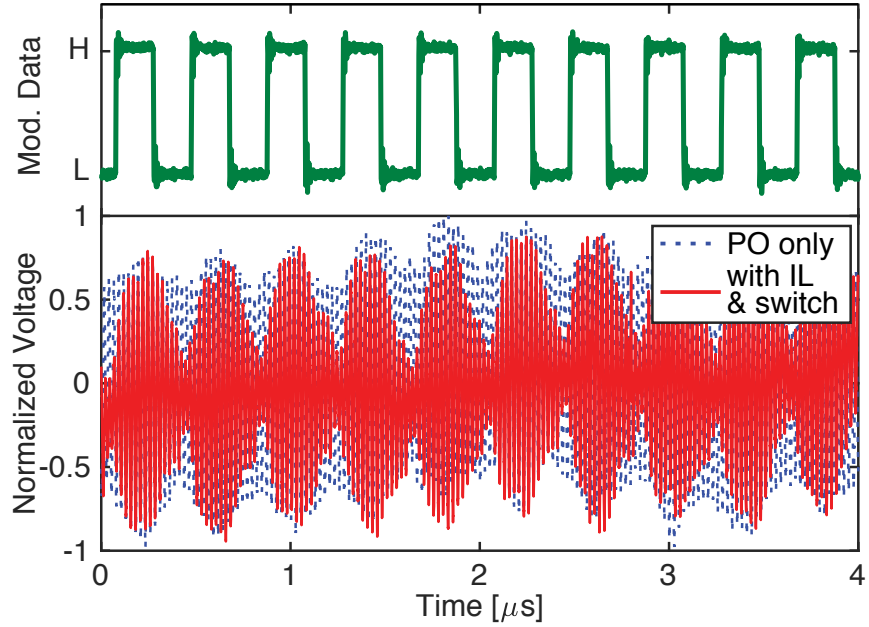


**Figure 4.16:** Measurement results of the high data rate capability of the proposed mHBC TX:  $5.5\times$  improved modulation index by rapid-quenching and kick-start circuits.

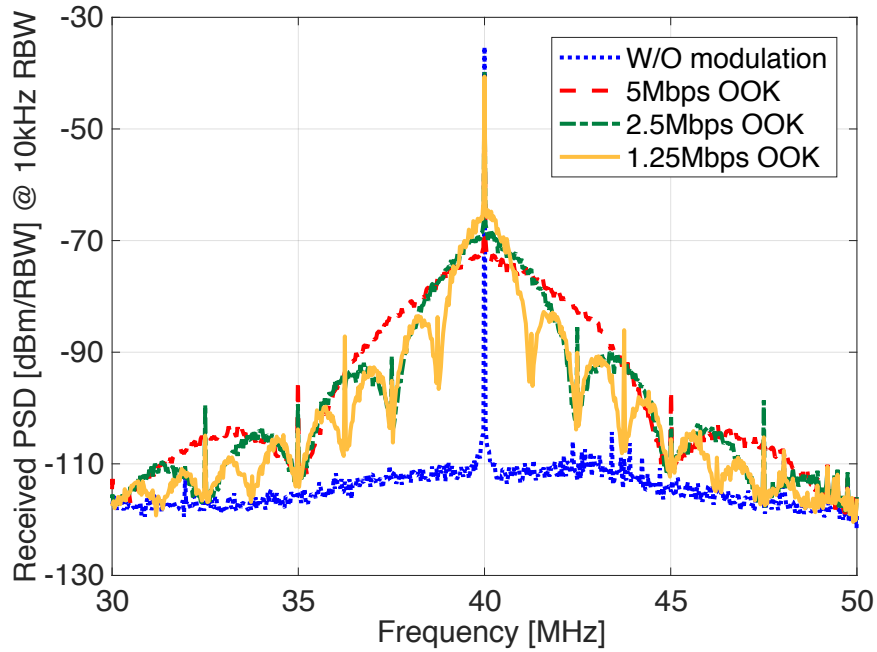


**Figure 4.17:** Measurement results of the high data rate capability of the proposed mHBC TX: measured OOK modulated spectra with various data rates, received by a wire-wound RX coil ( $Q_{RX}=8$ ) with 10-cm distance air (12-dB loss).

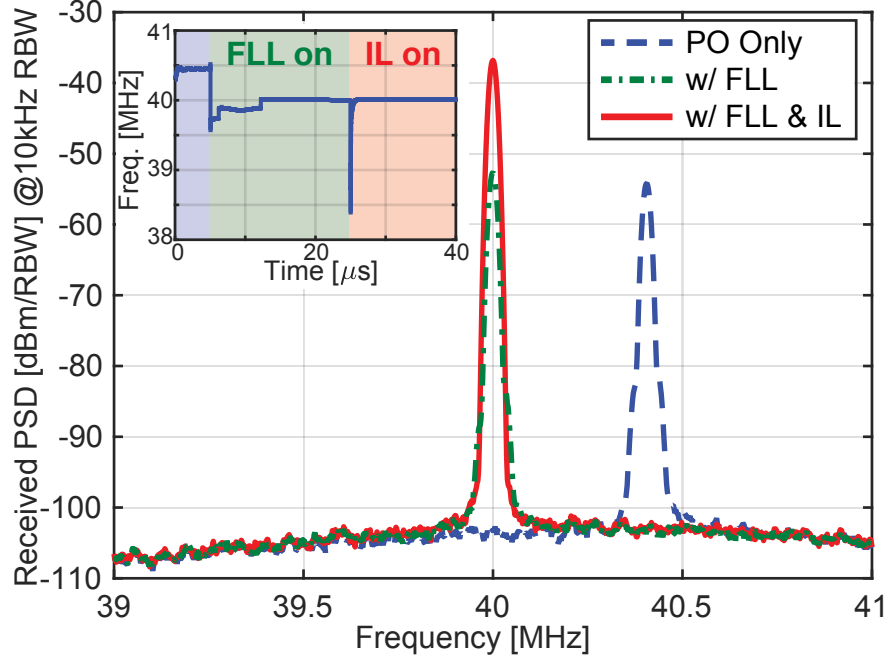


**Figure 4.18:** Measurement results of dynamic resonant frequency calibration for the proposed mHBC TX: measured spectrum and frequency tracking waveform (inset) of ADFLL operation.

onant frequency calibration by the ADFLL. Here, to confirm whether the designed ADFLL was working correctly, the LC resonance of the TX PO was intentionally off-tuned to 40.4 MHz (blue dashed line in Fig. 4.18). Once the FLL starts operating, the capacitor-array DAC in the PO is automatically adjusted to set the oscillation frequency to 40 MHz (green dashed line in Fig. 4.18) in 10  $\mu\text{s}$  as shown in the measured frequency-tracking result (the inset plot of Fig. 4.18).

As depicted in Fig. 4.19, the  $4 \times 4$  capacitor-array DAC with 0.2-pF unit capacitors was designed to cover  $\pm 10\%$  inductance variation of a 960-nH mHBC TX coil because a printed-circuit-trace coil for hand-held mHBC applications in Section 4.5 has lower inductance fluctuation ( $< \pm 10\%$ ) than flexible wearable coils. The inductance values for 40 MHz resonance were calculated in Fig. 4.19 with the tuning capacitance (DAC + off-chip fixed capacitors) estimated by the measured resonant frequencies according to the DAC bit configurations and the fixed 960-nH mHBC TX coil.

After a 20  $\mu\text{s}$  calibration period to set the PO resonance frequency in the injection

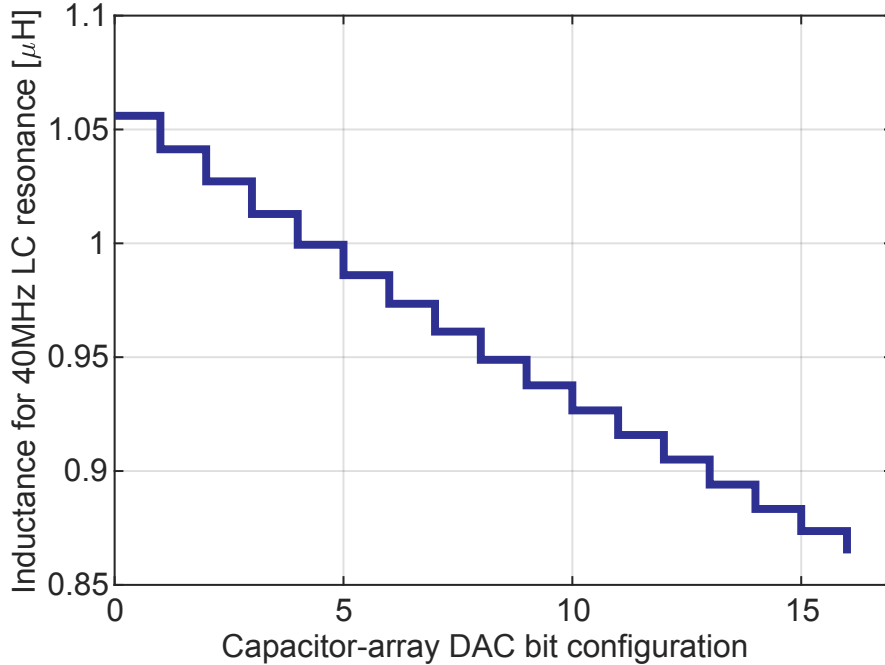
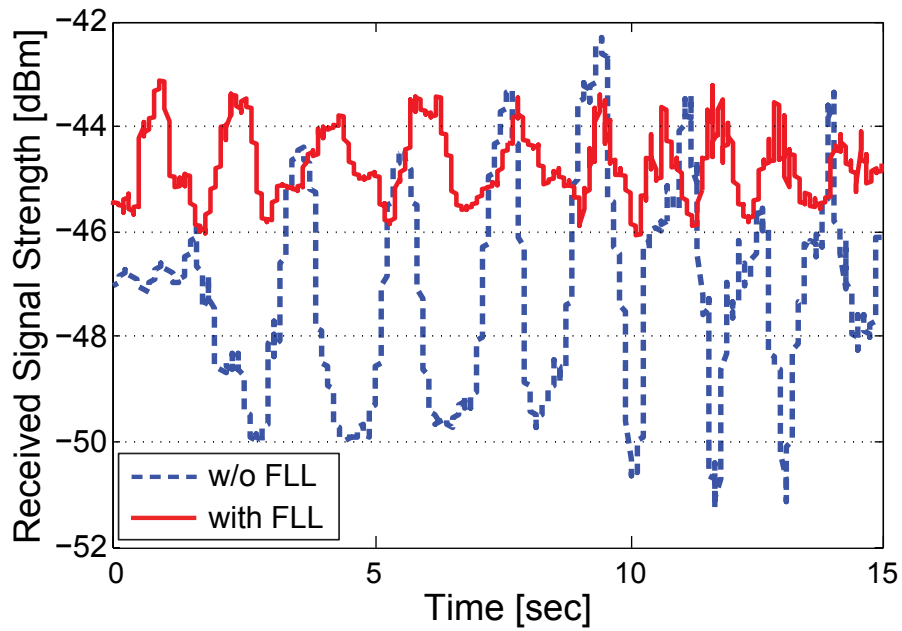


**Figure 4.19:** Measurement results of dynamic resonant frequency calibration for the proposed mHBC TX: measured inductance variation coverage by capacitor-array DAC in ADFLL.

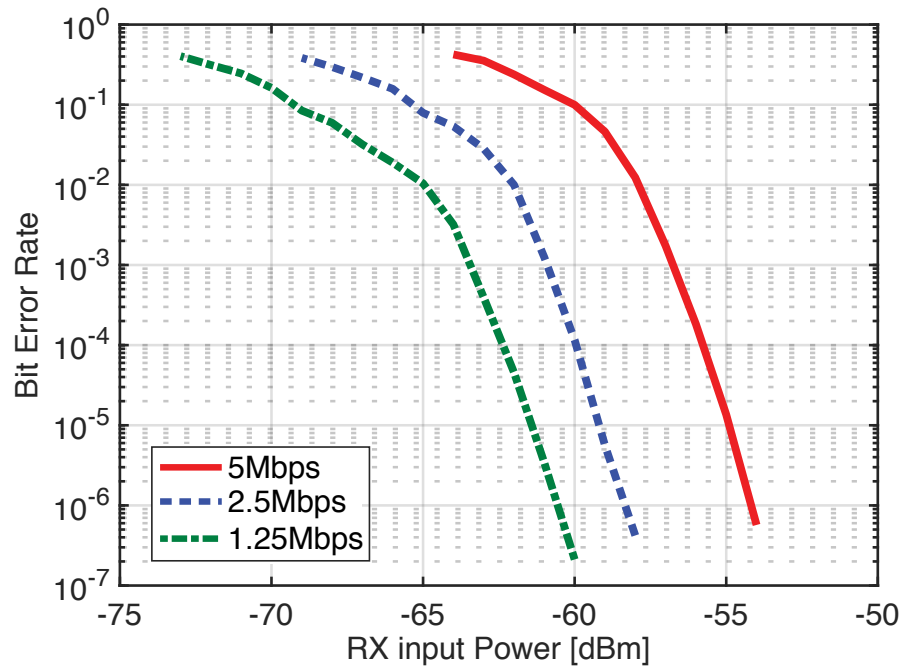
locking range, the injection locking block is turned on to provide the rapid kick-start behavior described in Section 4.2 and enhance the TX output power by 17.4dB (red solid line in Fig. 4.18).

In 3D FEM simulation in Ansys HFSS, a TX output power of -24.8 dBm in the TX default mode causes  $73 \mu\text{W}/\text{kg}$  specific absorption rate (SAR), which is much less than the  $2 \text{ W}/\text{kg}$  IEEE regulation. The H-field flux density is 3.2 nT, which is significantly less than an MRI machine (1.5 T), and is even less than earth’s magnetic field ( $65 \mu\text{T}$ ).

Figure 4.20a depicts the received signal strength variation under ordinary walking conditions. Due to both the mis-tuned carrier frequency caused by varying inductance of the TX LC tank and the different channel distance in moving, the received power can be fluctuating by up to 8.9 dB. However, once the ADFLL helps calibrate the resonant frequency to the designed carrier frequency automatically, the received signal strength fluctuates only up to 2.9 dB, which matches the posture data in Fig. 4.4 well.



(a)



(b)

**Figure 4.20:** RX measurement results: (a) received signal strength variation under inductance fluctuation by user's moving when the TX output power is -24.8dBm at 40 MHz and (b) RX bit-error-rate results with various data rates.

Figure 4.20b shows the RX bit-error-rate (BER) measurement results representing that the 0.1% BER RX sensitivity is  $-63.5$  dBm to  $-56$  dBm at data rates from 1.25 to 5 Mbps, respectively. These BER results were measured by providing the output of a signal generator that has a configurable output impedance to match the RX input ( $1.8$  k $\Omega$ ). The BER measurements were performed using  $2\times$  oversampling decision logic with a clock generated separately by an on-chip XO for asynchronous and non-coherent demodulation conditions. Here, all the curves in Fig. 4.20b depict the averaged BER curves over ten measurements with arbitrary phase differences between the modulated input signals and the RX logic clock.

Figure 4.21 demonstrates that a pair of mHBC transceivers with  $-24.8$  dBm TX output power and  $-56$  dBm RX sensitivity settings successfully operated across a human body at 5 Mbps with 388 ns latency (path loss was 20 dB over a 1 m mHBC channel,  $Q_{TX}=50$  and  $Q_{RX}=8$ ).

As summarized in Fig. 4.22a, the mHBC TX transmits  $-24.8$  dBm output power with  $18.6$   $\mu$ W of power consumption in the default mode, resulting in an energy effi-

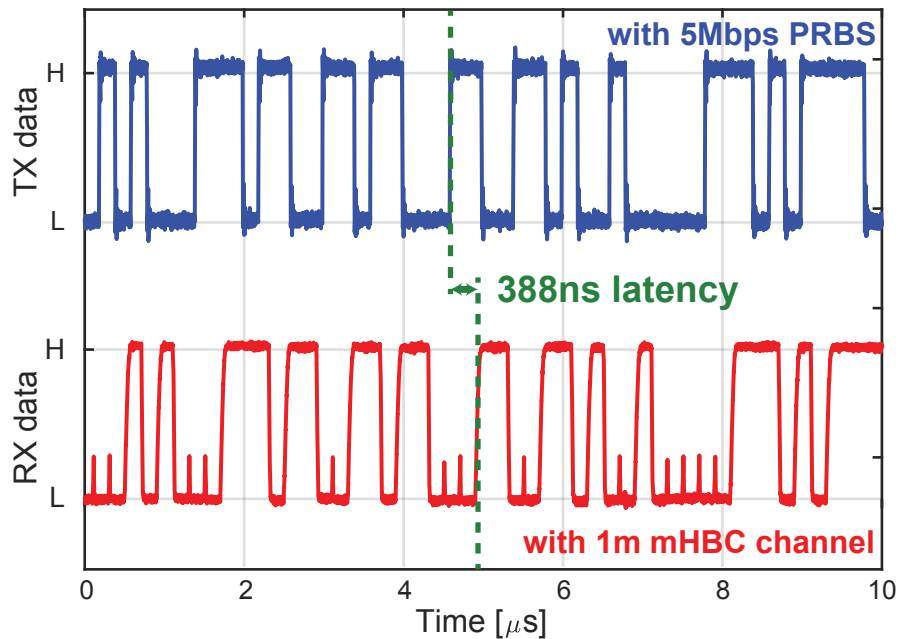


**Figure 4.21:** Measured waveform results of 1-m trans-body TX-to-RX data transfer.

ciency of 3.7 pJ/bit and a TX global efficiency of 9.3%. These TX performance metrics can be improved by changing the TX operation mode (e.g., 1.5 pJ/bit with -34.1 dBm minimum TX output mode, and 13.5% with -22.3 dBm maximum TX output mode). To the authors' knowledge, this is the first wireless BAN transmitter achieving >5% TX global efficiency with <-20 dBm TX output power [73]. With 1.3 pJ/bit energy-efficiency at 6.3  $\mu$ W of power consumption, the mHBC RX achieves a sensitivity of -56dBm in the default mode and supports a 1.5-m mHBC channel using a -24.8 dBm TX output. When including the 17.2  $\mu$ W from the on-chip XO, the TX and RX consume 35.8  $\mu$ W (7.15 pJ/bit) and 23.5  $\mu$ W (4.7 pJ/bit), respectively. This proposed mHBC transceiver is the lowest power and most energy-efficient amongst reported eHBC transceivers when including the energy cost of frequency synthesis as shown in Fig. 4.22b and Table. 4.1.

## 4.5 Demonstration

To demonstrate that the designed mHBC transceiver is capable of operating in a practical wearable application, a Hi-Fi audio data streaming system was developed. As illustrated in Fig. 4.23a, 2-channel analog audio data from a smartphone was converted

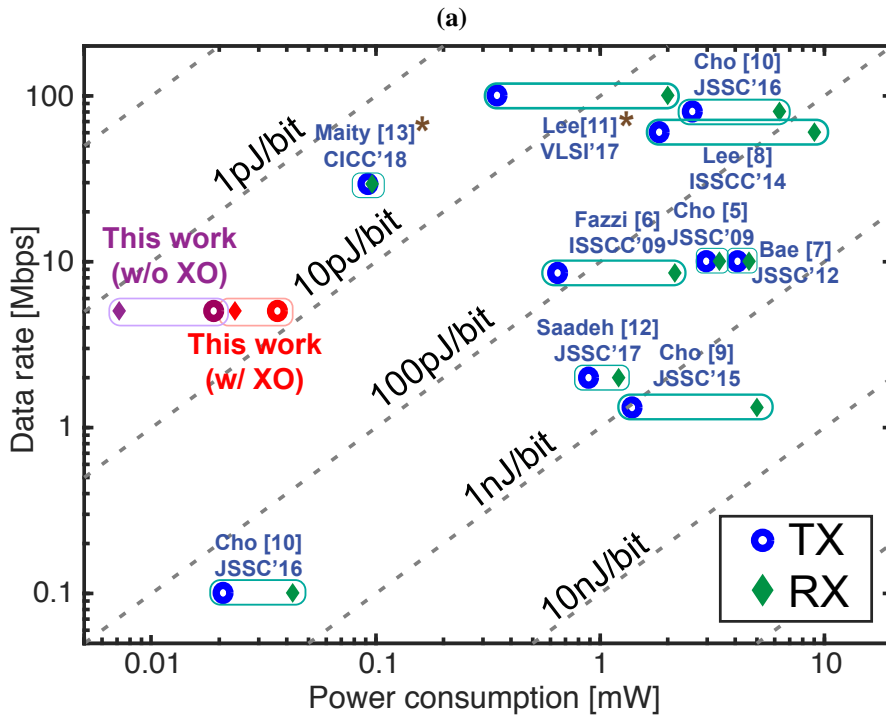
**Table 4.1:** Performance Comparison Table

	N. Cho [62] JSSC'09	A. Fazzi [63] ISSCC'09	J. Bae [64] JSSC'12	J. Lee [65] ISSCC'14	H. Cho [66] JSSC'15	H. Cho [67] JSSC'16	J. Lee [68] VLSI'17	W. Saadeh [69] JSSC'17	S. Maity [70] CICC'18	This work	
CMOS process	180nm	130nm	180nm	65nm	130nm	65nm	65nm	65nm	65nm	65nm	
HBC scheme	eHBC									mHBC	
Frequency band [MHz]	30 - 120	1 - 30	40 - 120	40 - 120	18.375 - 23.625	20-60 140-180	13.56	0 - 50	20-120	0 - 15	37.5 - 42.5
Modulation	FSK	Direct Digital	Double FSK	3-level Walsh	BPSK	BPSK	OOK	Direct Digital	P-OFDM BPSK	Direct Digital	OOK
Supply [V]	0.9	1.2	1	1.1	1.2	1.2	0.8	Not Reported	1.1	1	0.6
Maximum data rate	10Mbps	8.5Mbps	10Mbps	60Mbps	1.3125Mbps	80Mbps	100kbps	100Mbps	2Mbps	30Mbps	5Mbps
TX power consumption	2.35mW	0.652mW	3.8mW	1.85mW	1.4mW	2.6mW	21 $\mu$ W	0.35mW <sup>†</sup>	0.87mW	93 $\mu$ W <sup>†</sup>	36.7 $\mu$ W
TX E/bit (w/ XO) [pJ/bit]	235	76.7	380	30.8	1067	32.5	210	3.5 <sup>†</sup>	435	3.1 <sup>†</sup>	7.15
RX power consumption	3.7mW	2.15mW	3.2mW	9.02mW	5mW	6.3mW	42.5 $\mu$ W	2mW <sup>†</sup>	1.1mW	98 $\mu$ W <sup>†</sup>	23.5 $\mu$ W
RX sensitivity [dBm]	-65	-60	-66	-62	-98.3	-58	-72	Not Reported	-83.1	-63.3	-56.6
RX E/bit (w/ XO) [pJ/bit]	370	253.2	320	150.3	3810	78.8	425	20 <sup>†</sup>	550	3.27 <sup>†</sup>	4.7

<sup>†</sup> Note: Not including the power of frequency synthesis.

Setting		Min.	Default	Max.	
XO	Power [ $\mu$ W]	17.2			
	Output power [dBm]	-34.1	-24.8	-22.3	
TX (w/ 50% OOK Mod.)	Power [ $\mu$ W]	PO (with IL)	7.1	18.2	26.0
		ADFL* <sup>*</sup>	0.02		
		Ctrl Logic	0.34		
		<b>Total</b>	<b>7.46</b>	<b>18.56</b>	<b>26.36</b>
	TX eff. (w/ XO) [%]	<b>2.7</b>	<b>9.3</b>	<b>13.5</b>	
	E/bit [pJ/bit]	<b>1.5</b>	<b>3.7</b>	<b>5.3</b>	
RX	Sensitivity [dBm] (0.1% BER)		-54	-56	-57
	Power [ $\mu$ W]	Preamplifier	1.8		
		ED	0.53		
		S-D buffer	2.6		
		BB VGA	0.94	1.3	1.9
		Comp. + Logic	0.07		
		<b>Total</b>	<b>5.94</b>	<b>6.3</b>	<b>6.9</b>
	E/bit [pJ/bit]		<b>1.2</b>	<b>1.3</b>	<b>1.4</b>

\* Note : Operates for 20- $\mu$ s duration every 1 ms.



\* Note: Not including the power of frequency synthesis.

**Figure 4.22:** (a) A summary of the proposed mHBC TRX specification. (b) E/bit comparison to the prior eHBC TRXs.

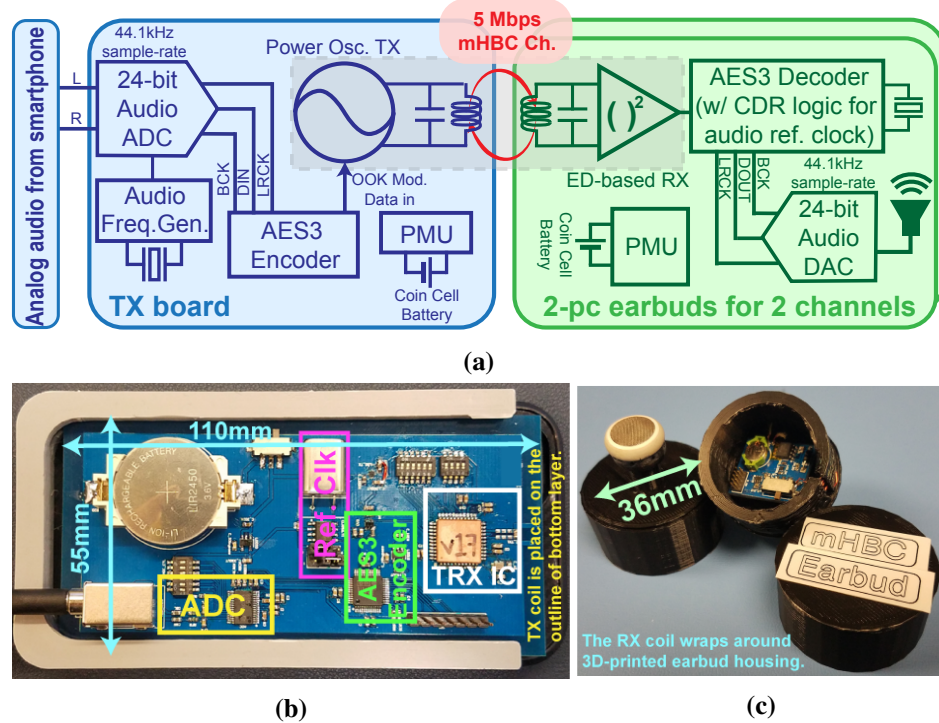


**Figure 4.23:** A Hi-Fi audio streaming demonstration: (a) demonstration block diagram; (b) mHBC TX unit prototype fitted in a compact-sized smartphone; (c) mHBC RX headphone unit prototypes.

to a 5 Mbps lossless and non-compressed AES3 format, commonly employed in high-performance wired digital audio interfaces, via a 2-channel 24-bit audio ADC and an AES3 encoder.<sup>1</sup> Once the digitized audio data was applied to the mHBC TX data input, the TX generated a 40-MHz 5-Mbps OOK-modulated signal with a 1 mm width 2-turn mHBC TX coil ( $Q_{TX}=50$ ,  $L_{TX}=960$  nH) printed on the outline of 1-oz copper print circuit board (PCB) mounted on the smartphone.

As depicted in Fig. 4.23b, the designed TX PCB board contains all the components for audio data transmission, such as an ADC, an AES3 encoder, an mHBC TX, a TX coil, and power management blocks with a coin-cell battery, in the same size as a compact smartphone ( $11 \times 5.5$  cm<sup>2</sup>), which mimics when the TX coil is deployed inside the smartphone. As shown in Fig. 4.23c, the mHBC RX unit employed a 32-mm

<sup>1</sup>It should be noted that this is not necessarily a pragmatic demonstration - compressed audio is likely a better solution here. However, the main point of this demonstration is to show it is possible to transmit high data rates across the body with high throughput.

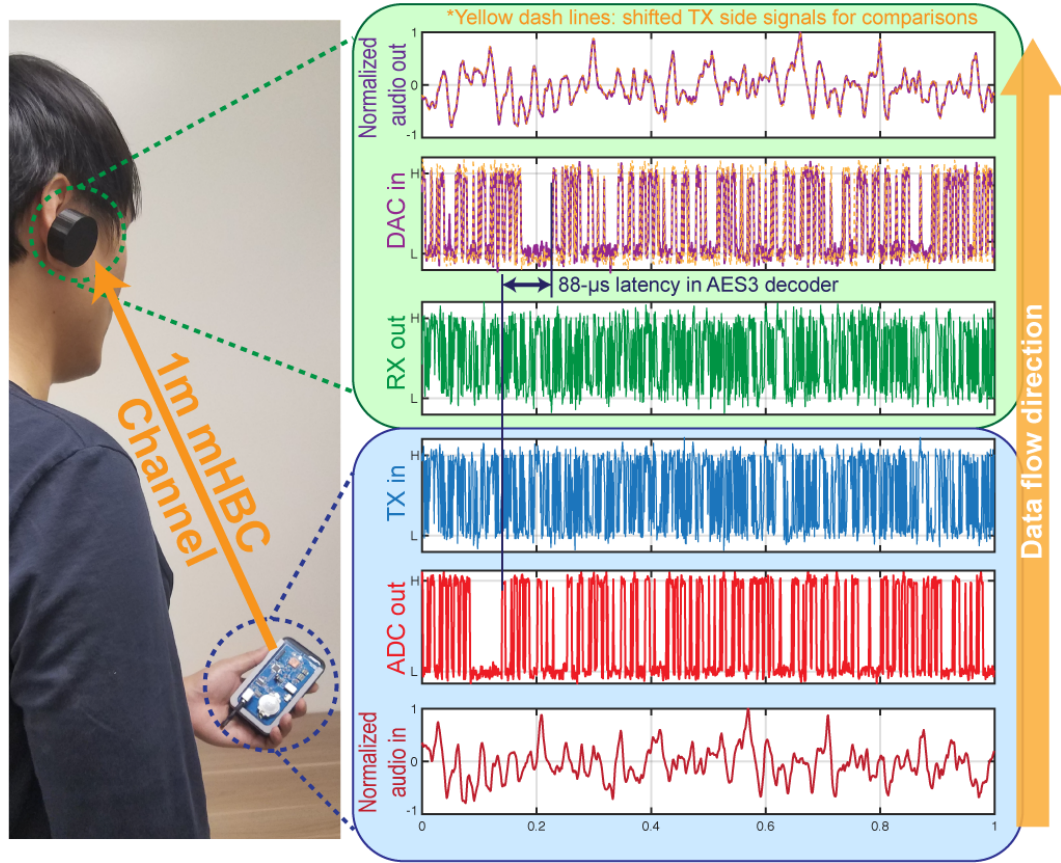


**Figure 4.24:** Waveform results of the proposed mHBC Hi-Fi audio streaming system.

diameter 4-turn wire-wound coil ( $Q_{RX}=7.6$  and  $L_{RX}=495$  nH) mounted inside an in-ear headphone prototype housing while playing the delivered audio data via the AES3 decoder and DAC.

Figure 4.24 shows that audio data was successfully transmitted from the smartphone TX unit to the headphone RX unit over a 1 m mHBC channel with no error bits and  $<90 \mu\text{s}$  latency ( $88 \mu\text{s}$  latency caused by the AES3 decoder), thereby demonstrating that the proposed mHBC transceiver can be used as a real body-area network.

## 4.6 Conclusion

This chapter has presented the first transceiver designed to exploit the low path loss of mHBC communication channels. Implemented in  $0.12 \text{ mm}^2$  of core-area in

65 nm, the TX and RX require only 7.15 and 4.7 pJ/bit, respectively, which exceeds the efficiency of prior-art BAN systems that include frequency synthesis by an order of magnitude, all at the lowest demonstrated power consumption when closing a real human body channel link. State-of-the-art efficiency was accomplished by exploiting the inherently low gain of mHBC links to design an ultra-low-power sub- $V_{TH}$  DTMOS-based RX circuits with minimal sensitivity requirements, while employing a direct-PO TX with synchronous kick-start via an ADPLL to raise the data rate when utilizing a high- $Q$  TX coil. A Hi-Fi audio streaming via the designed mHBC transceiver validates the practicality of the promising mHBC scheme.

Chapter Four is largely a combination of material in the following two papers: "A Sub-40 $\mu$ W 5Mb/s Magnetic Human Body Communication Transceiver Demonstrating Trans-Body Delivery of High-Fidelity Audio to a Wearable In-Ear Headphone," in IEEE International Solid-State Circuits Conference (ISSCC), February 2019, and "A Sub-10-pJ/bit 5-Mb/s Magnetic Human Body Communication Transceiver," in IEEE Journal of Solid-State Circuits (JSSC), November 2019, which both are written by Jiwoong Park and Patrick P. Mercier. The author is the primary author and investigator of this work.

# Chapter 5

## Wireless Powering of Millimeter-Scale Fully-on-Chip Neural Interfaces

Miniaturized implantable microchips featuring on-chip electrodes, amplifiers, stimulators, and wireless power transfer (WPT) and telemetry capabilities can offer electrical access to the cortical surface at high electrode density for next generation information-rich, long-lasting, and robust brain-machine interfaces (BMI). If the fully-on-chip neural interfaces are smaller than the radius of curvature of the cortical surface (i.e., at mm-scales), many such chips can be arrayed across the curves of the cortical surface (Fig. 5.1), potentially enabling higher global electrode density over a larger total area than more conventional ECoG or  $\mu$ ECoG [81]. As fully wireless modular devices, interconnect problems that burden conventional approaches are eliminated.

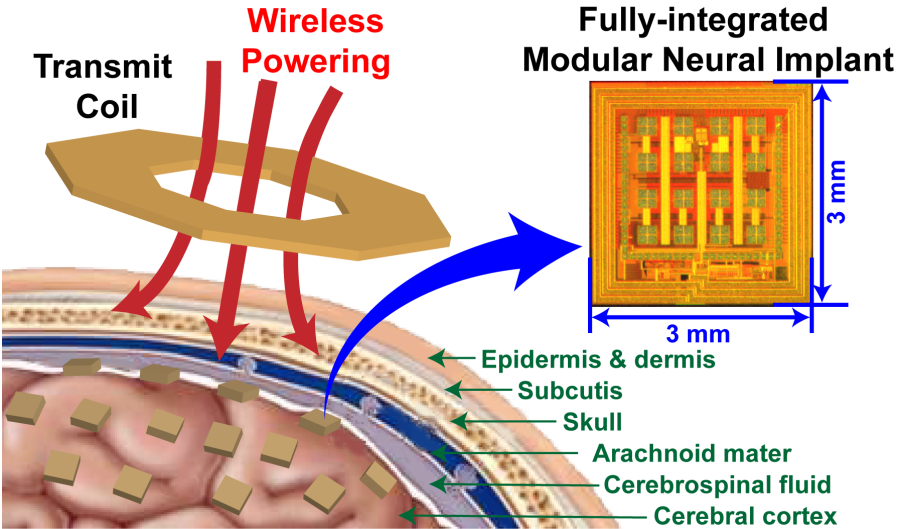


**Figure 5.1:** Overview of fully-on-chip modular neural implants. The inset die photo illustrates the on-chip coil and interior active circuitry.

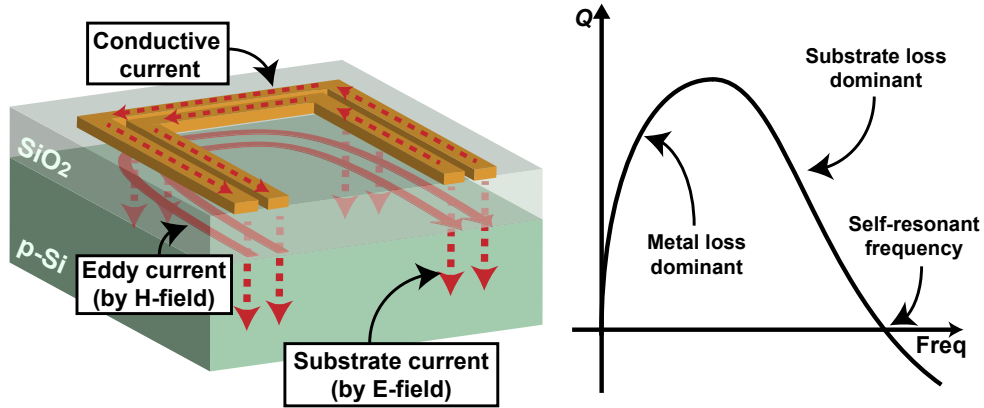


**Figure 5.2:** Loss mechanisms in an on-chip coil and its typical quality factor as a function of frequency.

However, the achievable quality factor ( $Q$ ) of mm-scale on-chip coils is low for several reasons as illustrated in Fig. 5.2, which results in low power transfer efficiency (PTE) when coupled with the small physical size of the on-chip coils and relatively large transcutaneous separation between the implant and an external driving coil [82]. For example, the limited area and trace width/spacing design rules, along with its sheet resistance and proximity effect between traces, results in finite parasitic resistance in the on-chip coils [83]. Also, the P-type silicon (p-Si) substrate for ICs yields loss mechanism that contributes to additional resistance in the coils as well as parasitic capacitance that reduce the self-resonant frequency (SRF) [84]. In addition, unlike conventional on-chip inductors which have an interior blank for magnetic flux and a guard ring for isolation from peripheral circuitry, the inner of on-chip coils for modular neural implants would be filled with neural interface circuits and electrodes for integration, which reduces  $Q$  of the coils by blocking magnetic flux while introducing severe interference to sensitive circuits. Also, the  $Q$ -enhancement techniques for on-chip inductors, such as the patterned ground plane [85] and the deep trenched p-Si substrate, cannot be applied to the interior of fully-on-chip neural interfacing devices. For these reasons, the WPT with on-chip coils in fully-integrated neural implants has not achieved comparable PTE to conventional WPT techniques utilizing PCB [86, 87], wire-wound [88–90], or ferrite core coils [91].

This chapter presents guidelines for design and optimization of on-chip WPT coils to overcome and alleviate the challenges described above with reporting the results of an on-chip coil optimized for a 100  $\mu\text{W}$  neural interfacing system depicted in Fig.5.1.

## 5.1 On-chip Coil Optimization

### 5.1.1 Model parameters

Power transfer efficiency of an inductive link illustrated in Fig 5.3 is given by:

$$\begin{aligned} PTE &= \frac{k^2 Q_{TX} Q_{RX,loaded}}{1 + k^2 Q_{TX} Q_{RX,loaded}} \frac{R_{P,RX}}{R_L + R_{P,RX}} \\ &= \frac{K_{coupling} \eta_{RX}}{1 + K_{coupling} \eta_{RX}} \eta_{load} \end{aligned} \quad (5.1)$$

where  $Q_{TX} = \omega L_{TX} / R_{TX}$ ,  $Q_{RX} = \omega L_{RX} / R_{RX}$ ,  $Q_{RX,loaded} = \eta_{RX} Q_{RX}$ ,  $K_{coupling} = k^2 Q_{TX} Q_{RX}$ ,  $\eta_{RX} = R_L / (R_L + R_{P,RX})$ ,  $\eta_{load} = R_{P,RX} / (R_L + R_{P,RX})$  and  $R_{P,RX}$  is the effective parallel resistance of the RX coil ( $R_{RX}(Q_{RX}^2 + 1)$ ), assuming capacitors are used to resonate both the transmitter (TX) and receiver (RX) coils [86].

Here,  $K_{coupling}$  is largely dominated by the TX and RX coil design and their physical separation, which is difficult to optimize on the RX side under anatomical constraints. Instead, optimizing on-chip coils for mm-scale neural implants is typically an exercise in maximizing  $\eta_{RX} \times \eta_{load}$ , both of which depend on the load impedance. To

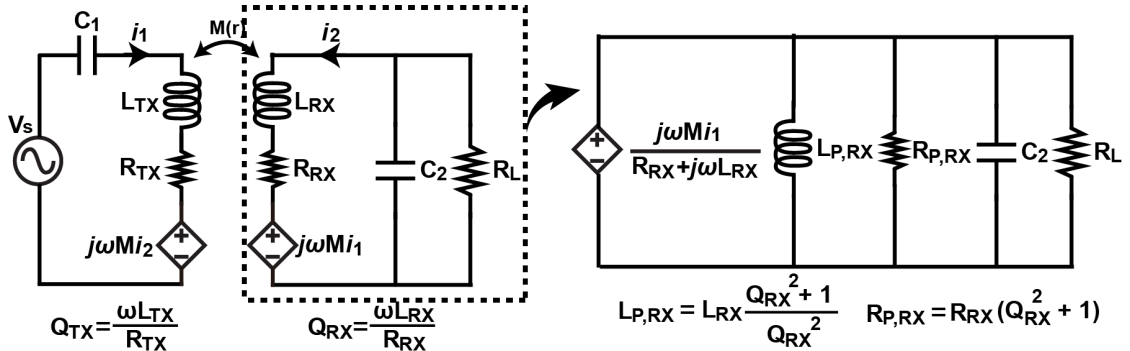
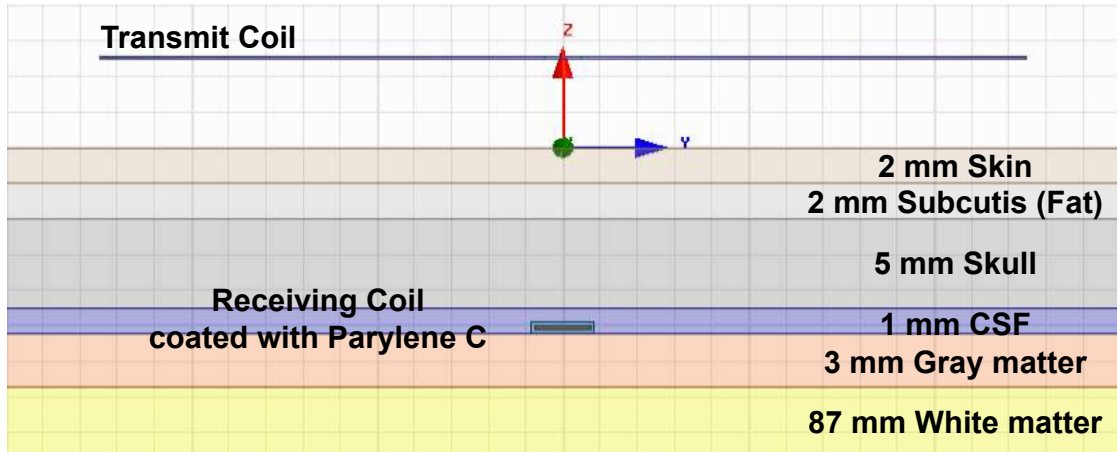
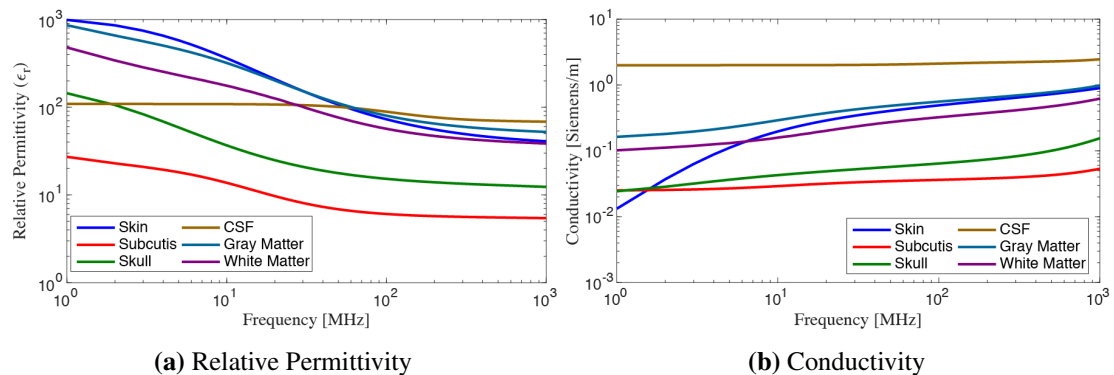


Figure 5.3: Equivalent circuit model of inductive power transfer systems.



**Figure 5.4:** Cross section of the employed FEM simulation model.



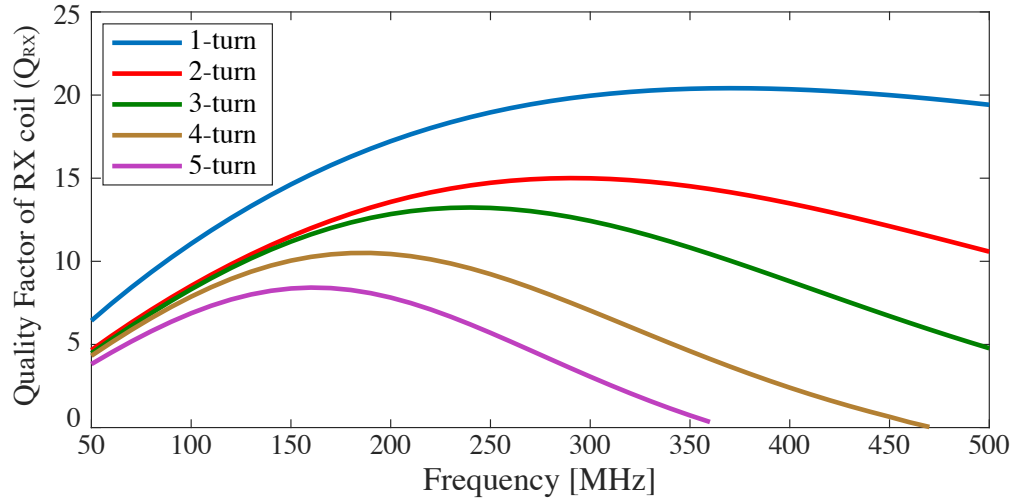
**Figure 5.5:** Frequency-dependent dielectric properties of tissues for the proposed FEM model.

illustrate the proposed design procedure, in this work, a  $100 \mu\text{W}$  load is considered in a total chip area of  $3 \times 3 \text{ mm}^2$  with  $2.4 \times 2.4 \text{ mm}^2$  of area available for inner active circuitry (Fig. 5.1).

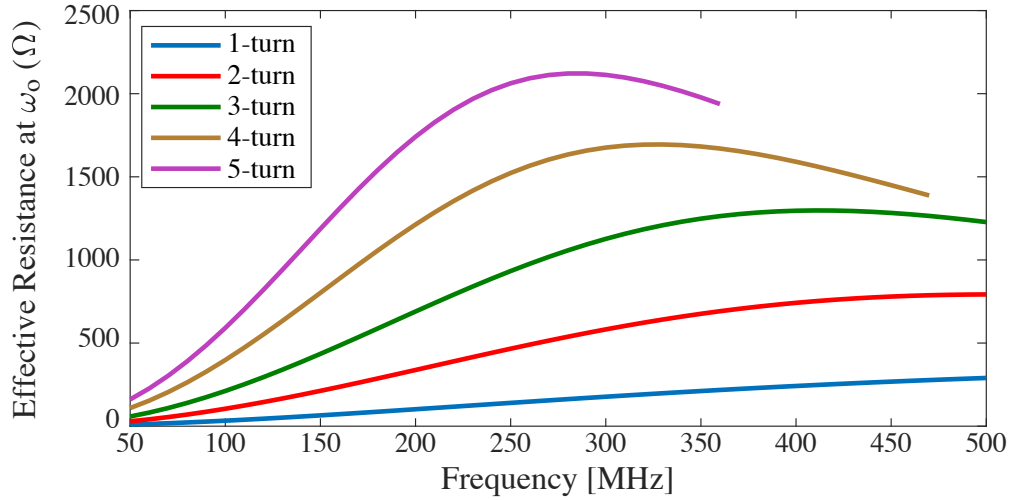
In this work, optimization is performed based on 3D Finite Element Method (FEM) simulations using Ansys HFSS v15. Figure 5.4 shows a cross section of the employed  $10 \times 10 \times 10 \text{ cm}^3$  model, consisting of 2 mm of skin, 2 mm of subcutis (fat), 5 mm of bone, 1 mm of CSF that models the subarachnoid space, 3 mm of gray matter, and 87 mm of white matter. All of the tissue layers include frequency-dependent dielectric properties as shown in Fig. 5.5 from [27]. The RX chip is placed on gray matter (10 mm implant depth) and covered with  $200 \mu\text{m}$  of Parylene C, while the TX is positioned above tissue with various air gap distances (1 to 10 mm).

## 5.1.2 Optimizing the number of turns

Figure 5.6a depicts the simulated  $Q_{RX}$  of on-chip coils with the varying number of turns in the same layout area, and with a 1:1 width-to-space ratio. Here, fewer turns results in higher  $Q_{RX}$ . This matches intuition, as resistance increases quadratically with trace length and width, while inductance increases only linearly in the same layout area. This analysis concludes that a single turn coil offers the largest possible  $K_{coupling}$ .

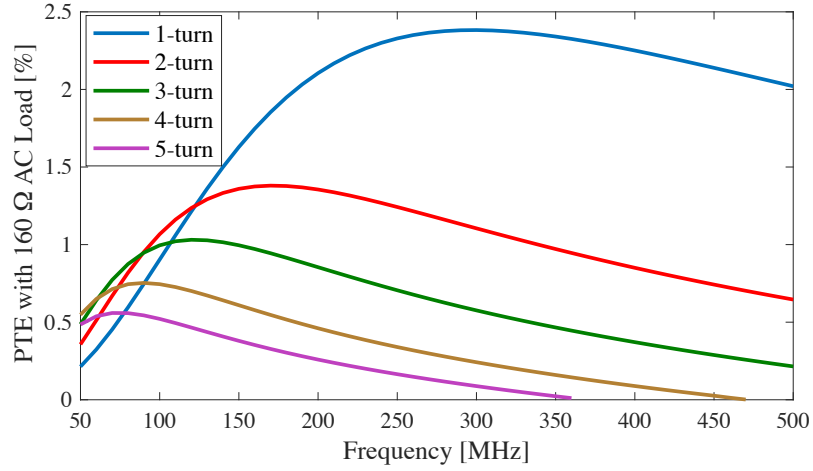


(a)

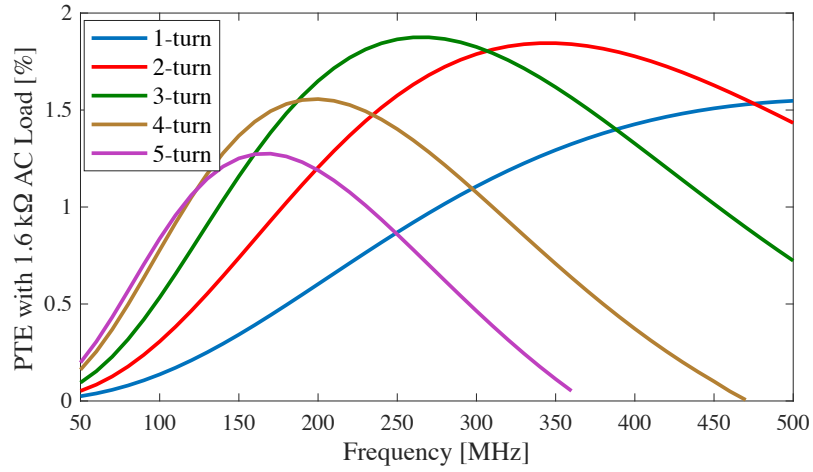


(b)

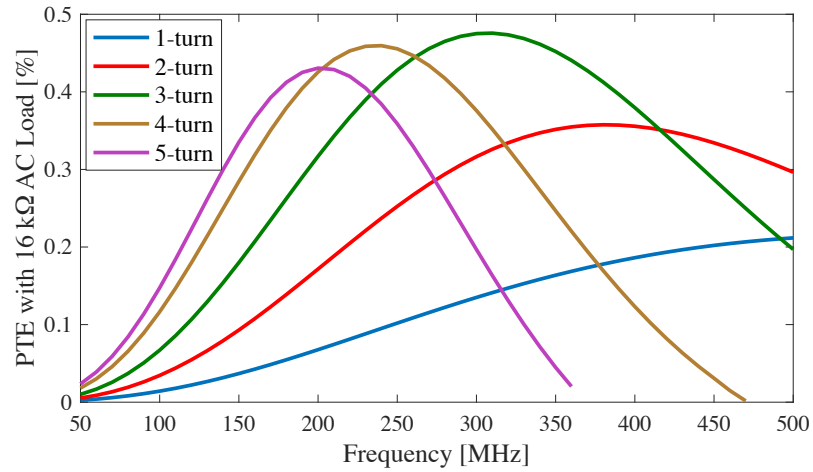
**Figure 5.6:** (a) Quality factor ( $Q_{RX}$ ), and (b) effective resistance ( $R_{P,RX}$ ) at resonance for various turn-number configurations.



(a)



(b)



(c)

**Figure 5.7:** Power transfer efficiency for  $k=0.005$ , and  $Q_{TX}=250$  for AC loads of (a) 0.16 kΩ, (b) 1.6 kΩ, and (c) 16 kΩ.

However, PTE is not determined solely by  $K_{coupling}$ ;  $\eta_{RX}$  and  $\eta_{load}$  are also important, and depend on both the load impedance and  $R_{P,RX}$ . As illustrated in Fig.5.6b,  $R_{P,RX}$  increases with the number of turns due to increased  $R_{RX}$ . In contrast to optimizing  $K_{coupling}$ , a larger number of turns is desired to achieve a high  $R_{P,RX}$  in order to better match to the impedance of a low-power load. These competing trade-offs equalize for various frequencies and load conditions, resulting in an optimal number of turns for maximum PTE.

Figure 5.7 illustrates this for  $k = 0.005$  and  $Q_{TX} = 250$ , assuming AC loads of 0.16, 1.6, and 16 k $\Omega$  that model 1,000, 100, and 10  $\mu$ W 0.8 V DC loads, given a rectifier with 50 % power conversion efficiency (PCE) and 100 % voltage conversion efficiency (VCE) [92]:

$$R_{AC.load} = \frac{1}{2} \frac{PCE}{VCE^2} R_{DC.load} = \frac{1}{2} \frac{PCE}{VCE^2} \frac{V_{DC.load}^2}{P_{DC.load}}. \quad (5.2)$$

This analysis shows a 3-turn coil is optimal for a 100  $\mu$ W neural implant with other specifications described above.

### 5.1.3 Optimizing trace width/spacing

The next step for RX coil design is to size the coil wire width and spacing. Wider trace widths achieve lower resistance but reduce the spacing between turns in a fixed area. Proximity effects between turns result in not only additional effective resistance but also increased parasitic capacitance that reduces SRF, both of which ultimately serve to degrade  $Q_{RX}$ . Unlike when optimizing for the number of turns, it is appropriate to try to maximize  $Q_{RX}$  when optimizing coil trace/space specifications, as at large load resistances,  $\eta_{RX}$  and  $\eta_{load}$  are not strongly affected by coil trace size. To select optimal trace width and spacing, a parametric sweep was performed in HFSS with 5  $\mu$ m trace width steps from 60 to 90  $\mu$ m for a fixed total coil width (280  $\mu$ m). Representative results from this parametric sweep are shown in Fig. 5.8. Here, HFSS simulation results suggest an optimal ratio of 30:11 (75  $\mu$ m : 27.5  $\mu$ m for  $Q = 14$  at 200 MHz).

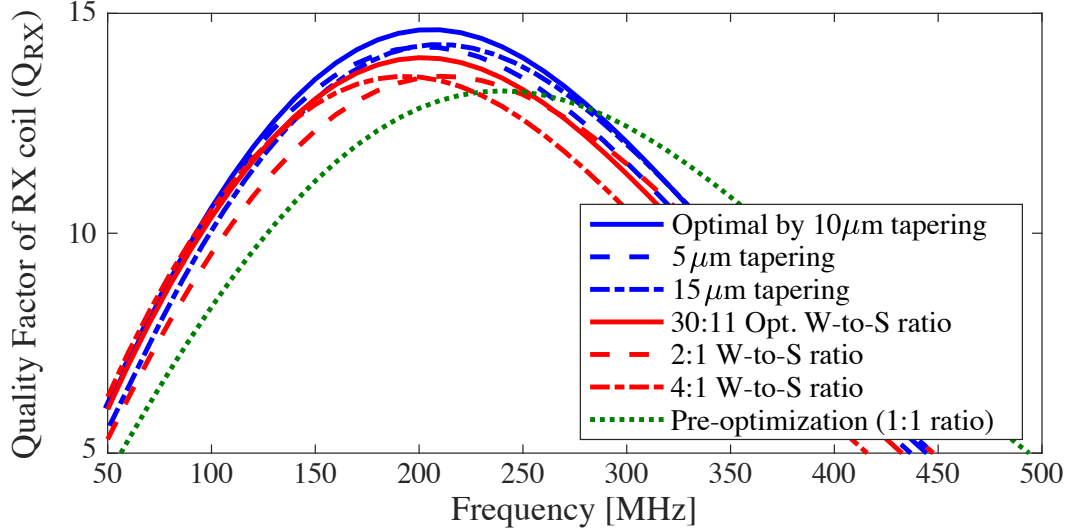


**Figure 5.8:** Optimizing  $Q_{RX}$  through trace width/spacing engineering.

Interestingly, a tapered sizing approach where outer turns are wider than inner turns can further improve  $Q$  under the same total coil width constraint by minimizing the proximity effect and p-Si substrate losses. To find the optimal tapering rate, a further parametric sweep was performed in HFSS by increasing the outer-turn trace with  $1 \mu\text{m}$  steps from  $80$  to  $90 \mu\text{m}$ , while decreasing the inner trace width by the same amount and maintaining the middle trace width and relative spacing. Simulation results reveal an improved  $Q$  of  $14.6$  for a  $10 \mu\text{m}$  tapering rate with  $27.5 \mu\text{m}$  spacing. Figure 5.8 illustrates  $Q$  of the optimized on-chip coil in comparison to the 1:1 width-to-space 3-turn coil.

## 5.1.4 Internal Circuit Routing Considerations

In fully-on-chip neural implants, the RX coil is typically positioned along the perimeter of the chip to maximize its area and inductance. However, unlike conventional inductors in RFICs, the inner area of the RX coil in fully-on-chip neural implants is filled with active circuitry, electrodes, metalization, etc. [93]. The presence of conductors within the inner area of the coil can potentially adversely affect  $Q_{RX}$  (and potentially interfere with sensitive internal analog circuits). Figure 5.9 shows simulated

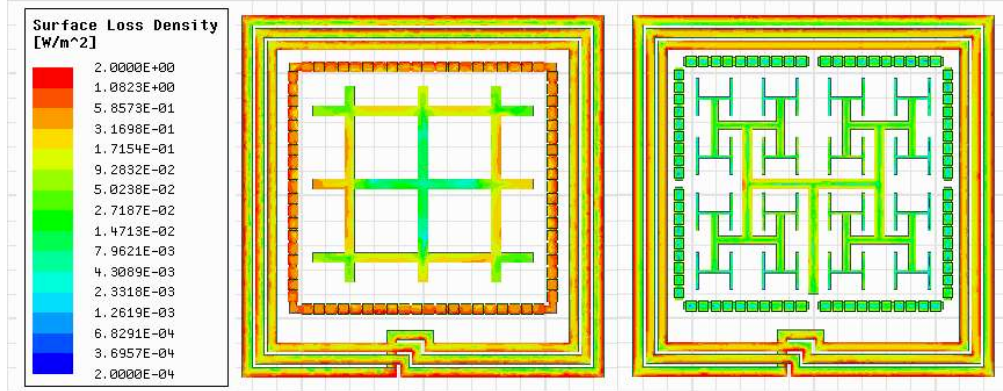


**Figure 5.9:** The loss density on metal surfaces indicating the amount of receiving power from a 1 W transmitting coil and neighboring traces

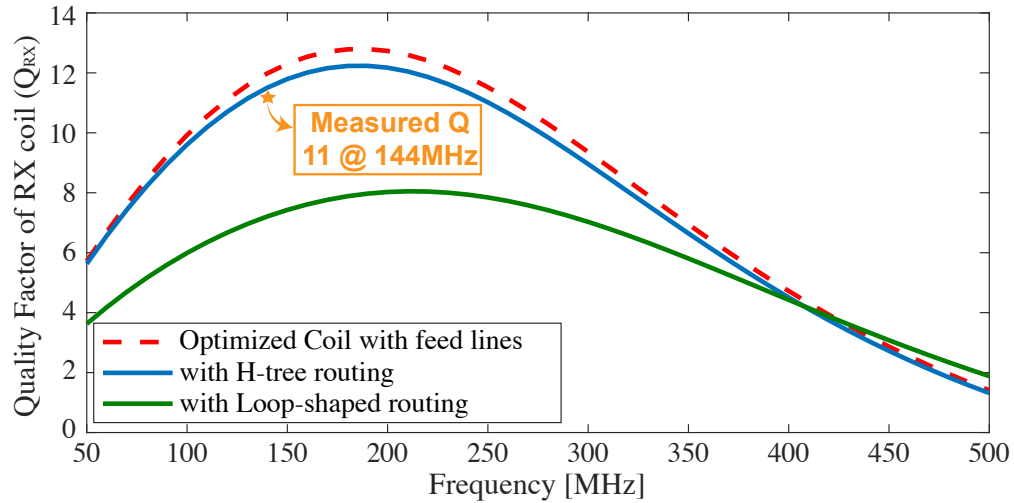


**Figure 5.10:** The  $Q$  degradation by inner routing and its measured value of the fabricated IC implementing the H-tree routing scheme

power loss densities of two representative chip implementations with a conventional grid-based internal power distribution and routing scheme (left) and a fractal H-tree-based routing scheme (right). As shown, grid-based routing schemes introduce additional on-chip eddy current loops that cause significant additional losses. Figure 5.10 shows how  $Q_{RX}$  is degraded from a maximum of 12.8 with no internal routing (including feed line losses), to 8.0 under grid-based routing. To minimize the degradation of  $Q_{RX}$ , it is recommended to design on-chip power distribution and routing networks to follow a fractal geometry, to minimize the number of eddy current loops. Simulation

results from an H-tree implementation are also shown in Fig. 5.10, illustrating minimal degradation of  $Q_{RX}$ . Measurement results at 144 MHz, chosen not because it is optimal for the RX coil's  $Q$ , but rather due to characteristics of the TX coil, reveal a  $Q_{RX}$  of 11, validating simulations at that frequency.

## 5.2 Transmit Coil Optimization

To maximize PTE, the TX coil should be designed to maximize  $k^2 Q_{TX}$  at the frequency where the RX coil was optimized. At the frequencies where mm-scale RX coils are optimal ( $\sim 100$ s of MHz), a single-turn TX coil offers superior  $Q_{TX}$  compared to multi-turn coils (due to higher SRF), and is thus employed in the following analysis with regards to the trace width and the inner dimension, assuming 1 oz ( $35 \mu\text{m}$  thickness) copper on a 0.6 mm thick FR4 PCB substrate.

Generally,  $k$  increases with both frequency and TX coil size as shown in Fig. 5.11, until the SRF or for a radius  $\sqrt{2}$  larger than the TX-RX coil separation distance, respectively. However, too large of a coil size decreases  $Q_{TX}$  at the optimal RX coil frequency as depicted in Fig. 5.12. Figure 5.13 illustrates the effects of this trade-off

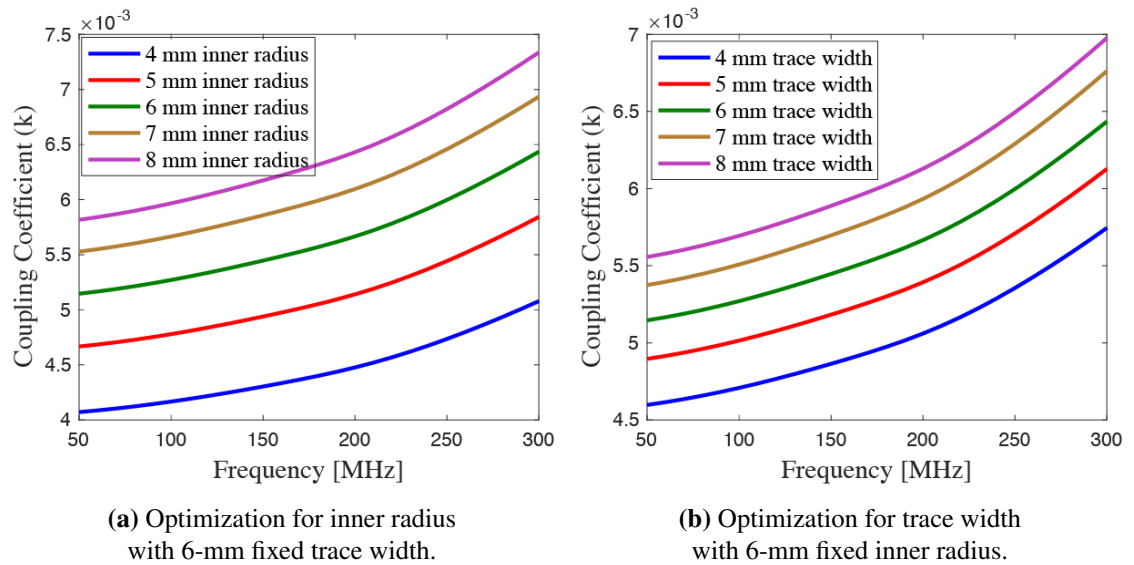


**Figure 5.11:** Single-turn TX coil optimization for coupling coefficient ( $k$ ).

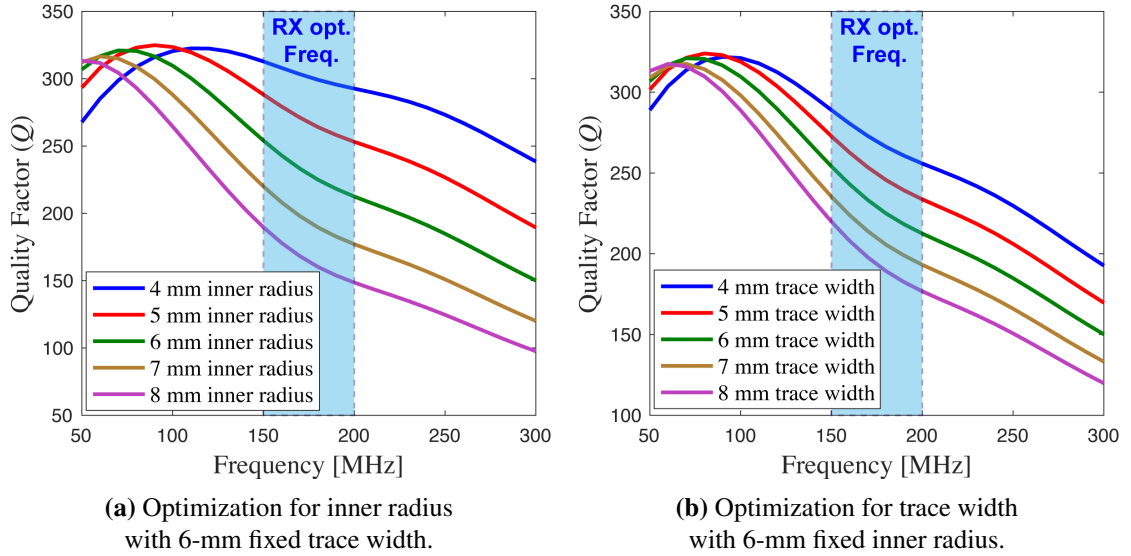


**Figure 5.12:** Single-turn TX coil optimization for quality factor ( $Q_{TX}$ ) at the RX optimal frequency.

vis-a-vis PTE, showing an optimal PTE of 2.1 % for a 6 mm inner radius and 6 mm trace width at 185 MHz. Here, the proposed octagon-shaped TX coil realizes up to 10.5 % PTE improvement over a circular coil that has 1.9 % optimal PTE as shown in Fig 5.14.

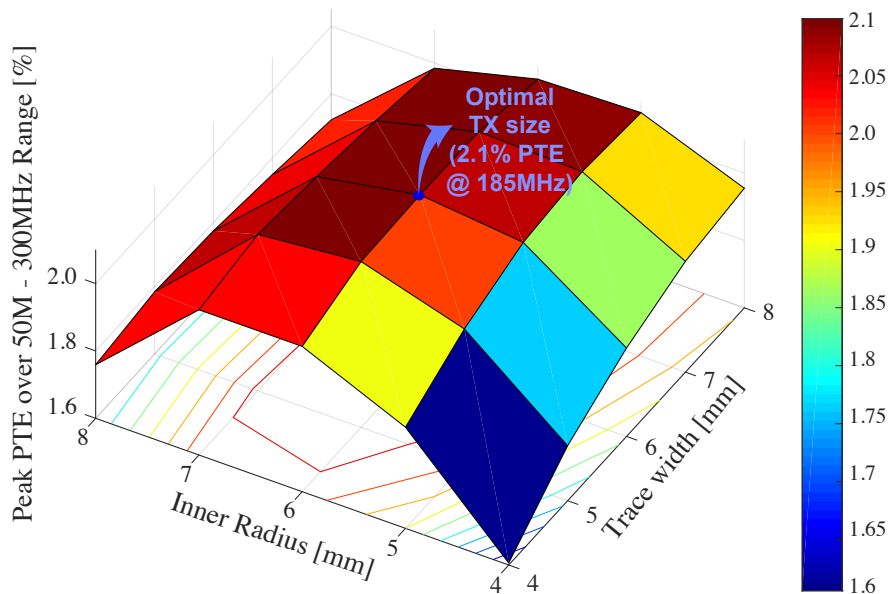


**Figure 5.13:** Transmit coil optimization for 1 oz copper ( $35 \mu\text{m}$  thickness) on a PCB, for 15 mm coupling distance (5 mm of air and 10 mm of tissue).

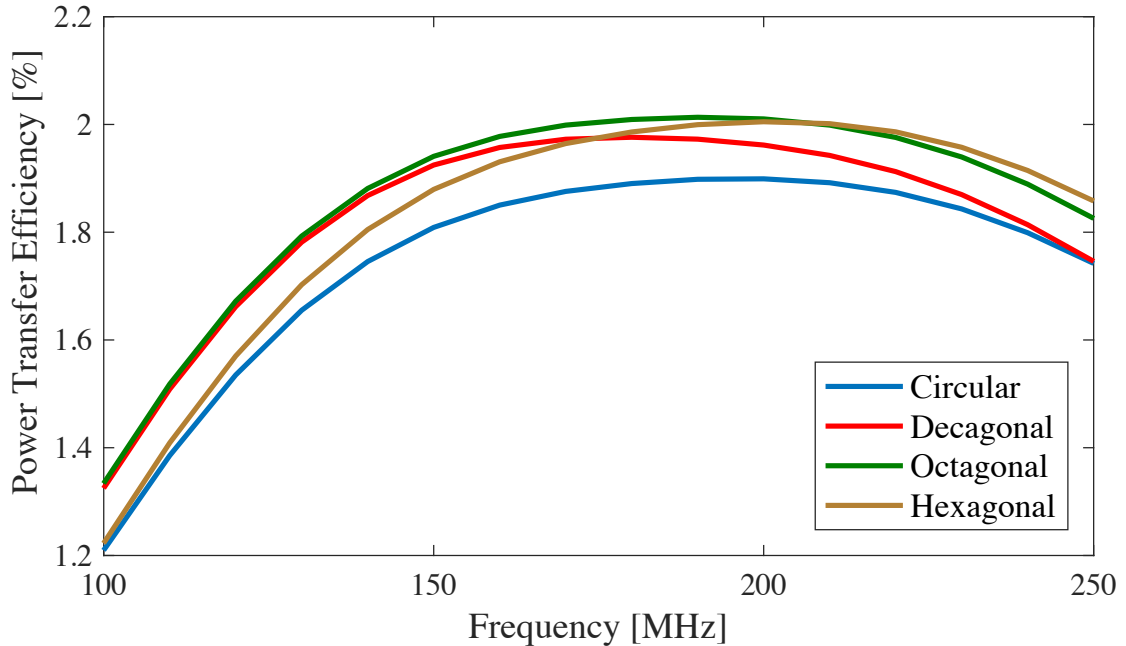


**Figure 5.14:** TX shape optimization.

In high power applications that flirt with specific absorption rate (SAR) limits, it may be beneficial to not necessarily optimize for maximum PTE, but instead for maximum delivered power to the RX under SAR limits. For example, the TX coil described above can transmit more power under SAR limits at lower frequencies, where PTE is deteriorated. As shown in Fig. 5.15a, an optimal frequency of 144 MHz balances SAR-limited TX power with PTE to maximize power delivered to the RX load. Interestingly, placing the TX coil away from the skin increases TX power under SAR limits as depicted in Fig. 5.15b, yet does so with decreased PTE. In this example, the power delivered to the RX load is maximized for an air separation distance of 5 mm. At an RX load power of  $100 \mu\text{W}$ , it is better to optimize for maximum PTE, as SAR limits are not reached. However, if the implant enters a constant stimulation mode, where power can be as high ( $\sim\text{mW}$  level) [94], the SAR-informed optimizations described above may be appropriate. Assuming a peak power as high as 6 mW, a 144 MHz frequency was selected in this work.

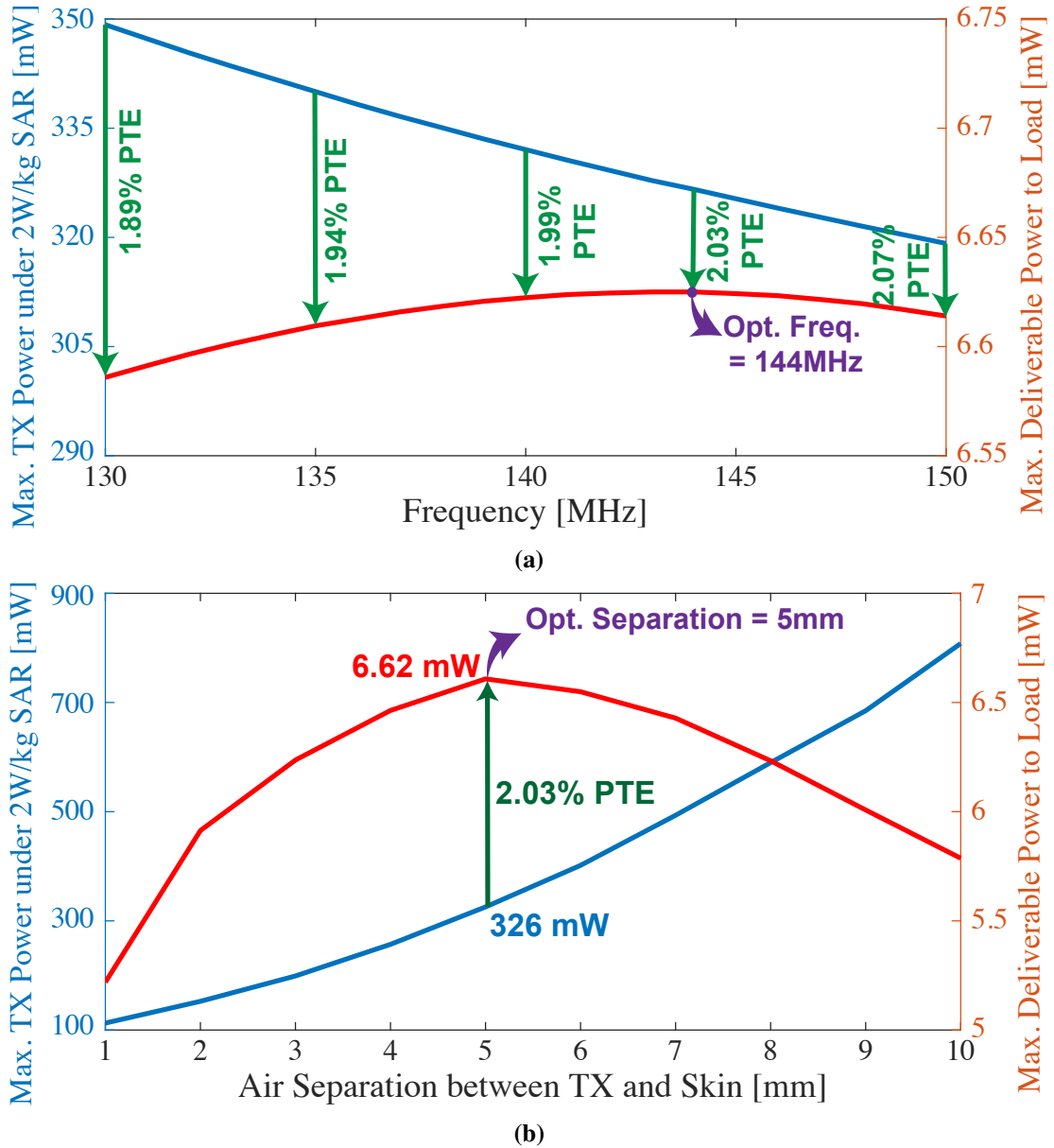
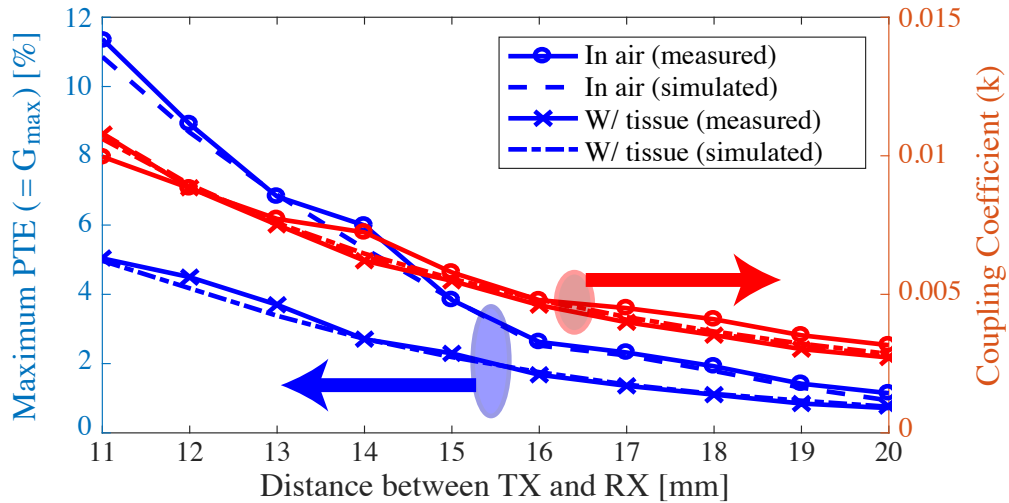


**Figure 5.15:** (a) Operating frequency selection with 5 mm air gap and (b) optimal air separation from tissue when considering SAR at 144 MHz.

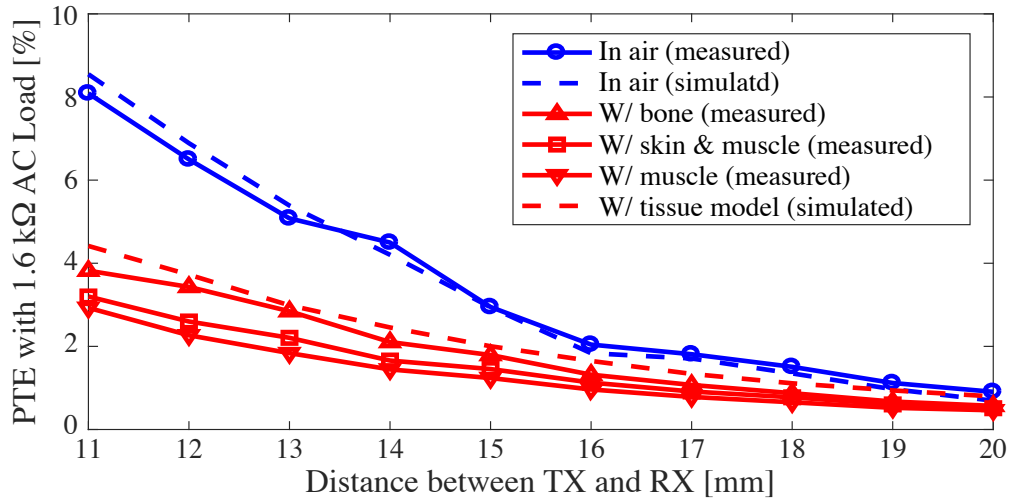
## 5.3 Measurement Results

In order to validate the described optimization methodology, a  $3 \times 3$  mm<sup>2</sup> fully-on-chip neural interfacing device and a 24 mm octagonal TX coil were fabricated with the coil specifications described in the preceding section. WPT measurements were

taken with a Keysight E5071C vector network analyzer. To ensure accurate PTE measurements, extensive calibrations and port extensions were performed to de-embed the effects of all SMA connectors and feed lines, and all measurements were repeated 20 times and averaged. Unlike conventional WPT systems, which often estimate important quantities such as  $k$  by removing the tuning capacitor and measuring Z-parameters [89,90], it is difficult to remove on-chip tuning capacitors used in mm-scale neural implants, and thus an alternative analytical technique is required.



(a)



(b)

**Figure 5.16:** (a) Maximum PTE under optimal load conditions, along with estimated  $k$ . (b) Measured and simulated PTE with a 1.6 k $\Omega$  AC load in air and galline tissue.

The maximum PTE with an optimal load,  $PTE_{max.opt.load}$ , is defined approximately as  $k^2 Q_{TX} Q_{RX} / 4$  when  $K_{coupling}$  is smaller than 1. This is exactly the same as the definition of maximum available gain ( $G_{max}$ ), and thus  $k$  can be estimated by measuring  $Q_{TX}$ ,  $Q_{RX}$ , and  $G_{max}$  derived from the following equation:

$$G_{max} = \frac{|S_{21}|}{|S_{12}|} (S - \sqrt{S^2 - 1}), \quad (5.3)$$

where  $S$  is the stability factor derived from  $S$ -parameters. Figure 5.16a shows the measured  $PTE_{max.opt.load}$  and  $k$  results acquired via measured and converted  $S$ -parameters both in air and across 10 mm of galline tissue (with the rest of the coil separation distance occurring in air). Coil  $Q$ s were measured separately, revealing  $Q_{TX} = 416.8$  and  $Q_{RX} = 11$  at 144 MHz in air. Since  $Q_{TX}$  is severely degraded in the presence of biological tissue,  $Q_{TX}$  was measured at every data point in order to estimate  $k$ . Simulated  $PTE_{max.opt.load}$  based on the models described above agree with all shown measurements to within 0.6 %.

While Fig. 5.16a shows the maximum PTE given an ideal load, Fig. 5.16b shows measured PTE for a more realistic fixed 1.6 k $\Omega$  AC load. Here, the WPT achieved 3.82 %, 3.2 %, and 2.93 % PTE at 11 mm WPT channel distance (1 mm air gap, and 10 mm of either galline chest bone or muscle tissue with and without skin). Simulations with the brain implant model described in Fig. 5.4 achieves 4.25 %. For reference, the WPT link achieved 8.1 % measured PTE and 8.6 % simulated PTE across 11 mm in air, matching to within 0.5 %.

Table 5.1 summarizes the results of this work while contrasting to other recent work on mm-scale implantable coils. As a result of the proposed optimization procedure, the designed on-chip coil WPT link achieved higher PTE than previously-reported on-chip WPT solutions, while achieving comparable PTE to mm-scale wirewound coils.

**Table 5.1:** Table of Comparisons to Recent mm-Scale WPT Links for Implants under In-vitro Conditions

Parameters		This work	[82]	[89]	[90]
TX	Type	Oct. PCB	Square PCB	Hex. PCB	Cir. PCB
	Diameter [mm]	24	20.5	24	28
	No. of turns	1	2	1	5
RX	Type	On-chip	On-chip	Wirewound	Wirewound
	Volume [mm <sup>3</sup> ]	0.036 (3×3×0.004)	0.048 (2×2.18×0.011)	0.785 ( $\pi \times 0.5^2 \times 1$ )	0.785 ( $\pi \times 0.5^2 \times 1$ )
	No. of turns	3	4	7	7
TX-to-RX distance [mm]		11 <sup>†</sup> \ 15 <sup>‡</sup>	10	12	12
Tissue thickness [mm]		10	7.5	10	10
Frequency [MHz]		144	160	200	20
AC load [k $\Omega$ ]		1.6	Optimal	5	0.25
PTE [%]		3.82* \ 1.83	0.8	0.56	1.4
Max. Del. Power (2W/kg SAR) [mW]		5.22 <sup>◊</sup> \ 6.62 <sup>◊</sup>	0.8 <sup>◊</sup>	0.275 <sup>◊</sup>	2.75 <sup>◊</sup>

Note : <sup>†</sup> for the maximum PTE and <sup>‡</sup> for the maximum delivered power under 2 W/kg SAR

\* 5.04 % with optimal load. <sup>◊</sup> based on HFSS SAR simulation. <sup>◊</sup> converted from 1.6 W/kg SAR.

## 5.4 Conclusion

This chapter has shown the optimization methods for on-chip WPT coils via FEM simulation, validating with the in-vitro experiments. With the restricted Q of on-chip inductors under IC fabrication, these optimizing steps enable to achieve 3.82 % PTE with 1.6 k $\Omega$  AC load modeled for 100  $\mu$ W  $3 \times 3$  mm<sup>2</sup> neural implants when the implant depth is 10 mm with 1 mm air separation. Since the optimized PTE ensures the plenty of delivered power on an energy-efficient neural implant, the on-chip WPT is expected to create the next generation of neural implants, alleviating the problems by external components.

Chapter Five is largely a reprint of material as it appears to "Wireless powering of mm-Scale Fully-on-Chip Neural Interfaces," by Jiwoong Park, Chul Kim, Abraham Akinin, Sohmyung Ha, Gert Cauwenberghs, and Patrick P. Mercier in IEEE Biomedical Circuits and Systems Conference (BioCAS), October 2017. The dissertation author is the primary investigator and author of this work.

# Appendix A

## Derivation of Field Pattern and Complex Power Density

Given an ideal current loop ( $I = I_o e^{j\omega t}$ ) which has a radius of  $a$  as shown in Fig. A.1a, the vector potential can be derived as below:

$$\begin{aligned}
 \vec{A} &= \hat{\phi} \frac{\mu I_o a}{4\pi} \int_0^{2\pi} \cos\phi' \frac{e^{-j(k\sqrt{r^2+a^2-2ar\sin\theta\cos\phi'}-\omega t)}}{\sqrt{r^2+a^2-2ar\sin\theta\cos\phi'}} d\phi' \\
 &\approx \hat{\phi} \frac{\mu I_o a}{4\pi} \int_0^{2\pi} \cos\phi' \left[ \frac{1}{r} + a \left( j\frac{k}{r} + \frac{1}{r^2} \right) \sin\theta \cos\phi' \right] e^{-j(kr-\omega t)} d\phi' \quad (\text{for } r > a) \\
 &= \hat{\phi} \frac{\mu k I_o a^2}{4} \left( j + \frac{1}{kr} \right) \sin\theta e^{-j(kr-\omega t)}
 \end{aligned} \tag{A.1}$$

With derived vector potential by an ideal current loop, the E and H field pattern and Poynting vector can be derived as shown below:

$$\begin{aligned}
 \vec{H} &= \frac{1}{\mu} \nabla \times \vec{A} = \frac{1}{\mu} \left[ \hat{r} \frac{1}{r \sin\theta} \frac{\partial}{\partial \theta} (\sin\theta |\vec{A}|) - \hat{\theta} \frac{1}{r} \frac{\partial}{\partial r} (\sin\theta |\vec{A}|) \right] \\
 &= -\frac{k^3 I_o a^2}{4} \left\{ \hat{r} \left[ \frac{1}{j(kr)^2} - \frac{1}{(kr)^3} \right] 2 \cos\theta + \hat{\theta} \left[ \frac{1}{kr} + \frac{1}{j(kr)^2} - \frac{1}{(kr)^3} \right] \sin\theta \right\} e^{-j(kr-\omega t)}
 \end{aligned} \tag{A.2}$$

$$\vec{E} = \frac{1}{j\omega\epsilon} \nabla \times \vec{H} = \hat{\phi} \frac{\eta k^3 I_o a^2}{4} \left[ \frac{1}{kr} + \frac{1}{j(kr)^2} \right] \sin\theta e^{-j(kr-\omega t)} \tag{A.3}$$

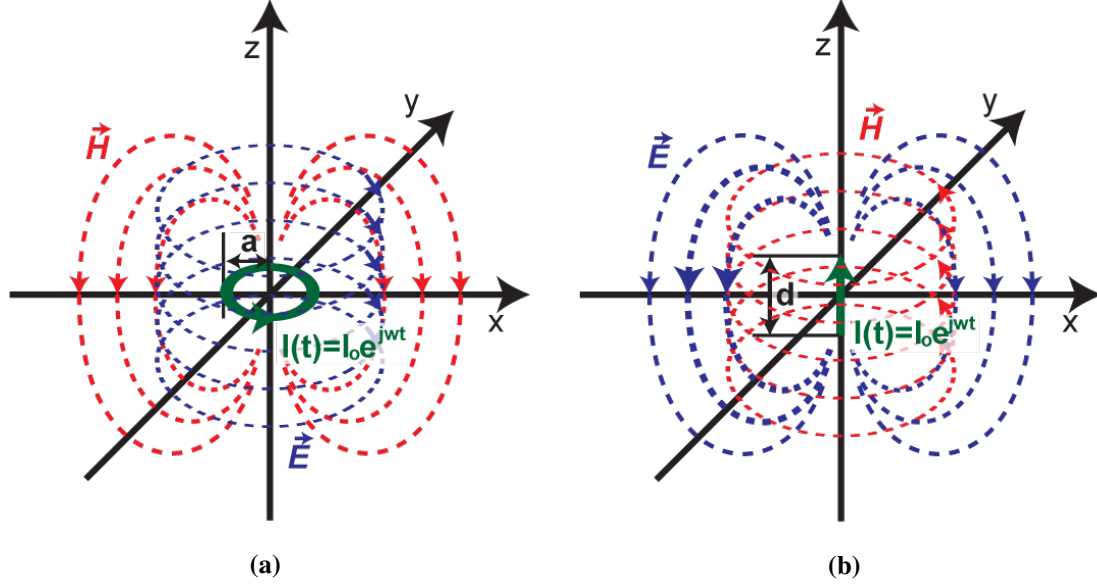


**Figure A.1:** (a) An ideal magnetic dipole and its near-field pattern and (b) a Hertzian electric dipole and its near-field pattern

$$\vec{W} = \frac{1}{2} \vec{E} \times \vec{H}^* = \frac{\eta k^6 I_o^2 a^4}{32} \hat{r} \left[ \frac{1}{(kr)^2} + j \frac{1}{(kr)^5} \right] \sin^2 \theta - \hat{\theta} \left[ j \frac{1}{(kr)^3} + j \frac{1}{(kr)^5} \right] \sin 2\theta \quad (\text{A.4})$$

Where  $k = \sqrt{\epsilon_r} k_o$ ,  $\eta = \eta_o / \sqrt{\epsilon_r}$  with a dielectric medium which has the relative permittivity of  $\epsilon_r$ ,

$$\vec{H} = -\frac{k_o^3 I_o a^2}{4} \left\{ \hat{r} \left[ \frac{\sqrt{\epsilon_r}}{j(k_o r)^2} - \frac{1}{(k_o r)^3} \right] 2 \cos \theta + \hat{\theta} \left[ \frac{\epsilon_r}{k_o r} + \frac{\sqrt{\epsilon_r}}{j(k_o r)^2} - \frac{1}{(k_o r)^3} \right] \sin \theta \right\} e^{-j(kr - \omega t)} \quad (\text{A.5})$$

$$\vec{E} = \hat{\phi} \frac{\eta_o k_o^3 I_o a^2}{4} \left[ \frac{\sqrt{\epsilon_r}}{k_o r} + \frac{1}{j(k_o r)^2} \right] \sin \theta e^{-j(kr - \omega t)} \quad (\text{A.6})$$

$$\vec{W} = \frac{\eta_o k_o^6 I_o^2 a^4}{32} \hat{r} \left[ \frac{\sqrt{\epsilon_r^3}}{(k_o r)^2} + j \frac{1}{(k_o r)^5} \right] \sin^2 \theta - \hat{\theta} \left[ j \frac{\epsilon_r}{(k_o r)^3} + j \frac{1}{(k_o r)^5} \right] \sin 2\theta \quad (\text{A.7})$$

In a similar manner, the vector potential, field pattern, and Poynting vector of an electric dipole which has a length of  $d$  as shown in Fig. A.1b can be derived as:

$$\vec{A} = \frac{\mu I_o d}{4\pi r} (\hat{r} \cos\theta - \hat{\theta} \sin\theta) e^{-j(kr - \omega t)} \quad (\text{A.8})$$

$$\vec{H} = \hat{\phi} \frac{j k_o^2 I_o d}{4\pi} \left[ \frac{\sqrt{\epsilon_r}}{k_o r} + \frac{1}{j(k_o r)^2} \right] \sin\theta e^{-j(kr - \omega t)} \quad (\text{A.9})$$

$$\begin{aligned} \vec{E} = \frac{j \eta_o k_o^2 I_o d}{4\pi} \left\{ \hat{r} \left[ \frac{1}{j \sqrt{\epsilon_r} (k_o r)^2} - \frac{1}{\epsilon_r (k_o r)^3} \right] 2 \cos\theta \right. \\ \left. + \hat{\theta} \left[ \frac{1}{k_o r} + \frac{1}{j \sqrt{\epsilon_r} (k_o r)^2} - \frac{1}{\epsilon_r (k_o r)^3} \right] \sin\theta \right\} e^{-j(kr - \omega t)} \end{aligned} \quad (\text{A.10})$$

$$\vec{W} = \frac{\eta_o k_o^4 I_o^2 d^2}{32\pi^2} \hat{r} \left[ \frac{\sqrt{\epsilon_r}}{(k_o r)^2} - j \frac{1}{\epsilon_r (k_o r)^5} \right] \sin^2\theta + \hat{\theta} \left[ j \frac{1}{(k_o r)^3} + j \frac{1}{\epsilon_r (k_o r)^5} \right] \sin 2\theta \quad (\text{A.11})$$

While degrading the E-field generated by an electric dipole as shown in Eqn. [A.10], a high dielectric material (e.g., biological tissues at lower frequency) enhances the H-field by a current loop as described in Eqn. [A.5], which results in better inductive coupling between the magnetic sources (e.g., mHBC coils), unlike poor capacitive coupling of eHBC or RF under a high dielectric medium like seawater as reported in [50,51]

# Appendix B

## Derivation of the Magnetic Flux Density inside the Human Body

When there is no boundary on the propagation path of a far-field EM wave (i.e., in free space), the averaged magnetic flux density ( $B_{far,avg}$ ) passing through the RX coil placed at  $z = Z$  can be derived as:

$$\begin{aligned} B_{far,avg,air}(Z) &= \frac{\Phi_{21}(Z)}{A_2} = \frac{1}{A_2} \int_{A_2} \mu_o H_{far}(r) dA \\ &= \frac{1}{\pi a^2} \int_0^{2\pi} \int_0^a \frac{\mu_o k_o^2 I_o a^2}{4r} \sin\theta da' d\phi \\ &= \frac{\mu_o k_o^2 I_o}{2} \int_0^a \frac{\sin\theta}{\sqrt{Z^2 + a'^2}} da' = \frac{\mu_o k_o^2 I_o}{2} \int_0^a \frac{a'}{Z^2 + a'^2} da' \\ &= \frac{\mu_o k_o^2 I_o}{4} \ln\left(1 + \frac{a^2}{Z^2}\right) \end{aligned} \tag{B.1}$$

However, the existence of high dielectric in air yields a boundary condition that keeps the far-field wave energy inside the dielectric material by total internal reflection as shown in Fig. 3.4, which can be modeled as an effectively enlarged dimension ( $a^*$ ) of the receptor coil, so long as the orientation of the flux vectors are taken into account. With this modeled wave behavior, the  $B_{far,avg}$  of the RX coil can be derived as follows:

$$\vec{B}_{far,avg}(Z \approx Nb) = \hat{x}B_{x,far,avg}(Z) + \hat{z}B_{z,far,avg}(Z) \tag{B.2}$$

$$\begin{aligned}
(\text{where } B_{x, far, avg}(Z \approx Nb) &= \frac{1}{\pi a^2} \int_0^{2\pi} \int_0^{a^*} \mu_o H_{far}(r) \cos\theta \, da' d\phi \\
&= \frac{\mu_o \epsilon_r k_o^2 I_o}{2} \sum_{m=1}^N D_{xm} \int_{(m-1)a}^{ma} \frac{\sin\theta \cos\theta}{r} \, da' \\
&= \frac{\mu_o \epsilon_r k_o^2 I_o}{2} \sum_{m=1}^N D_{xm} \int_{(m-1)a}^{ma} \frac{Za'}{\sqrt{Z^2 + a'^2}^3} \, da' \\
&= \frac{\mu_o \epsilon_r k_o^2 I_o}{2} \sum_{m=1}^N D_{xm} \left[ \frac{(m-1)aZ}{\sqrt{Z^2 + (m-1)^2 a^2}} - \frac{maZ}{\sqrt{Z^2 + m^2 a^2}} \right]
\end{aligned}$$

$$\begin{aligned}
\text{and } B_{z, far, avg}(Z \approx Nb) &= \frac{1}{\pi a^2} \int_0^{2\pi} \int_0^{a^*} \mu_o H_{far}(r) \sin\theta \, da' d\phi \\
&= \frac{\mu_o \epsilon_r k_o^2 I_o}{2} \left[ \int_0^a \frac{D_{z1} \sin^2\theta}{r} \, da' + \int_a^{2a} \frac{D_{z2} \sin^2\theta}{r} \, da' \right. \\
&\quad \left. + \dots + \int_{(N-1)a}^{Na} \frac{D_{zN} \sin^2\theta}{r} \, da' \right] \\
&= \frac{\mu_o \epsilon_r k_o^2 I_o}{2} \sum_{m=1}^N D_{zm} \int_{(m-1)a}^{ma} \frac{\sin^2\theta}{r} \, da' \\
&= \frac{\mu_o \epsilon_r k_o^2 I_o}{2} \sum_{m=1}^N D_{zm} \int_{(m-1)a}^{ma} \frac{a'^2}{\sqrt{Z^2 + a'^2}^3} \, da' \\
&= \frac{\mu_o \epsilon_r k_o^2 I_o}{2} \sum_{m=1}^N D_{zm} \left\{ \ln \left[ \frac{ma + \sqrt{Z^2 + m^2 a^2}}{(m-1)a + \sqrt{Z^2 + (m-1)^2 a^2}} \right] \right. \\
&\quad \left. - \frac{ma}{\sqrt{Z^2 + m^2 a^2}} + \frac{(m-1)a}{\sqrt{Z^2 + (m-1)^2 a^2}} \right\}
\end{aligned}$$

On the other hand, the mid- and near-field portion is stored in a standing wave rather than being radiated. Since the E and B fields are not coupled with each other in the near field, the boundary condition derived from the far-field radiating wave properties cannot be applied to this standing wave. Therefore, for the analysis of the near-field portion's behavior at the body air interface, it is more suitable to employ the boundary

condition for time-harmonic B field given below:

$$\vec{n} \times \frac{\vec{B}_i}{\mu_o} = \vec{n} \times \frac{\vec{B}_t}{\mu_o} \quad (\text{B.3a})$$

$$\vec{n} \cdot \vec{B}_t - \vec{n} \cdot \vec{B}_i = \vec{J}_s \approx 0 \quad (\text{B.3b})$$

where  $\vec{J}_s$  is the surface current density vector and  $\hat{n}$  is the normal vector of the incident plane. When  $\vec{J}_s$  can be negligible due to tissues' low conductivity ( $\sigma < 0.2$  Siemens/m) at lower frequency, the near-field portion of the B field does not show a discontinuity at the boundary; hence, B can be calculated without the consideration on the boundary condition by the human body as shown below.

$$\begin{aligned} B_{r,mid,avg}(Z) &= \frac{1}{\pi a^2} \int_0^{2\pi} \int_0^a \mu_o H_{r,near1}(r) da' d\phi = j \frac{\mu_o k^3 I_o}{2} \int_0^a \left(\frac{1}{kr}\right)^2 2 \cos\theta da' \\ &= j \sqrt{\epsilon_r} \mu_o k_o I_o \int_0^a \frac{Z}{\sqrt{Z^2 + a'^2}^3} da' = j \sqrt{\epsilon_r} \frac{\mu_o k_o I_o a}{Z \sqrt{Z^2 + a^2}} \end{aligned} \quad (\text{B.4a})$$

$$\begin{aligned} B_{\theta,mid,avg}(Z) &= j \frac{\mu_o k^3 I_o}{2} \int_0^a \left(\frac{1}{kr}\right)^2 \sin\theta da' = j \frac{\sqrt{\epsilon_r} \mu_o k_o I_o}{2} \int_0^a \frac{a'}{\sqrt{Z^2 + a'^2}^3} da' \\ &= j \frac{\sqrt{\epsilon_r} \mu_o k_o I_o}{2} \left( \frac{1}{Z} - \frac{1}{\sqrt{Z^2 + a^2}} \right) \end{aligned} \quad (\text{B.4b})$$

$$\begin{aligned}
B_{x,near,avg}(Z) &= \frac{1}{\pi a^2} \int_0^{2\pi} \int_0^a \mu_o [H_{r,near}(r) \sin\theta + H_{\theta,near}(r) \cos\theta] da' d\phi \\
&= \frac{\mu_o k^3 I_o}{2} \int_0^a \frac{1}{(kr)^3} 3 \sin\theta \cos\theta da' = \frac{\mu_o I_o}{2} \int_0^a \frac{3Za}{\sqrt{Z^2 + a'^2}^5} da' \quad (\text{B.4c}) \\
&= \frac{\mu_o I_o}{2} \left( \frac{1}{Z^2} - \frac{Z}{\sqrt{Z^2 + a^2}^3} \right)
\end{aligned}$$

$$\begin{aligned}
B_{z,near,avg}(Z) &= \frac{1}{\pi a^2} \int_0^{2\pi} \int_0^a \mu_o [H_{r,near}(r) \cos\theta - H_{\theta,near}(r) \sin\theta] da' d\phi \\
&= \frac{\mu_o I_o}{2} \int_0^a \frac{2Z^2 - a'^2}{\sqrt{Z^2 + a'^2}^5} da' = \frac{\mu_o I_o a \sqrt{2Z^2 + a^2}}{2Z^2 \sqrt{Z^2 + a^2}^3} \quad (\text{B.4d})
\end{aligned}$$

Here, since  $B_{near}$  has the same phase as the far-field portion,  $B_{near,avg}$  is split into  $\hat{x}$  and  $\hat{z}$  dimension for the sake of convenience for computing the total averaged  $B$  as derived below:

$$\begin{aligned}
|B_{total,avg}(Z)| &= \{ [B_{z,far}(Z) + B_{z,near2,avg}(Z)]^2 + [B_{x,far}(Z) + B_{x,near2,avg}(Z)]^2 \\
&\quad + |B_{r,near1,avg}(Z)|^2 + |B_{\theta,near1,avg}(Z)|^2 \}^{1/2} \quad (\text{B.5})
\end{aligned}$$

# References

- [1] P. Hall, Y. Nechayev, A. Alomainy, C. Constantinou, C. Parini, M. Kamarudin, T. Salim, D. Hee, R. Dubrovka, A. Owadally, A. Serra, P. Nepa, M. Gallo, and M. Bozzetti, “Antennas and Propagation for On-Body Communication Systems,” *IEEE Antennas and Propagation Magazine*, vol. 49, no. 3, pp. 41–58, Jun. 2007.
- [2] A. V. Vorst, A. Rosen, and Y. Kotsuka, *RF/Microwave Interaction with Biological Tissues*. New York, NY: John Wiley & Sons, Inc., 2006.
- [3] T. G. Zimmerman, “Personal Area Networks (PAN): Near-Field Intra-Body Communication,” Master’s thesis, Massachusetts Institute of Technology, Cambridge, MA, 1995.
- [4] M. Wegmueller, M. Oberle, N. Felber, N. Kuster, and W. Fichtner, “Signal Transmission by Galvanic Coupling Through the Human Body,” *IEEE Transactions on Instrumentation and Measurement*, vol. 59, no. 4, pp. 963–969, apr 2010.
- [5] M. A. Callejon, Naranjo-Hernandez, J. D., Reina-Tosina, and L. M. Roa, “A Comprehensive Study Into Intrabody Communication Measurements,” *IEEE Transactions on Instrumentation and Measurement*, vol. 62, no. 9, pp. 2446–2455, Sep. 2013.
- [6] N. Cho, J. Yoo, S. J. Song, J. Lee, S. Jeon, and H. J. Yoo, “The human body characteristics as a signal transmission medium for intrabody communication,” *IEEE Transactions on Microwave Theory and Techniques*, vol. 55, no. 5, pp. 1080–1085, 2007.
- [7] J. A. Ruiz and S. Shimamoto, “Propagation characteristics of intra-body communications for body area networks,” in *CCNC 2006. 2006 3rd IEEE Consumer Communications and Networking Conference, 2006.*, vol. 1. IEEE, 2006, pp. 509–513.
- [8] Y. Liu, J. Kuang, Z. He, and J. Fang, “Measurement System for Propagation Characteristics of Intra-Body Communication,” in *2010 International Conference on Computational Intelligence and Software Engineering*. IEEE, Sep. 2010, pp. 1–4.

- [9] R. Xu, H. Zhu, and J. Yuan, "Characterization and analysis of intra-body communication channel," in *2009 IEEE Antennas and Propagation Society International Symposium*. IEEE, Jun. 2009, pp. 1–4.
- [10] W. Wang, Z. Nie, F. Guan, T. Leng, and L. Wang, "Experimental Studies on Human Body Communication Characteristics Based Upon Capacitive Coupling," in *2011 International Conference on Body Sensor Networks*. IEEE, May 2011, pp. 180–185.
- [11] v. Lučev, I. Krois, and M. Cifrek, "A capacitive intrabody communication channel from 100 kHz to 100 MHz," in *2011 IEEE International Instrumentation and Measurement Technology Conference*. IEEE, May 2011, pp. 1–4.
- [12] J. Sakai, L.-S. Wu, H.-C. Sun, and Y.-X. Guo, "Balun's effect on the measurement of transmission characteristics for intrabody communication channel," in *2013 IEEE MTT-S International Microwave Workshop Series on RF and Wireless Technologies for Biomedical and Healthcare Applications (IMWS-BIO)*. IEEE, Dec. 2013, pp. 1–3.
- [13] K. Hachisuka, A. Nakata, T. Takeda, Y. Terauchi, K. Shiba, K. Sasaki, H. Hosaka, and K. Ito, "Development and performance analysis of an intra-body communication device," in *TRANSDUCERS '03. 12th International Conference on Solid-State Sensors, Actuators and Microsystems. Digest of Technical Papers (Cat. No.03TH8664)*, vol. 2. IEEE, 2003, pp. 1722–1725.
- [14] Z. Nie, T. Leng, W. Wang, F. Guan, and L. Wang, "Experimental Characterization of human body communication in shield chamber," in *Proceedings of 2012 IEEE-EMBS International Conference on Biomedical and Health Informatics*. IEEE, Jan. 2012, pp. 759–762.
- [15] J. Bae, H. Cho, K. Song, H. Lee, and H.-J. Yoo, "The Signal Transmission Mechanism on the Surface of Human Body for Body Channel Communication," *IEEE Transactions on Microwave Theory and Techniques*, vol. 60, no. 3, pp. 582–593, Mar. 2012.
- [16] Ž. Lučev, I. Krois, M. Cifrek, H. Džapo, and S. Tonković, "Effects of transmitter position and receiver ground plane on signal transmission in intrabody wireless emg measurement system," in *World Congress on Medical Physics and Biomedical Engineering, September 7-12, 2009, Munich, Germany*. Springer, 2009, pp. 887–890.
- [17] Z. Nie, J. Ma, K. Ivanov, and W. Lei, "An Investigation on Dynamic Human Body Communication Channel Characteristics at 45 MHz in Different Surrounding Environments," *IEEE Antennas and Wireless Propagation Letters*, vol. 13, pp. 309–312, 2014.

- [18] Y. Song, Q. Hao, K. Zhang, M. Wang, Y. Chu, and B. Kang, "The Simulation Method of the Galvanic Coupling Intrabody Communication With Different Signal Transmission Paths," *IEEE Transactions on Instrumentation and Measurement*, vol. 60, no. 4, pp. 1257–1266, Apr. 2011.
- [19] M. A. Callejón, J. Reina-Tosina, D. Naranjo-Hernandez, and L. M. Roa, "Measurement Issues in Galvanic Intrabody Communication: Influence of Experimental Setup." *IEEE transactions on bio-medical engineering*, vol. 62, no. 11, pp. 2724–32, Nov. 2015.
- [20] M. A. Callejón, D. Naranjo-Hernández, J. Reina-Tosina, and L. M. Roa, "Distributed circuit modeling of galvanic and capacitive coupling for intrabody communication." *IEEE transactions on bio-medical engineering*, vol. 59, no. 11, pp. 3263–9, Nov. 2012.
- [21] B. Kibret, M. Seyedi, D. T. H. Lai, and M. Faulkner, "Investigation of galvanic-coupled intrabody communication using the human body circuit model." *IEEE journal of biomedical and health informatics*, vol. 18, no. 4, pp. 1196–206, Jul. 2014.
- [22] R. Xu, H. Zhu, and J. Yuan, "Electric-field intrabody communication channel modeling with finite-element method." *IEEE transactions on bio-medical engineering*, vol. 58, no. 3, pp. 705–12, Mar. 2011.
- [23] V. De Santis, P. A. Beeckman, D. A. Lampasi, and M. Feliziani, "Assessment of human body impedance for safety requirements against contact currents for frequencies up to 110 MHz." *IEEE transactions on bio-medical engineering*, vol. 58, no. 2, pp. 390–6, Feb. 2011.
- [24] B. Gustavsen and A. Semlyen, "Rational approximation of frequency domain responses by vector fitting," *IEEE Transactions on Power Delivery*, vol. 14, no. 3, pp. 1052–1061, Jul. 1999.
- [25] S. C. Cripps, *RF Power Amplifiers for Wireless Communications*, 2nd ed. Norwood, MA: Artech House, 2006.
- [26] G. Noetscher, A. T. Htet, and S. Makarov, "N-Library of basic triangular surface human body meshes from male subjects," 2014. [Online]. Available: <https://www.nevaelectromagnetics.com/>
- [27] S. Gabriel, R. W. Lau, and C. Gabriel, "The dielectric properties of biological tissues: II. Measurements in the frequency range 10 Hz to 20 GHz," *Physics in Medicine and Biology*, vol. 41, no. 11, pp. 2251–2269, nov 1996.
- [28] J. G. Webster, *Medical instrumentation : Application and Design*, 4th ed. Hoken, NJ: John Wiley & Sons, Inc., 2010.

- [29] H. Yoo and C. V. Hoof, *Bio-medical CMOS ICs*, 1st ed. New York, NY: Springer, 2011.
- [30] J. Park and P. P. Mercier, “Magnetic Human Body Communication,” in *2015 37th Annual International Conference of the IEEE Engineering in Medicine and Biology Society (EMBC)*. IEEE, Aug. 2015, pp. 1841–1844.
- [31] D. Son, J. Lee, S. Qiao, R. Ghaffari, J. Kim, J. E. Lee, C. Song, S. J. Kim, D. J. Lee, S. W. Jun, S. Yang, M. Park, J. Shin, K. Do, M. Lee, K. Kang, C. S. Hwang, N. Lu, T. Hyeon, and D.-H. Kim, “Multifunctional wearable devices for diagnosis and therapy of movement disorders,” *Nature Nanotechnology*, vol. 9, no. 5, pp. 397–404, may 2014.
- [32] D. H. Kim, N. Lu, R. Ma, Y. S. Kim, R. H. Kim, S. Wang, J. Wu, S. M. Won, H. Tao, A. Islam, K. J. Yu, T. I. Kim, R. Chowdhury, M. Ying, L. Xu, M. Li, H. J. Chung, H. Keum, M. McCormick, P. Liu, Y. W. Zhang, F. G. Omenetto, Y. Huang, T. Coleman, and J. A. Rogers, “Epidermal electronics,” *Science*, vol. 333, no. 6044, pp. 838–843, aug 2011.
- [33] K. I. Jang, K. Li, H. U. Chung, S. Xu, H. N. Jung, Y. Yang, J. W. Kwak, H. H. Jung, J. Song, C. Yang, A. Wang, Z. Liu, J. Y. Lee, B. H. Kim, J. H. Kim, J. Lee, Y. Yu, B. J. Kim, H. Jang, K. J. Yu, J. Kim, J. W. Lee, J. W. Jeong, Y. M. Song, Y. Huang, Y. Zhang, and J. A. Rogers, “Self-assembled three dimensional network designs for soft electronics,” *Nature Communications*, vol. 8, p. 15894, jun 2017.
- [34] J. Wang, “Electrochemical glucose biosensors,” *Electrochemical Sensors, Biosensors and their Biomedical Applications*, vol. 108, no. 2, pp. 57–69, feb 2008.
- [35] S. Emaminejad, W. Gao, E. Wu, Z. A. Davies, H. Yin Yin Nyein, S. Challa, S. P. Ryan, H. M. Fahad, K. Chen, Z. Shahpar, S. Talebi, C. Milla, A. Javey, and R. W. Davis, “Autonomous sweat extraction and analysis applied to cystic fibrosis and glucose monitoring using a fully integrated wearable platform,” *Proceedings of the National Academy of Sciences*, vol. 114, no. 18, pp. 4625–4630, may 2017.
- [36] S. Imani, A. J. Bandodkar, A. M. Mohan, R. Kumar, S. Yu, J. Wang, and P. P. Mercier, “A wearable chemical-electrophysiological hybrid biosensing system for real-time health and fitness monitoring,” *Nature Communications*, vol. 7, p. 11650, may 2016.
- [37] W. Gao, S. Emaminejad, H. Y. Y. Nyein, S. Challa, K. Chen, A. Peck, H. M. Fahad, H. Ota, H. Shiraki, D. Kiriya, D.-H. Lien, G. A. Brooks, R. W. Davis, and A. Javey, “Fully integrated wearable sensor arrays for multiplexed in situ perspiration analysis,” *Nature*, vol. 529, no. 7587, pp. 509–514, jan 2016.
- [38] P. P. Mercier and A. P. Chandrakasan, *Ultra-Low-Power Short-Range Radios*. New York, NY: Springer, 2015.

- [39] Texas Instruments, “2.4-GHz Bluetooth <sup>®</sup> low energy System-on-Chip,” Tech. Rep. October 2010, 2013.
- [40] Intan Technologies, “RHD2000 Series Digital Electrophysiology Interface Chips,” Tech. Rep., 2012.
- [41] A. Kurs, A. Karalis, M. Robert, J. D. Joannopoulos, P. Fisher, and M. Soljacic, “Wireless power transfer via strongly coupled magnetic resonances,” *Science*, vol. 317, no. 5834, pp. 83–86, 2007.
- [42] J. Park, H. Garudadri, and P. P. Mercier, “Channel Modeling of Miniaturized Battery-Powered Capacitive Human Body Communication Systems,” *IEEE Transactions on Biomedical Engineering*, vol. 64, no. 2, pp. 452–462, Feb 2017.
- [43] J. Park and P. P. Mercier, “A Sub-40 $\mu$ W 5Mb/s Magnetic Human Body Communication Transceiver Demonstrating Trans-Body Delivery of High-Fidelity Audio to a Wearable In-Ear Headphone,” in *2019 IEEE International Solid-State Circuits Conference (ISSCC)*, Feb 2019, pp. 286–287.
- [44] J. Park and P. P. Mercier, “A Sub-10-pJ/bit 5-Mb/s Magnetic Human Body Communication Transceiver,” *IEEE Journal of Solid-State Circuits*, pp. 1–12, 2019.
- [45] C. A. Balanis, *Advanced Engineering Electromagnetics*. Wiley, 2012.
- [46] S. Kim, J. S. Ho, and A. S. Y. Poon, “Midfield wireless powering of subwavelength autonomous devices,” *Physical Review Letters*, vol. 110, no. 20, p. 203905, may 2013.
- [47] J. S. Ho, A. J. Yeh, E. Neofytou, S. Kim, Y. Tanabe, B. Patlolla, R. E. Beygui, and A. S. Y. Poon, “Wireless power transfer to deep-tissue microimplants,” *Proceedings of the National Academy of Sciences of the United States of America*, vol. 111, no. 22, jun 2014.
- [48] J. Volakis, C.-C. Chen, and K. Fujimoto, *Small Antennas: Miniaturization Techniques & Applications*. McGraw-Hill Professional Publishing, 2009.
- [49] A. S. Y. Poon, S. O’Driscoll, and T. H. Meng, “Optimal frequency for wireless power transmission into dispersive tissue,” *IEEE Transactions on Antennas and Propagation*, vol. 58, no. 5, pp. 1739–1750, May 2010.
- [50] J. R. Wait, “The magnetic dipole antenna immersed in a conducting medium,” *Proceedings of the IRE*, vol. 40, no. 10, pp. 1244–1245, Oct 1952.
- [51] G. S. Smith, “A theoretical and experimental study of the insulated loop antenna in a dissipative medium,” *Radio Science*, vol. 8, no. 7, pp. 711–725, July 1973.

- [52] E. Snitzer, "Cylindrical dielectric waveguide modes," *Journal of the Optical Society of America*, vol. 51, no. 5, p. 491, may 1961.
- [53] C. Yeh and F. I. Shimabukuro, *The Essence of Dielectric Waveguides*. Springer, 2008.
- [54] A. W. Snyder, "Leaky-ray theory of optical waveguides of circular cross section," *Applied Physics*, vol. 4, no. 4, pp. 273–298, sep 1974.
- [55] J. Park, C. Kim, A. Akinin, S. Ha, G. Cauwenberghs, and P. P. Mercier, "Wireless powering of mm-scale fully-on-chip neural interfaces," *2017 IEEE Biomedical Circuits and Systems Conference (BioCAS)*, pp. 1–4, oct 2017.
- [56] C. Wang, E. Li, and D. F. Sievenpiper, "Surface-wave coupling and antenna properties in two dimensions," *IEEE Transactions on Antennas and Propagation*, vol. 65, no. 10, pp. 5052–5060, Oct 2017.
- [57] Federal Communications Commission, "Guidelines for Evaluating the Environmental Effects of Radiofrequency Radiation," Federal Communications Commission, Tech. Rep., 1993.
- [58] P. S. Hall and Y. Hao, *Antennas and Propagation for Body-Centric Wireless Communications*. Artech, 2012.
- [59] IEEE 802 working group, "IEEE Standard for Local and metropolitan area networks - Part 15.6: Wireless Body Area Networks," Tech. Rep., 2012.
- [60] J. Edelmann and T. Ussmueller, "Can You Hear Me Now?: Challenges and Benefits for Connectivity of Hearing Aids and Implants," *IEEE Microwave Magazine*, vol. 19, no. 7, pp. 30–42, Nov 2018.
- [61] T. G. Zimmerman, "Personal area networks (pan): Near-field intra-body communication," Master's thesis, Massachusetts Inst. Technol., Cambridge, MA, 1995.
- [62] N. Cho, L. Yan, J. Bae, and H. Yoo, "A 60 kb/s 10 Mb/s Adaptive Frequency Hopping Transceiver for Interference-Resilient Body Channel Communication," *IEEE Journal of Solid-State Circuits*, vol. 44, no. 3, pp. 708–717, March 2009.
- [63] A. Fazzi, S. Ouzounov, and J. van den Homberg, "A 2.75mW Wideband Correlation-Based Transceiver for Body-Coupled Communication," in *2009 IEEE International Solid-State Circuits Conference (ISSCC)*, Feb 2009, pp. 204–205.
- [64] J. Bae, K. Song, H. Lee, H. Cho, and H. Yoo, "A 0.24-nJ/b Wireless Body-Area-Network Transceiver With Scalable Double-FSK Modulation," *IEEE Journal of Solid-State Circuits*, vol. 47, no. 1, pp. 310–322, Jan 2012.

- [65] J. Lee, V. V. Kulkarni, C. K. Ho, J. H. Cheong, P. Li, J. Zhou, W. Da Toh, X. Zhang, Y. Gao, K. W. Cheng, X. Liu, and M. Je, "A 60Mb/s Wideband BCC Transceiver with 150 pJ/b RX and 31 pJ/b TX for Emerging Wearable Applications," in *2014 IEEE International Solid-State Circuits Conference (ISSCC)*, Feb 2014, pp. 498–499.
- [66] H. Cho, H. Lee, J. Bae, and H. Yoo, "A 5.2 mW IEEE 802.15.6 HBC Standard Compatible Transceiver With Power Efficient Delay-Locked-Loop Based BPSK Demodulator," *IEEE Journal of Solid-State Circuits*, vol. 50, no. 11, pp. 2549–2559, Nov 2015.
- [67] H. Cho, H. Kim, M. Kim, J. Jang, Y. Lee, K. J. Lee, J. Bae, and H. Yoo, "A 79 pJ/b 80 Mb/s Full-Duplex Transceiver and a 42.5  $\mu$ W 100 kb/s Super-Regenerative Transceiver for Body Channel Communication," *IEEE Journal of Solid-State Circuits*, vol. 51, no. 1, pp. 310–317, Jan 2016.
- [68] J. Lee, K. Kim, M. Choi, J. Sim, H. Park, and B. Kim, "A 16.6-pJ/b 150-Mb/s Body Channel Communication Transceiver with Decision Feedback Equalization Improving >200% Area Efficiency," in *2017 Symposium on VLSI Circuits*, June 2017, pp. C62–C63.
- [69] W. Saadeh, M. A. B. Altaf, H. Alsuradi, and J. Yoo, "A 1.1-mW Ground Effect-Resilient Body-Coupled Communication Transceiver With Pseudo OFDM for Head and Body Area Network," *IEEE Journal of Solid-State Circuits*, vol. 52, no. 10, pp. 2690–2702, Oct 2017.
- [70] S. Maity, B. Chatterjee, G. Chang, and S. Sen, "A 6.3pJ/b 30Mbps - 30dB SIR-Tolerant Broadband Interference-Robust Human Body Communication Transceiver Using Time Domain Signal-Interference Separation," in *2018 IEEE Custom Integrated Circuits Conference (CICC)*, April 2018, pp. 1–4.
- [71] J. Zhao, J. Mao, T. Zhou, L. Lai, H. Yang, and B. Zhao, "An Auto Loss Compensation System for Non-contact Capacitive Coupled Body Channel Communication," in *2018 IEEE International Symposium on Circuits and Systems (ISCAS)*, May 2018, pp. 1–5.
- [72] S. Maity, M. He, M. Nath, D. Das, B. Chatterjee, and S. Sen, "BioPhysical Modeling, Characterization and Optimization of Electro-Quasistatic Human Body Communication," *IEEE Transactions on Biomedical Engineering*, pp. 1–1, 2018.
- [73] D. Lee, L. G. Salem, and P. P. Mercier, "Narrowband Transmitters: Ultra low-Power Design," *IEEE Microwave Magazine*, vol. 16, no. 3, pp. 130–142, April 2015.
- [74] J. L. Bohorquez, A. P. Chandrakasan, and J. L. Dawson, "A 350  $\mu$  W CMOS MSK Transmitter and 400  $\mu$ W OOK Super-Regenerative Receiver for Medical Implant

- Communications,” *IEEE Journal of Solid-State Circuits*, vol. 44, no. 4, pp. 1248–1259, April 2009.
- [75] P. P. Mercier, S. Bandyopadhyay, A. C. Lysaght, K. M. Stankovic, and A. P. Chandrakasan, “A Sub-nW 2.4 GHz Transmitter for Low Data-Rate Sensing Applications,” *IEEE Journal of Solid-State Circuits*, vol. 49, no. 7, pp. 1463–1474, July 2014.
- [76] V. Kratyuk, P. K. Hanumolu, K. Mayaram, and U. Moon, “A 0.6GHz to 2GHz Digital PLL with Wide Tracking Range,” in *2007 IEEE Custom Integrated Circuits Conference*, Sep. 2007, pp. 305–308.
- [77] N. E. Roberts, K. Craig, A. Shrivastava, S. N. Wooters, Y. Shakhsher, B. H. Calhoun, and D. D. Wentzloff, “A 236nW -56.5dBm Sensitivity Bluetooth Low-Energy Wakeup Receiver with Energy Harvesting in 65nm CMOS,” in *2016 IEEE International Solid-State Circuits Conference (ISSCC)*, Jan 2016, pp. 450–451.
- [78] P. P. Wang, H. Jiang, L. Gao, P. Sen, Y. Kim, G. M. Rebeiz, P. P. Mercier, and D. A. Hall, “A Near-Zero-Power Wake-Up Receiver Achieving -69-dBm Sensitivity,” *IEEE Journal of Solid-State Circuits*, vol. 53, no. 6, pp. 1640–1652, June 2018.
- [79] A. S. Rekhi and A. Arbabian, “A 14.5mm<sup>2</sup> 8nW -59.7dBm Sensitivity Ultrasonic Wake-Up Receiver for Power-, Area-, and Interference-Constrained Applications,” in *2018 IEEE International Solid-State Circuits Conference (ISSCC)*, Feb 2018, pp. 454–456.
- [80] P. P. Wang and P. P. Mercier, “A 220 $\mu$ W -85dBm Sensitivity BLE-Compliant Wake-Up Receiver Achieving -60dB SIR via Single-Die Multi-Channel FBAR-Based Filtering and a 4-Dimensional Wake-Up Signature,” in *2019 IEEE International Solid-State Circuits Conference (ISSCC)*, Feb 2019, pp. 440–442.
- [81] S. Ha, A. Akinin, J. Park, C. Kim, H. Wang, C. Maier, P. P. Mercier, and G. Cauwenberghs, “Silicon-Integrated High-Density Electrocranial Interfaces,” *Proceedings of the IEEE*, vol. 105, no. 1, pp. 11–33, Jan. 2017.
- [82] M. Zargham and P. G. Gulak, “Fully Integrated On-Chip Coil in 0.13  $\mu$ m CMOS for Wireless Power Transfer Through Biological Media,” *IEEE Transactions on Biomedical Circuits and Systems*, vol. 9, no. 2, pp. 259–271, April 2015.
- [83] S. S. Mohan, M. del Mar Hershenson, S. P. Boyd, and T. H. Lee, “Simple Accurate Expressions for Planar Spiral Inductances,” *IEEE Journal of Solid-State Circuits*, vol. 34, no. 10, pp. 1419–1424, Oct 1999.
- [84] A. M. Niknejad and R. G. Meyer, “Analysis, Design, and Optimization of Spiral Inductors and Transformers for Si RF ICs,” *IEEE Journal of Solid-State Circuits*, vol. 33, no. 10, pp. 1470–1481, Oct 1998.

- [85] C. P. Yue and S. S. Wong, "On-chip Spiral Inductors with Patterned Ground Shields for Si-based RF ICs," *IEEE Journal of Solid-State Circuits*, vol. 33, no. 5, pp. 743–752, May 1998.
- [86] P. P. Mercier and A. P. Chandrakasan, "Rapid Wireless Capacitor Charging Using a Multi-Tapped Inductively-Coupled Secondary Coil," *IEEE Transactions on Circuits and Systems I: Regular Papers*, vol. 60, no. 9, pp. 2263–2272, Sept. 2013.
- [87] U. M. Jow and M. Ghovanloo, "Design and Optimization of Printed Spiral Coils for Efficient Transcutaneous Inductive Power Transmission," *IEEE Transactions on Biomedical Circuits and Systems*, vol. 1, no. 3, pp. 193–202, Sept 2007.
- [88] Y. Cheng, G. Wang, and M. Ghovanloo, "Analytical Modeling and Optimization of Small Solenoid Coils for Millimeter-Sized Biomedical Implants," *IEEE Transactions on Microwave Theory and Techniques*, vol. 65, no. 3, pp. 1024–1035, March 2017.
- [89] D. Ahn and M. Ghovanloo, "Optimal Design of Wireless Power Transmission Links for Millimeter-Sized Biomedical Implants," *IEEE Transactions on Biomedical Circuits and Systems*, vol. 10, no. 1, pp. 125–137, Feb. 2016.
- [90] A. Ibrahim and M. Kiani, "A Figure-of-Merit for Design and Optimization of Inductive Power Transmission Links for Millimeter-Sized Biomedical Implants," *IEEE Transactions on Biomedical Circuits and Systems*, vol. 10, no. 6, pp. 1100–1111, Dec. 2016.
- [91] P. T. Theilmann and P. M. Asbeck, "An Analytical Model for Inductively Coupled Implantable Biomedical Devices With Ferrite Rods," *IEEE Transactions on Biomedical Circuits and Systems*, vol. 3, no. 1, pp. 43–52, Feb 2009.
- [92] C. Kim, S. Ha, J. Park, A. Akinin, P. Mercier, and G. Cauwenberghs, "A 144 MHz Fully Integrated Resonant Regulating Rectifier with Hybrid Pulse Modulation for mm-sized Implants," *IEEE Journal of Solid-State Circuits*, 2017.
- [93] C. Kim, J. Park, A. Akinin, S. Ha, R. Kubendran, H. Wang, P. Mercier, and G. Cauwenberghs, "A Fully Integrated 144 MHz Wireless-Power-Receiver-on-Chip with an Adaptive Buck-Boost Regulating Rectifier and Low-Loss H-Tree Signal Distribution," in *Symposium on VLSI Circuits (VLSI Circuits)*, Jun. 2016.
- [94] S. Ha, C. Kim, J. Park, G. Cauwenberghs, and P. P. Mercier, "A Fully Integrated RF-Powered Energy-Replenishing Current-Controlled Stimulator," *IEEE Transactions on Biomedical Circuits and Systems*, vol. 13, no. 1, pp. 191–202, Feb 2019.